Static Structural Analysis of OceanGate's Titan Submersible: Analytical and Numerical Comparison with Ansys

a report presented to
The Faculty of the Department of Aerospace Engineering
San José State University

in partial fulfillment of the requirements for the degree
Master of Science in Aerospace Engineering

by

Ignacio D. Ramírez Romero

May 2025

approved by

Dr. Maria Chierichetti
Faculty Advisor

ABSTRACT

Static Structural Analysis of OceanGate's Titan Submersible: Analytical and Numerical Comparison with Ansys

Ignacio D. Ramírez Romero

The following work analyzes the static structural response of a deep-sea ocean submersible. More specifically, a simplified geometry model of OceanGate's Titan Submersible was developed using available online resources and later analyzed using Ansys's Static Structural. The geometry model is represented by a carbon fiber reinforced epoxy (CFRE) cylindrical section flanked by two titanium hemispheres, with a polymethyl methacrylate (PMMA) observation window embedded in the bow. The cylindrical section and the hemispheres are connected through two titanium O-ring interfaces assumed to be perfectly bonded. Total nodal displacements and structural failure were investigated developing a Finite Element model in Ansys Static Structural. Total displacements predicted by Ansys for the CFRE cylindrical section were then compared to those predicted by an analytical model. A brief literature review of failure of composite materials and an overview of the Finite Element Method (FEM) is discussed. Results suggest that failure occurs at the edges and middle of the cylindrical section with the current thickness and laminate selection. A low safety factor was observed in the O-Ring section connected to the pressure hull. Additional study cases and potential improvements are shared in the last section of this report.

Acknowledgements

Although the journey of professional learning is never-ending, I would like to express my gratitude to the entire SJSU Aerospace Engineering Department. Without the dedication and tireless efforts of our professors to teach and equip us with the tools to succeed both academically and professionally, the completion of this journey would not have been possible. In particular, I would like to thank Dr. Chierichetti for her infinite patience, encouragement, and support in the completion of this project. Challenges that have cost me hours of work have been solved in minutes by her expertise, skillfulness, and insight. Not only did Dr. Chierichetti approve of pursuing the project in which I was actively interested, but she also helped me prepare for the job interview that enabled me to secure a position as a mechanical engineer after the completion of my bachelor's degree. My current project investigator, Rufus Yazzie, and program manager, Stephen Shock, have also provided with encouragement, a wealth of technical resources, and an infinite number of jokes about California, for which I am proud and thankful.

Lastly, I thank my family and friends, who have both encouraged me and endured my absence from family and social events to support the pursuit of my career goals. Specially, I express my eternal gratitude toward my grandmother and grandaunt, Carolina Téllez Pérez and María Matilde Téllez Pérez. These two stellar ladies have shared their time, energy, and resources ensuring I had a loving home and the support to challenge myself daily and care for my friends, community and country. They have and continue to do so since I gained consciousness until now, at her 86 and 77 years of life.

Table Of Contents

List of Figures

List of Tables

Symbols, Subscripts, Superscripts and Acronyms

Symbol	Definition	Units (SI)
σ	Stress	Pa
D	Delamination damage variable	-
N	Cycle number of fatigue loading	-
Y	Range of damage evolution variable	-
A	Material parameter	-
β	Material parameter	-
Y_{12}	Thermodynamic force relating to damage variables	Pa
Y_{12}	Thermodynamic force relating to damage variables	Pa
k	Coupling parameter	-
D_E	Residual Stiffness Damage	
D_S	Residual Strength	
w	Exponential fitting parameter	-
X	Strength value for σ_1	Pa^2
Y	Strength value for σ_2	Pa^2
S	Strength value for σ_{12}	Pa
S_0	Failure strength of composite laminate	Pa
F_i	Experimental material constant	Pa^{-1}
F_{ij}	Experimental material constant	Pa^{-2}
τ	Shear Stress	Pa
E	Modulus of elasticity	Pa
G	Shear's modulus	Pa
γ	Poisson's ratio	-
$[.]^+$	Heavyside function	-
ϵ	Strain	-
d	Micro-level damage property	-
d	Displacement	m
ΔT	Environment and manufacturing temperature difference	Kq
α	Coefficient of thermal expansion	-
N_{ini}	Matrix crack initiation life	-
K_0	Material Parameter	-
λ	Material Parameter	-
g	Gravitational acceleration on earth	m/s^2
f	Applied force	N
F	Applied force	N
Q	Stiffness matrix	-
ρ	Density	-
q	Ratio of extension length to total length	-
U	Normalized displacement matrix of the matrix	

∇	Laplace Operator	-
ϵ	Strain	-
T	Temperature	K
C	Speed of Sounds	m/s
A	Material parameter measured at transition temperature	Pa
B	Material parameter measured at transition temperature	-
C	Material parameter measured at transition temperature	-
m	Material parameter measured at transition temperature	-
n	Material parameter measured at transition temperature	-
γ_s	Grüneisen coefficient	-
S	Material parameter	-
D_1	Material parameter	-
D_2	Material parameter	-
D_3	Material parameter	-
D_4	Material parameter	-
μ	Modeling parameter	-
Δ	Difference between final and initial properties	-
A	Material parameter	K
m	Material parameter	-
a_1	Material parameter	K^{-3}
b_1	Material parameter	K^{-2}
c_1	Material parameter	K^{-1}
k_1	Material parameter	K/Pa
d_1	Material parameter	K
n	Material parameter	-
a_2	Material parameter	K^{-2}
b_2	Material parameter	K^{-1}
c_2	Material parameter	K/Pa
k_2	Material parameter	K
t	Time	s
C	Integral constant based on elastic strain before loading	-
A	Area	m^2
u	Displacement	m
k	Local stiffness matrix	N/m
K	Global stiffness matrix	N/m
l_t	Bar length	m
P	Applied load	N
L	Length	m
c	Integration constant	-
Π_P	Potential Energy	J
Ω	External potential energy	J
U	Internal strain energy	J
[B]	Stress-displacement matrix	-

[N]	Matrix shape function	-
N	Membrane Forces	N
h	Shell Thickness	m
R	Radius of curvature	m
M	Moment	Nm
κ	Laminate curvature	m
Q	Reduced stiffness coefficients matrix	Pa
D	Engineering constant	-
A	Element of ABD matrix	N/m
B	Element of ABD matrix	N
D	Element of ABD matrix	Nm
T_σ	Rotation matrix	-
T_ϵ	Rotation matrix	-
V	Shear force	N
u	Axial displacement	m
v	Circumferential displacement	m
w	Radial displacement	m
T	Torque	Nm
P	Pressure	Pa
γ	Roots of characteristic equation	-
h	Depth location of geometry	m
Subscripts		
$()_1$	Fiber direction	
$()_2$	Direction transverse to fiber	
$()_{12}$	In-plane	
$()_1$	Longitudinal Direction	
$()_2$	Transverse Direction	
$()_3$ or $()_6$	Orthogonal Direction	
$()_f$	Fiber	
$()_m$	Matrix	
$()_m$	Melting	
$()_{room}$	Room	
$()_d$ or $()_r$	Damaged state	
$()_0$	Undamaged state	
$()_{s,t}$	Current	
$()_s$	Initial	
$()_i$	Of each element	

Superscripts		
$()^{+}$	Tension	
$()^{-}$	Compression	
$()^{0}$	Original State	
$(\dot{\ })$	Rate	
$[]^{T}$	Transpose Matrix	
Acronyms		
TS	Titan Submersible	
FEM	Finite Element Method	
FEA	Finite Element Analysis	

1. Introduction

1.1 Introduction

Humanity's unending quest for knowledge and exploration has catalyzed the advancement of science and subsequent development of various technologies. During this process, the lives of many individuals around the world have been positively impacted. That is the case, for example, with Global Positioning System (GPS), whose original purpose was the tracking of maritime vehicles and military targets [1]. Today, individuals around the world enjoy the accessibility of GPS for tasks spanning from driving to a desired destination or knowing with precision the location of certain objects. Moreover, the development of Sonar Navigation and Ranging -also referred to as sonar, - used to map objects in the ocean, pioneered the later creation of ultrasound [2]. The benefits of this technology enable medical professionals to monitor fetal development and assess potential anomalies in several internal organs [3]. Fruits of scientific and technological innovation have, undeniably, positively impacted the lives of individuals around the world.

Another oceanic invention with a noble purpose -but a catastrophic outcome- was that embodied by OceanGate's Titan submersible. As included in OceanGate's website (now archived), its main mission was to facilitate commercial expeditions and scientific research and exploration [4]. Most notably, within the scope of these commercial expeditions, was the transport of passengers to the wreckage site of the Titanic, located approximately 690 kms southeast of Newfoundland, Canada. On June 18, 2024, the US Navy's sonar detected an acoustic signature which was later confirmed to be the implosion of the Titan submersible [5]. Stockton Rush, the principal engineer who oversaw the design and construction of the Titan, neglected warnings provided by industry experts regarding the questionable reliability and safety of the Titan. Should these warnings have been considered seriously, the loss of five human lives, who participated in the last expedition of the Titan submersible during its implosion, including that of Stockton Rush himself, could have been prevented. This work seeks to provide a general insight into structural challenges generated by the operational design of the Titan submersible using Ansys Static Structural . Identifying, understanding, and improving deficiencies in the final design of human occupied vehicles (HOV) in deep-sea environments will provide future designers with an additional outlook about limitations and promising design configurations for the development of deep-sea vehicles.

1.2 Background

An image of the Titan Submersible and its schematic is depicted in Figure 1.1. The pressurized section of the submersible consisted of two main elements: a carbon-fiber cylindrical section flanked by two titanium spheres with one acrylic window [6]. Possibly, for legal reasons after the implosion of the submersible, OceanGate deleted all the content previously available on its website. Despite the lack of current peer-reviewed literature detailing its specific dimensions, available online resources appeared to reach consensus regarding its principal measurements. Four of these sources, [7], [8], [9], [10], reflect the specifications summarized in Table 1.1.

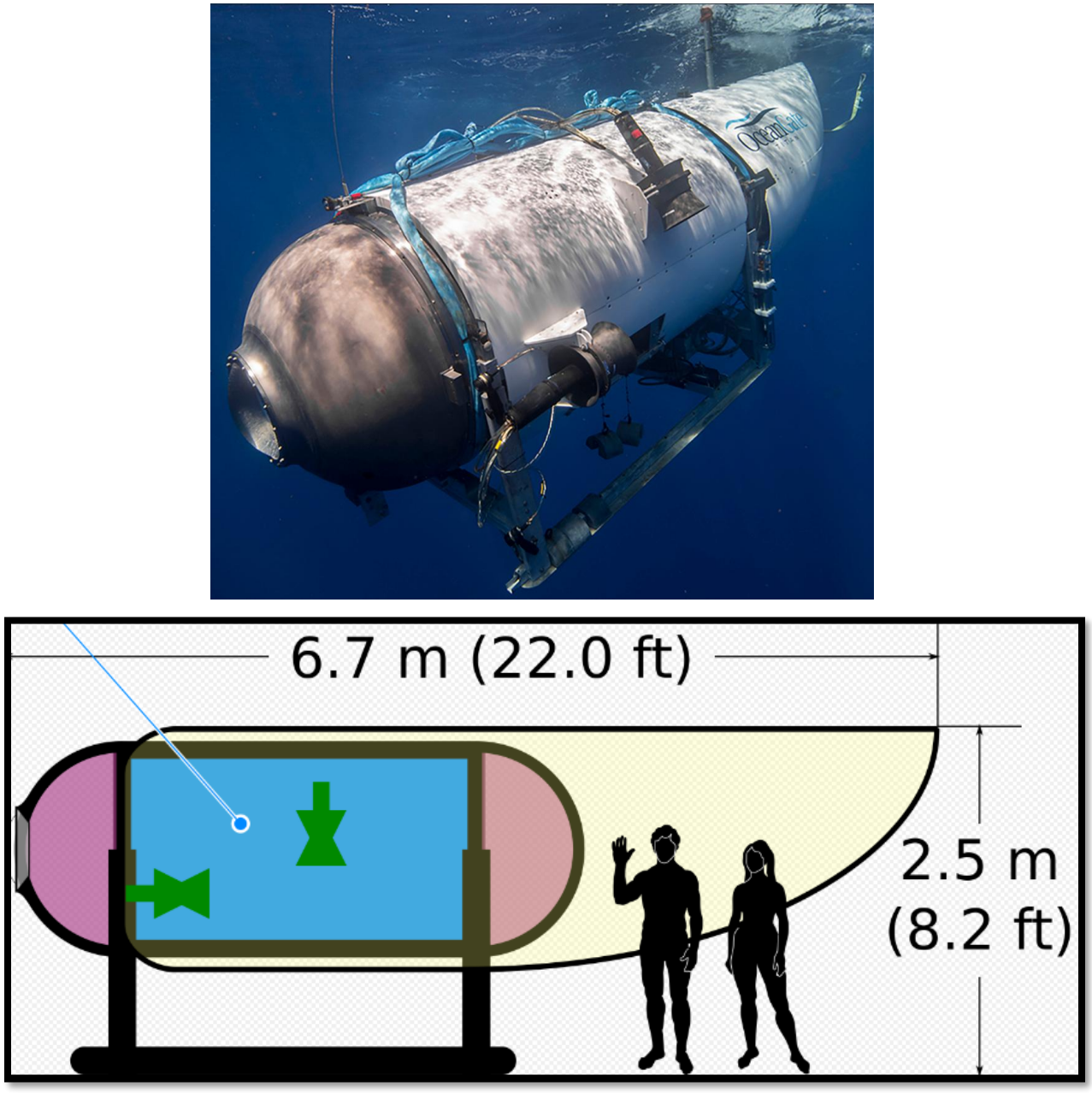

Figure 1.1 - Titan Submersible underwater and its schematic [6].

Table 1.1 - Dimensions of the Titan submersible according to online resources.

Dimensions		Wikipedia [7]	Seattle Times [8]	The Guardian [9]	People [10]
Overall Dimensions	Length [ft]	22	22	22	22
	Height [ft]	8.2	8.3	8.2	8.3
	Width [ft]	9.2	-	9.19	9.2
Carbon-Fiber Wound Cylinder	Diameter [ft]	5.5*	4.6	-	-
	Length [ft]	8.3	8.3	-	-
	Thickness [in]	5.0	-	-	-
Titanium Caps	Thickness [in]	3.25	-	-	-

*Judged as the "outer diameter"

The nature of the Titan Submersible's mission, which required reaching a depth of approximately 4km, subjected the structure to extremely harsh operating conditions. The hydrostatic pressure increases by 1 atmosphere for every 10.06 meters of descent [11]. For this corresponding diving depth, the submersible experienced an omnidirectional pressure of 398 atmospheres, or 40.33 MPa, attempting its implosion. Of the three main materials previously identified, carbon fiber composite possesses failure modes whose theoretical models have not undergone extensive experimental testing. Precisely, this cyclical increase in pressure at such low diving depths might have switched the cause of structural failure from overall buckling to gradual material failure in the composite pressure hull [12]. The various material interfaces, in addition to the cyclical pressure loading experienced by this maritime system add complexity to the modeling techniques of composite pressure hulls, relative to the better understood behavior of isotropic materials, such as metal alloys. To mitigate the enormous hydrostatic pressure to which the vessel was exposed, the thickness of the structure had to be significantly increased. Nevertheless, pressure hulls of large thicknesses are more prone to phenomenon called snap buckling, a sudden, catastrophic material failure [12]. It is crucial to consider various potential failure mechanisms appropriate to each material to assess the potential mechanical behavior of an underwater composite pressure vessel.

1.3 Previous Studies on Structural Failure Modeling

Understanding the various possible failure mechanisms of a fiber-reinforced composite structure, like the cylindrical body of the Titan Submersible, requires first exploring the most fundamental *unit* of this type of composite material: a laminate. In a fiber reinforced composite material, a lamina consists of two constituents: fibers and a bonding material interface called matrix. When a group of laminae are stacked in multiple directions to achieve superior mechanical properties, the resulting unit structure is called a *laminate.* Several methodologies have been developed to predict the structural failure mechanisms for complex materials of this nature. The author proposes discussing these theories as classical and modern. After reviewing these two

failure theories for laminates, failure theories targeting composite pressure hulls specifically will be explored. Finally, structural failure modeling of the other dominant materials, titanium alloy and acrylic, will be briefly explored.

1.3.1 Classical Failure Criteria of Composite Materials

One such categorization classified failure as occurring at either single-scale or multi-scale. In the single-scale arena, the first major effort consisted of modeling a composite structure as homogenized and unidirectional. In 1948, Hill [13] proposed describing the yield criterion for isotropic metals as orthotropic by using six independent yield stresses. Using a cartesian coordinate system, these could be described as three normal stresses in each symmetrical direction and three shear stresses on each symmetrical plane. In 1965, Azzi and Tsai [14] proposed a mathematical model derived by equating the six yield stresses in the Hill criterion to a series of corresponding strength values of a unidirectional composite. This model became known as the Tsai-Hill criteria, and its mathematical expression is summarized in equation 1.1. Here, the normal stress in the fiber and transverse directions are represented by σ_1 and σ_2. The in-plane shear stress is denoted by σ_{12}, and X, Y, and S are the strength values of σ_1, σ_2, and σ_{12}. Its main source of criticism became its incorrect modeling based on *yielding*, which does not correctly capture the failure mechanism of unidirectional composites.

$$\left(\frac{\sigma_1}{X}\right)^2 - \left(\frac{\sigma_1\sigma_2}{X}\right) + \left(\frac{\sigma_2}{Y}\right)^2 + \left(\frac{\sigma_{12}}{S}\right) = 1 \qquad (1.1)$$

Experimental inconsistencies between values predicted by the Tsai-Hill criteria led to a proposed improvement by Tsai and Wu [15]. Distinctive to Tsai-Hill, the Tsai-Wu criteria was based on a scalar function expressed as a polynomial in terms of the stress tensor components, as denoted by equation 1.2. For a unidirectional laminate, indices i and j obtain the values of 1, 2, and 6, and the repeated indices signal summation. The coefficients F_i and F_{ij} are referred to as material strength constants, which are obtained experimentally. The Tsai-Wu criteria allowed for the creation of an ellipsoidal fit representation of the failure limits. Like the Tsai-Hill criteria, the main critique attributed to Tsai-Wu was its inadequacy describing the failure mechanics of a lamina and representing instead a convenient mathematical framework.

$$F_i\sigma_j + F_{ij}\sigma_i\sigma_j = 1 \qquad (1.2)$$

Subsequent improvements to the Tsai-Hill took the form of Hashin and later Puck failure criteria. In his research, Hashin [16] signaled differences between experimental data and some stress components in equation 1.2. As a result, he then proposed increasing the number of failure modes for a composite material, such as failure for i) fibers in tension, ii) fibers in compression, iii) matrix in tension, and iv) matrix in compression. These failure modes are outlined as depicted in equations 1.3 through 1.6. Equations 1.3 and 1.4 represent the failure criteria for fibers in tension and compression, while 1.5 and 1.6 correspond to the failure criteria for the matrix in tension and compression. Subscripts 1, 2, and 3 refer to the longitudinal, transverse, and orthogonal (through-thickness) directions, whereas superscripts + and – denote tension or compression. The variable S denotes the values at which the corresponding failure types occur. In a subsequent investigation, Puck and colleagues [17] incorporated the concept of a failure plane which would not intersect the fibers of a unidirectional composite and had previously been suggested by Hashin, as well as

hybrid modes, which would consider failure during combined loading modes, such as tension and compression. Although the discussed theories enhanced the understanding and prediction of failure in a unidirectional laminate composite, Talreja [18] asserted that these classical theories were limited by the inability to describe the initiation of the first event that would cause the evolution of subsequent failure in the composite structure. All these initial efforts catalyzed the subsequent improvements in models of failure in composite materials.

$$\left(\frac{\sigma_{11}}{S_{11}^{+}}\right)^2 + \alpha\left(\frac{\sigma_{12}^2+\sigma_{13}^2}{S_{12}^2}\right) \geq 1.0 \tag{1.3}$$

$$\left(\frac{\sigma_{11}}{S_{11}^{-}}\right)^2 \geq 1.0 \tag{1.4}$$

$$\left(\frac{\sigma_{22}+\sigma_{33}}{S_{22}^{+}}\right)^2 + \frac{\sigma_{23}^2-\sigma_{22}\sigma_{33}}{S_{23}^2} + \frac{\sigma_{12}^2+\sigma_{13}^2}{S_{12}^2} \geq 1.0 \tag{1.5}$$

$$\left[\left(\frac{S_{22}^{-}}{2S_{23}}\right)^2 - 1\right]\left(\frac{\sigma_{22}+\sigma_{33}}{S_{22}^{-}}\right) + \frac{\left(\sigma_{23}-\sigma_{33}\right)^2}{4S_{23}^2} + \frac{\sigma_{23}^2-\sigma_{22}\sigma_{33}}{S_{23}^2} + \frac{\sigma_{12}^2+\sigma_{13}^2}{S_{12}^2} \geq 1.0 \tag{1.6}$$

1.3.2 Modern Failure Fracture Mechanics of Composite Laminates

One of the more recent efforts to characterize and predict structural failure of composite laminates was proposed by Qi and collaborators [19], whose work is summarized in the entirety of this subsection. First, the dominant damage modes in composite laminates were identified as matrix cracking, local delamination, and fiber breakage. This is illustrated in Figure 1.2, located below. Under repeated cyclic loadings, they observed that matrix cracks would first originate in *weaker* piles, which would typically form parallel to the direction of the fibers. As the number of loading cycles increased, these cracks would then saturate, leading to the degradation of the transverse modulus and shear modulus. Consequently, local delamination would start and develop at the edges of the transverse matrix cracks because of the stress concentration effects. As the matrix interface accumulated more damage, the fibers would then start to progressively bear more loading until fiber breakage -leading to catastrophic structural failure- would occur. Qi and colleagues provided a useful visualization of this process, as depicted in figure 1.3.

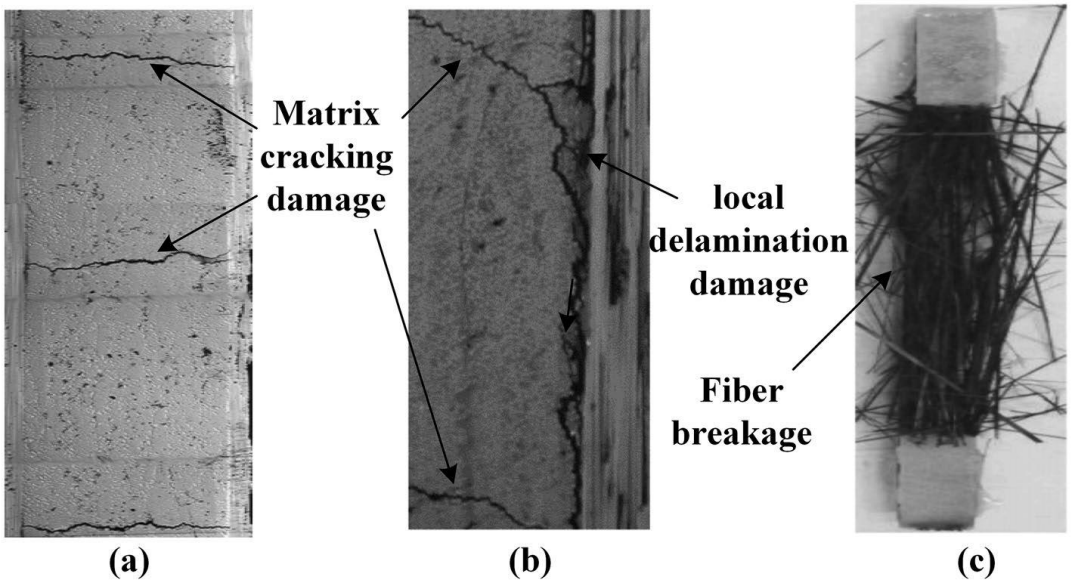

Figure 1.2 - Observed dominant damage modes in cross-ply composite laminates under fatigue loading [19].

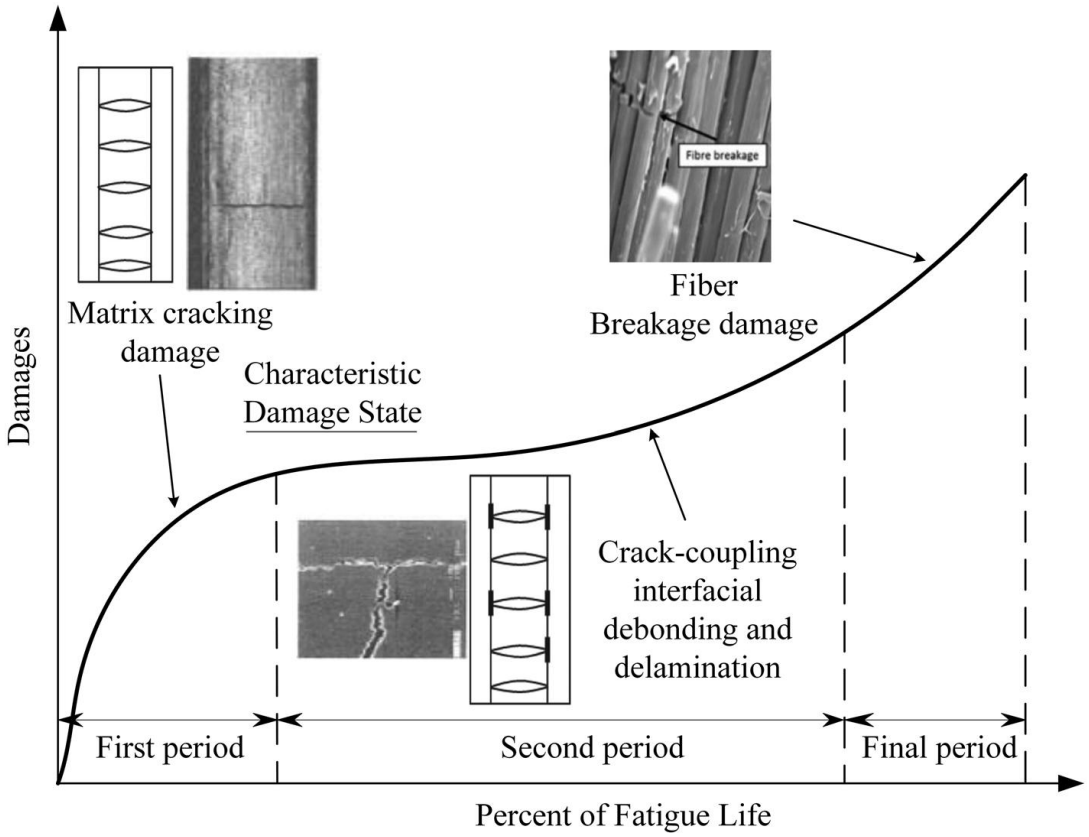

Figure 1.3 - Damage evolution in composites under fatigue loading [19].

To model the damage experienced by a composite structure, Qi introduced the concept of damaged strain energy density of an elementary ply, as summarized by equation 1.7. Subscripts 11, 22, and 12 denote the longitudinal, transverse, and orthogonal (through-thickness) directions. Superscripts f and m denote *fiber* and *matrix*, while 0 denotes the original properties (before-damage) of the ply. The main stresses, shear stress, Elasticity Modulus, shear modulus, Poisson's ratio, and the macro-level damage properties are denoted by $\sigma, \tau, \mathrm{E}, \mathrm{G}, \gamma$, and d, respectively. The blanket $[.]^{+}$ represents the Heavyside function. By applying the definition of strain energy release rate, in equation 1.8, the strain-stress relationship of a damaged ply could then be reflected in terms of the constitutive equations 1.9-a to 1.9-c. ϵ_{ij} represents the strain components. This set of three equations enabled the quantification of the damaged stiffness properties under fatigue loading. By including the effects of temperature changes, which induce thermal stress in composite laminates, as reflected by 1.10, the constitutive equations, 1.9-a through 1.9-c, could then be expressed as Equations 1.11-a through 1.11-c. Here, ϵ^{T} is the residual strain, ΔT denotes the difference between the loading environment and the manufacturing temperature, and α represents the thermal coefficient of expansion. Subscripts 1, 2, and 6 in α denote the longitudinal, transverse, and orthogonal (through-thickness) directions.

$$e_d = \frac{1}{2}\left(\frac{\sigma_{11}^2}{E_1^0(1-d^f)} + \frac{\sigma_{22}^2}{E_2^0(1-[\sigma_{22}]^{+}d_{22}^m)(1-d_{22}^l)} + \frac{\tau_{12}^2}{G_{12}^0(1-d_{12}^m)(1-d_{12}^l)} - \frac{2\nu_{12}^0\sigma_{11}\sigma_{22}}{E_1^0(1-d^f)}\right) \qquad (1.7)$$

$$\epsilon_{ij} = \frac{\partial e_d}{\partial \sigma_{ij}} \quad (1.8)$$

$$\epsilon_{11} = \frac{\sigma_{11}}{E_1^0(1-d^f)} - \frac{\nu_{12}^0}{E_1^0(1-d^f)}\sigma_{22} \quad (1.9\text{-a})$$

$$\epsilon_{22} = \frac{\sigma_{22}}{E_2^0(1-[\sigma_{22}]^+ d_{22}^m)(1-d_{22}^l)} - \frac{\nu_{12}^0}{E_1^0(1-d^f)}\sigma_{11} \quad (1.9\text{-b})$$

$$\gamma_{12} = \frac{\tau_{12}^2}{G_{12}^0(1-d_{12}^m)(1-d_{12}^l)} \quad (1.\ 9\text{-c})$$

$$\epsilon^T = \Delta T \alpha \quad (1.10)$$

$$\epsilon_{11} = \frac{\sigma_{11}}{E_1^0(1-d^f)} - \frac{\nu_{12}^0}{E_1^0(1-d^f)}\sigma_{22} + \alpha_1 \Delta T \quad (1.11\text{-a})$$

$$\epsilon_{22} = \frac{\sigma_{22}}{E_2^0(1-[\sigma_{22}]^+ d_{22}^m)(1-d_{22}^l)} - \frac{\nu_{12}^0}{E_1^0(1-d^f)}\sigma_{11} + \alpha_2 \Delta T \quad (1.11\text{-b})$$

$$\gamma_{12} = \frac{\tau_{12}^2}{G_{12}^0(1-d_{12}^m)(1-d_{12}^l)} + \alpha_6 \Delta T \quad (1.11\text{-c})$$

The main objective of modeling the damage evolution history of a composite laminate undergoing fatigue is the prediction of stiffness degradation. To achieve this objective, three damage evolution laws were outlined and integrated into the previous damage characterization model. These three laws were a) evolution law of matrix cracking, b) evolution law of delamination, and c) evolution law of fiber breakage. Principal highlights of this work appear summarized in the paragraphs below.

A. Evolution Law of Matrix Cracking

The first event in the proposed evolution damage model starts with the generation of transverse cracks in the matrix. The concept of initial matrix crack initiation life, summarized by Equation 1.16, was introduced to define whether transverse cracks would start or continue, evolve, and saturate. N_{ini} represents the matrix crack initiation life; σ_{max}^{90} denotes the maximum stress in cracked plies, and $\sigma_{ti}^{90}$is the initiation stress of an initial matrix crack in cracked plies, under the assumption of quasi-static loading. K_0 and λ are material parameters. Specifically, this theory outlined that when an applied maximum stress was smaller than the initial matrix crack initiation stress, matrix cracks would be expected to occur after several cycles. When the number of cycles reached the local initial matrix crack initiation life, cracks would be assumed to start. Moreover, when an applied maximum stress exceeded the initial matrix crack initiation stress, cracks would initiate during that stress cycle and eventually saturate. When this occurred, the damaged stiffness matrix of cracked cracks could then be calculated by the crack opening displacement theory, expressed by equation 1.17. Q_d represents the damaged stiffness matrix, ρ denotes the density of the transverse crack, I is the identity matrix, q represents the ratio of the extension length to the total length, and U is the normalized displacement matrix of the matrix crack surface. The undamaged longitudinal modulus and undamaged stiffness matrix are denoted by E_1^0 and Q_0, respectively. Consequently, the damaged elastic modulus of composite laminates could then be quantified according to the damaged longitudinal modulus, damaged transverse modulus, and damaged shear modulus, represented by equations 1.18-a to 1.18-c.

$$\log N_{ini} = \log K_0 - 2\lambda \log \sigma_{ti}^{90} + 2\lambda \log \sigma_{max}^{90} \quad (1.16)$$

$$Q_d = \left[I + \frac{\rho q}{E_1^0} Q_0 U\right]^{-1} Q_0 \quad (1.17)$$

$$E_1(\rho) = \frac{Q_{11}^d Q_{22}^d - {Q_{12}^d}^2}{Q_{22}^d} \quad (1.18\text{-a})$$

$$E_2(\rho) = \frac{Q_{11}^d Q_{22}^d - {Q_{12}^d}^2}{Q_{11}^d} \quad (1.18\text{-b})$$

$$G_{12}(\rho) = Q_{66}^d \quad (1.18\text{-c})$$

B. Evolution Law of Delamination

Proceeding crack saturation, in the matrix damage history of events, is local delamination phase. Although observations have confirmed that it is feasible for delaminate damage to occur before saturation [19], even at small stress levels, this model assumes that local delaminate damage would occur after saturation. To describe the evolution of local delamination, the Paris-law, reflected on equation 1.19 was employed. D represents the delamination damage variable, N denotes the cycle number of fatigue loading, and Y is the range of damage evolution variable; A and β are material parameters. The evolution damage variable Y was defined according to 1.20, where Y_{12} and Y_{22} denote the thermodynamic forces relating to damage variables, and k is the coupling parameter. Consequently, using damage mechanics theory, the damage variables could then be expressed as 1.21-a and 1.21-b.

$$\frac{\Delta D}{\Delta N} = A(\Delta Y)^{\beta} \quad (1.19)$$

$$Y = \sqrt{Y_{12} + kY_{22}} \quad (1.20)$$

$$Y_{22} = -\frac{\partial e}{\partial d_{22}^l} = \frac{1}{2}\frac{\sigma_{22}^2}{E_2^0(1-d_{22}^m)(1-d_{22}^l)^2} \quad (1.21\text{-a})$$

$$Y_{12} = -\frac{\partial e}{\partial d_{12}^l} = \frac{1}{2}\frac{\tau_{12}^2}{G_{12}^0(1-d_{22}^m)(1-d_{22}^l)^2} \quad (1.21\text{-b})$$

C. Evolution Law of Fiber Breakage

After the cracks begin to saturate, and delamination occurs, under cyclical loading, fibers become subjected to bearing higher loads. When the local stress experienced by a fiber would reach a critical value, fiber breakage would then occur. Equation 1.22, which represents a brittle failure law, was used to model the initiation of fiber breakage damage, where the bearing stress and the failure strength of the fibers are denoted by σ_f and S_f. As this equation reflects, an increase in bearing stress would be accompanied by a decrease in fiber strength. The quantification of this decrease in fiber strength required the introduction of the residual strength and residual stiffness of a composite laminate, as shown by Equation 1.23. The residual strength and stiffness damage variables are denoted by D_s and D_E, while w represents a material parameter. Subsequently, D_s and D_E are redefined by equations 1.24-a and 1.24-b. The initial longitudinal elastic modulus and failure strength of the composite laminate are denoted by E_1^0 and S_0; E_1^d and S_r represent the damaged longitudinal elastic modulus and strength. E_1^{cr} denotes the critical longitudinal elastic modulus when the composite laminate fails under fatigue loading at the corresponding maximum longitudinal stress σ_{max}. The calculation of the residual strength of a composite laminate under a specific cycle number could then be predicted according to equation 1.25. The laminate was considered to fail when the obtained residual strength was smaller than the applied maximum stress of fatigue loading. Because the previous laws and damage characterization model were established

for an *elementary ply*, coordinate transformation equations would need to be computed to obtain the constitutive equations for plies in laminates oriented at a θ-angle.

$$\frac{\sigma_f}{S_f} = 1 \tag{1.22}$$

$$D_s = (D_E)^w \tag{1.23}$$

$$D_E = \frac{E_1^0 - E_1^d}{E_1^0 - E_1^{cr}} \tag{1.24-a}$$

$$D_S = \frac{S_0^1 - S_r^1}{S_0 - \sigma_{max}} \tag{1.24-b}$$

$$S_r = S_0 - (S_0 - \sigma_{max})\left(\frac{E_1^0 - E_1^d}{E_1^0 - E_1^{cr}}\right)^w \tag{1.25}$$

1.3.3 Structural Failure of Composite Pressure Hulls for Deep-Sea Applications

The most recent available structural failure review, specifically addressing composite pressure hulls for deep-sea applications, is that offered by Li et al [20], whose work is synthesized in this section. Three principal aspects were proposed as the principal structural failure modes: overall buckling failure, material failure, and snap buckling failure. Overall buckling was identified as the dominant failure mode. Experiments involving various cylindrical composites, made from different materials and prepared using different manufacturing processes, were performed to test each of the specimens under external hydrostatic pressure to failure. Notably, some of the most recent work was conducted by Ross and Little [21], Pavlopoulou and Roy [22], and Zhang et al [23]. In these experiments, two main *sub-modes* of failure were observed: elastic (linear) and inelastic (non-linear) buckling. Elastic buckling is based on linear assumptions, and it involves the calculation of the critical buckling load by numerical or analytical methods. Theoretical approaches include the use of the buckling formula to determine the linear buckling load of a composite cylindrical shell. Popular numerical methods include Finite Element Analysis (FEA), identified as the most popular by Luo and Wang [24], specially using commercial software like ABAQUS, ANSYS, or DYNA, and NASTRAN. Results obtained through linear buckling assumptions are the foundation to perform the subsequent inelastic buckling analysis. Inelastic buckling occurs due to the large deformations caused by structural buckling, which are characterized by non-linear effects. Since pressure shells are expected to experience defects during the manufacturing, storage, and assembly process, geometric nonlinearity will occur. As a result, conducting gradual (step-by-step) non-linear simulations is recommended to clearly record the evolution of structural nonlinear buckling.

In the case of thick-walled composite shells, material failure under compression can cause loss of bearing capacity. When a compressive, unidirectional load is applied on a composite structure, along the fiber direction, the fiber behaves like an extended column prone to buckling. Consequently, macro and micro buckling will be the primary failure *sub-modes.* Four were identified as the dominant factors influencing the failure modes of composites under compression: i) material properties, ii) fiber deflection angle, iii) fiber volume content, and iv) defect sensitivity. The principal theoretical methods of prediction for this failure category focus on determining the compressive strength of a unidirectional composite material or shell structures under compression failure. Some of these methods are the elastic microbuckling theory, nonlinear microbuckling theory, three-parameters model, fracture mechanics, FEA, and cumulative damage analysis technology. The third failure mode discussed is snap buckling. This failure mode is unique to

composite pressure hulls exposed to high hydrostatic pressures and an inherently non-linear problem. It can occur with or without initial delamination and lead to instantaneous interlaminar fracture. Implemented approaches to predict damage evolution for a composite material under compressive load include six main approaches, summarized in table 1.2.

Table 1.2 - Main prediction methods for composite materials subject to compressive load [19, 20].

Method	Dominant Use
Elastic Microbuckling theory	Compressive Strength of unidirectional composite material
Nonlinear Buckling theory	
Three Parameters model	
Fracture mechanics method	Compression failure of composite shell structures
Finite element analysis method	
Cumulative damage analysis technology	

Li et all [20] asserted that snap buckling is a unique failure mode of composite shells with large thickness subjected to significant hydrostatic pressures. As the name implies, *snap* refers to instantaneous fracture and can occur without pre-existing delamination. Snap buckling is a non-linear problem, and, unlike *regular* buckling, where the post-deformation shape is somewhat similar to the pre-buckling form, the post-snap buckling shape is radically different from the original configuration. In one key study conducted by Kachanov [24], snap buckling was attributed to delamination coupled buckling. This term refers to gradual process of delamination due to the lower interlaminar strength and the simultaneous buckling of delamination sub-layers. Kachanov proposed to solve this problem theoretically by using a hybrid method combining large deflection theory with the fracture mechanics method. Another recent study was conducted by Lou and Wang [25] who created a model for the inner surface of a composite spherical shell under compression using the principle of elastic similarity. In this work, the coupled buckling concept previously introduced by Kachanov was explored, as well as the effects of delamination thickness and location.

1.3.4 Structural Failure of Titanium Alloys for Deep Sea Applications

The most recent investigation involving implosion of spherical, Titanium Alloy pressure hulls, at the time this report was written, corresponded to that performed by Zheng and Zhao [26]. This mentioned work focused on analyzing the implosion and failure mechanisms of a high-strength/beta annealed titanium alloy Ti-6Al-4V pressure hull in a high-pressure environment. An experimental investigation was first performed and later reconciled with numerical models, which included describing the fluid behavior and structural deformation before, during, and after the failure of the specimen. While details about the fluid behavior and post-implosion interaction are included in Zheng and Zhao's work, this subsection will focus on the elastoplastic deformation and structural failure stage of titanium alloy only. The structural deformation of the titanium alloy sphere was discretized and solved implementing FEM based on OpenRadioss, an open-source solver framework. The elastoplastic deformation of the titanium sphere was modeled by equation

1.26, where σ represents the second Piola-Kirchoff stress tensor component, d is the displacement, f represents the applied force, and ρ is the density of the multiphase flow. The second Piola-Kirchoff stress tensor component is then defined by equation 1.27, where p is the fluid pressure and δ denotes the Piola-Kirchoff function. Once the structure entered the elastoplastic deformation phase, the Johnson-Cook (J-C) constitutive equation was adapted express the equivalent plastic stress $\overline{\sigma}$, as shown by equation 1.28. A, B, C, m, and n represent material parameters measured at or below the transition temperature; $\bar{\epsilon}_{\text{plastic}}$ denotes the equivalent plastic strain, whereas the work and reference equivalent plastic strain rates are denoted by $\dot{\bar{\epsilon}}$ and $\dot{\bar{\epsilon}}_0$. The workpiece, melting, and room temperatures are represented by T, T_m, and T_{room}.

$$\nabla \cdot (\boldsymbol{\sigma} + \boldsymbol{\sigma}\nabla \mathbf{d}) + \mathbf{f} = \rho \frac{\partial^2 \mathbf{d}}{\partial t^2} \tag{1.26}$$

$$\sigma = -p\delta \tag{1.27}$$

$$\overline{\sigma} = \left(A + B\overline{\epsilon^n}_{\text{plastic}}\right)\left(1 + C \ln \frac{\dot{\bar{\epsilon}}}{\dot{\bar{\epsilon}}_0}\right)\left[1 - \left(\frac{T - T_{room}}{T_{melt} - T_{room}}\right)^m\right] \tag{1.28}$$

Similarly, the J-C failure criteria was used to model the structural failure of finite elements in the structure, where under the current strain rate, temperature, pressure, and equivalent stress conditions, the equivalent failure strain expression was defined according to equation 1.29. Here, the material parameters D_1 through D_5 are measured at or below the transition temperature, and the stress triaxiality is defined as the ratio of the pressure to equivalent plastic stress, $\dot{\sigma} = P/\overline{\sigma}$. When the damage parameter of a unit element in equation 1.30 became equal to 1, the material stiffness gradually disappeared, in accordance with explicit dynamics method, specified in OpenRadioss solver. The material stiffness was assumed to degrade progressively until reaching failure. Because the proposed model considered the effect of equations of state to describe the post-implosion deformation of the titanium structure, the Grüneisen model was implemented in the numerical simulation. More specifically, equation 1.31 was employed as the equation of state for titanium alloy during its compression. ρ_s denotes the density, C represents the speed of sound, γ_s is the Grüneisen coefficient, a is a first-order volume correction to γ_s, and S is a material parameter. Parameter μ is defined by equation 1.32, where $\rho_{s,t}$ and ρ_s denotes the current and initial densities of the structure.

$$\overline{\epsilon}_{\text{failure}} = [D_1 + D_2 \exp D_3 \dot{\sigma}]\left(1 + D_4 \ln \frac{\dot{\bar{\epsilon}}}{\dot{\bar{\epsilon}}_0}\right)[1 + D_5(\frac{T - T_{room}}{T_{melt} - T_{room}})] \tag{1.29}$$

$$D = \sum \frac{\Delta\epsilon}{\overline{\epsilon}_{\text{failure}}} \tag{1.30}$$

$$p_s = \rho_s C^2 \mu\left[1 + \left(1 - \frac{\gamma_s}{2}\right)\mu - \frac{a}{2}\mu^2\right] / [1 - (S - 1)\mu]^2 + \gamma_s E \tag{1.31}$$

$$\mu = \frac{\rho_{s,t}}{\rho_s} - 1 \tag{1.32}$$

1.3.5 Structural Studies of Acrylic Windows for Deep Sea Applications

Similarly, the most recent available literature exploring the deformation of an observation window in a deep-sea vehicle was conducted by He et al [27]. In this mentioned investigation, a finite element model was developed with ABAQUS 2022 and validated through experimental data. More specifically, a polymethyl methacrylate (PMMA) frustum observation window of a manned

submersible, designed according to ASME-PVHO-1, was modeled as illustrated in Figure 1.4. In this schematic, D_i, α, t, and R, represent the initial diameter, cone angle, thickness, and arc transition radius, respectively. To simulate the hydrostatic pressure and thermal loading pertaining to deep-sea environment, a parametric analysis implementing temperature combinations ranging between 2 to 30° Celsius, loading rates between 2.3 to 8 MPa/min, and friction coefficients values from 0.05 to 0.3 was conducted.

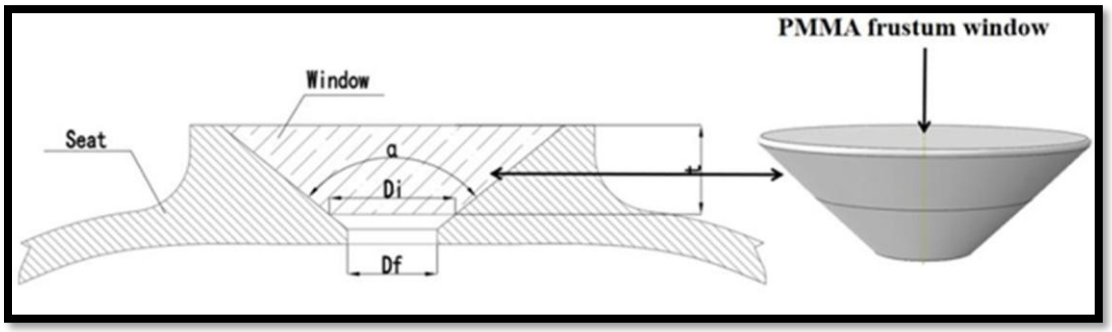

Figure 1.4 - Basic structural parameters of frustrum observation window from [27].

He et al [27] signaled that in the time-hardening theory, for an isothermal process, the relationship between the stress σ, creep rate $\dot{\epsilon}_{cr}$, and time, t, can be expressed according to equations 1.33 to 1.35. The stress and time-response functions are denoted by $f_1(\sigma)$ and $f_2(t)$, respectively, where n, A, and m represent exponential parameters. A temperature-dependent time-hardening model was then developed by introducing the creep strain rate and subsequently material parameters, as expressed in equations 1.36 through 1.38. $\dot{\epsilon}_{cr}$ denotes the creep strain rate; σ is the uniaxial stress; t is the total time; T is the temperature; $a_1, b_1, c_1, k_1, d_1, n, a_2, b_2, c_2$, and k_2 are material parameters. By integrating the creep strain from equation 1.37, equations 1.39a through 1.39c could then be obtained, where C is an integral constant dependent on the elastic strain before loading. Lastly, the material constants required for the model were obtained by implementing the nonlinear least square method with compression creep test data for the PMMA material at different temperatures.

$$\Phi = (\dot{\epsilon}_{cr}, \sigma, t) = 0 \quad (1.33)$$

$$\epsilon = f_1(\sigma) \cdot f_2(t) \quad (1.34\text{-a})$$

$$f_1(\sigma) = \sigma^n \quad (1.34\text{-b})$$

$$f_2(t) = \frac{A}{m+1} t^{m+1} \quad (1.34\text{-c})$$

$$\epsilon_{cr} = \frac{A}{m+1} \cdot \sigma^n \cdot t^{m+1} \quad (1.35)$$

$$\dot{\epsilon}_{cr} = A\sigma^n t^m \quad (1.36)$$

$$\epsilon_{cr} = A\sigma^n t^{m+1} + C \quad (1.37)$$

$$\dot{\epsilon}_{cr} = (a_1 T^3 + b_1 T^2 + c_1 T + k_1 \sigma + d_1)\sigma^n t^{(a_2 T^2 + b_2 T + k_2 \sigma + c_2)} \quad (1.38)$$

$$\epsilon_{cr} = A\sigma^n t^{m+1} + C \quad (1.39\text{-a})$$

$$A_1 = a_1 T^3 + b_1 T^2 + c_1 T + k_1 \sigma + d_1 \quad (1.39\text{-b})$$

$$m_1 = a_2 T^2 + b_2 T + k_2 \sigma + c_2 \quad (1.39\text{-c})$$

1.4 Project Proposal

The accurate modeling and prediction of the structural response of a HOV in deep-sea environments is indispensable to ensure the safety of its occupants. Before ceasing operations, OceanGate, as a private company, maintained design selections and technical details confidential from the public, despite warnings that implementing that design was “safe” for its occupants. At the time this report was proposed, no structural studies to corroborate its safety had been made available to the public. Consequently, this work seeks to reproduce a simplified geometry model of the Titan Submersible and generate the static structural response at its lowest operational depth, which is 4km. This analysis is to be conducted by comparing an analytical method for cylindrical composites to a FE model in Ansys. Potential troubling areas will be identified and design recommendations will be made.

1.5 Methodology

In more detail, the operational, simplified design geometry of the Titan submersible will first be reproduced using SolidWorks ®. A finite Element Method (FEM) will be developed and implemented in Ansys. Once results are generated and found satisfactory, convergence studies will be performed to identify the most stable numerical solution. This process then will be repeated implementing modifications in accordance with the test matrix summarized in table 1.3.

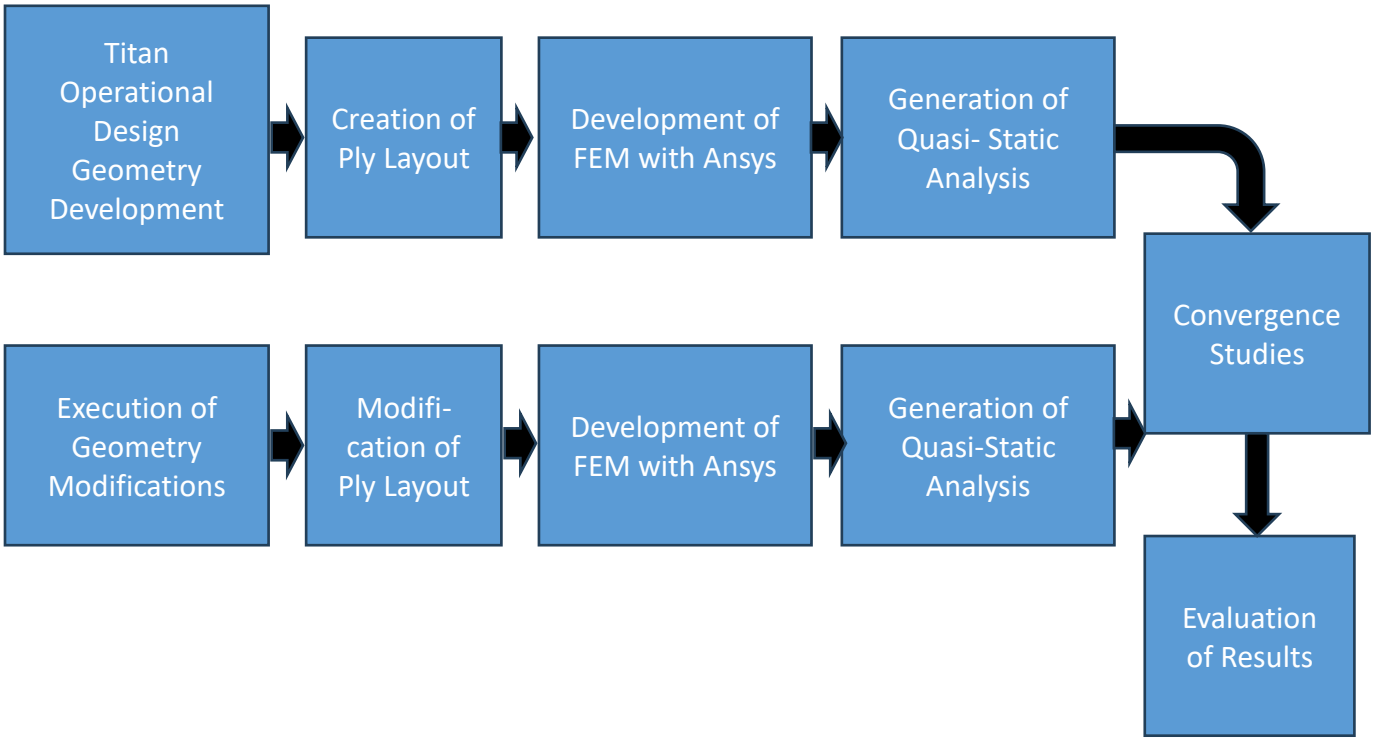

Figure 1.5 - Workflow Diagram of the Proposed Investigation.

Table 1.3 - Design of experiments matrix.

Case	Modification
1	1.5x thickness increase in thickness in pressure hull and titanium hemispheres
2	3.0x thickness increase in thickness in pressure hull and titanium hemispheres
3	Nominal Thicknesses, ply layout [0, 30, 60, 90]s, ceteris paribus
4	Ply layout [0, 30, 60, 90]s; 1.5x global thickness increase
5	Ply layout [0, 30, 60, 90]s; 3.0x global thickness increase
6	Replacement of Carbon Pressure Hull for Titanium

1.6 Conclusions

The presented literature review has focused on introducing the reader to appropriate background information about the Titan Submersible incident, its main physical characteristics, and principal constituent materials. Various theoretical failure theories of the two main dominant constituents, carbon fiber and titanium were explored, and a brief study about modeling of creep behavior in acrylic observation windows was included. Moreover, the relatively potent and sophisticated computational tools enjoyed by modelers and investigators of composite structural failure represents a great advantage to advance the understanding and predicting capabilities in today's world. These numerical tools and methods will be leveraged in this study to provide curious readers and future designers of HOVs with more insights about the effects of various design configurations involving carbon-fiber composites and titanium alloy.

2. Finite Element Method Overview

2.1 Finite Element Method Overview

The inherent complexity arisen when modeling physical processes in three-dimensional space has pushed the scientific community to develop various methods of numerical analysis, such as Finite Difference, Finite Volume and Boundary Element Method. Arguably, however, the Finite Element Method (FEM) has become the approach of choice to solve a wide variety of problems that can be described in terms of partial differential equations or integral expressions. Its impact in the field of structural analysis -along with other engineering disciplines- has been analogous to a quantum leap in scientific modeling and engineering design in the past century; nonetheless, its usefulness and applicability continue to resonate today. By considering the historical background, key developments, and areas of potential improvement, an analyst reader can gain a deeper understanding of the architecture of this powerful engineering method, its advantages and limitations, and think about alternatives to improve its efficiency and accuracy. Aiming to broaden the scope of this investigation, this section seeks to provide a synopsis of the historical overview and future of the FEM. Additionally, fundamental concepts of Finite Element Analysis (FEA) and its specific implementation in the field of Structural Mechanics in Ansys will be discussed.

Several individuals have contributed to the birth, development, and sophistication of the FEM as it is known today. Some scholars, like Oden [28], argue that an analogous idea to FEA can be traced back to the work of German mathematician Karl Schellback, whom in 1851 proposed discretizing a surface using right triangles to find the minimum surface area within a boundary. Approximating a differential equation with a set of algebraic equations was an intrinsic concept of FEA. Almost a century later, in 1943, Richard Courant of New York University determined the torsional rigidity of a hollow shaft through the Riley-Ritz method, where the cross-section of the shaft was divided into triangles, and the stress function was interpolated linearly at each of the nodes. In the 1950s, academics and private-sector engineers further developed Courant's early concepts to solve problems in civil and aeronautical engineering applications. One of them was John Argyris of the Imperial College of London, who created an energy method for structural analysis, which enabled FEM for three-dimensional elements in the 1950s. The second is Ray Clough, of UC Berkeley, who in the 1960s derived the *stiffness matrix* of an element in a continuum in the. Thirdly is Olgierd Zienkiewicz, of Northwestern University, who in collaboration with J. Z. Zhu, formulated an error estimation technique, which served as a quality control to the FEM solutions and implemented the concept of adaptive mesh refinement by the 1990s. Lie et al [29] asserted that three previous individuals could be credited with making the most "pivotal, critical, and significant contributions to the birth and early development of the FEM." Lastly, early developments of FEM were complimented by the development of the first general-purpose computer code, which was developed by structural engineers John Tinsley Oden and G. C. Best in the 1960s. The elements in this program library contained elements for 2D elasticity, 2D plane elasticity, 3D beam and rod elements, and elements for general composite materials [30].

The time spanning the 1960s to the 1990s witnessed crucial advancements in FEM methodology improvements and applications. One of these was the implementation of explicit, implicit-explicit, or implicit time integration with damping control to solve nonlinear structural dynamics problems, proposed by T. Belytschko, K. C. Park, and T. J. Hughes [29]. In fields such as fluid mechanics, FEM started to be implemented to solve the Navier-Stokes equations as an

alternative to finite difference and finite volume methods; this was preceding effort to the subsequent development of FEM solvers for fluid-structure interactions. Another significant development was the formulation of the Arbitrary Lagrangian-Eulerian (ALE) based FEM formulations in engineering simulation. This technique enabled the mesh domain to move arbitrarily to optimize the shape of the elements, ultimately leading to improved accuracy and numerical convergence. Lastly, in the 1980s, the development of nonlinear probabilistic FEM enabled the quantification and inclusion of uncertainty in major problem simulation parameters, such as loading conditions, material behavior, and geometric configuration. Almost parallel to these events was the development of FEM software technology. On the private sector, in 1963, the MacNeal-Schwedler Software Corporation (MSC) developed its FEM code Structural Analysis by Digital Simulation of Analog Methods (SADSAM), whereas NASA completed its own FEM code NASTRAN (NASA STRuctural Analysis) by 1969. During the same decade, John Swanson, a then Westinghouse mechanical engineer, left the company and developed its own *ANSYS* FEM code [31]. Moreover, Livermore National Laboratories also developed a 2D Nonlinear FEM code called DYNA3D; later, it evolved into LS-DYNA. This technology was bought and incorporated into ANSYS software, as ANSYS LS-DYNA in 2018. Moreover, in the 1970s, David Hibbitt, Bengy Karlsson, and Paul Sorensen created a company called HKS, which released a commercial FEM software called ABAQUS. Today, ABAQUS and ANSYS are arguably the two most popular FEM software used by academia and the private sector, aiding investigators to model and approximate solutions to many complex engineering problems.

The present and future FEM areas of research seem to be focused on two principal aspects. First is the study of the various forms of machine and deep-learning methods [29]. This area of research seeks to design and train a neural network to approximate any given continuous function to an arbitrary level of accuracy, solve high dimensional PDEs in strong form, and accelerate convergence of the solution. This process is expected to generate new discoveries, create more robust numerical approximation techniques, and procure the development of more efficient discretization processes. Secondly is the merging of deep machine learning methods with reduced order modeling methods. More specifically, this research aims to enable high-resolution topology design while maintaining a high level of speed and accuracy in the computed solution. Reducing the computational cost is expected to facilitate the demand between sensors, control algorithms, and simulation architectures, such as interactions between automated driving control (autonomous vehicles) and structural health monitoring systems.

2.2 Fundamental Elements of Finite Element Method

Most real-world problems involve complex geometries, non-isotropic material composition, and loading conditions that cannot be solved with using conventional analytical methods. In this case, by developing and implementing an appropriate simplified physical model of the system of interest, the FEM can provide an approximate solution to the problem at hand.

2.2.1 Fundamental Principles of FEA

The fundamental concept of the FEM, as signaled in the previous subsection, is the idea that a continuum can be discretized into a finite number of elements. A physical element, such as the post in figure 2.1a, consists of an infinite number of points, able to displace in an infinite

number of directions upon the application of forces. Interaction of a physical element and its constituents with forces, subject to constraints, can be represented mathematically through a Boundary Value Problem (BVP), where physical phenomena in an arbitrarily defined region can be described through differential equations. The investigation of a field variable, such as displacement, in structural mechanics, or temperature, in fluid mechanics, is the main objective of the analysis. In the case of the discussed post, a FE analysis can be achieved by representing the post with three line-elements of different cross-sectional areas, connected at nodes, and subject to a pressure applied on top of element 1, as element 3 remains fixed, as shown in Figure 2.1b. This representation enables the analysis of a system with a finite number of elements restricted to moving in a selected number of degrees of freedom. Applying the FEA to an analyzed system implies approximating numerically the field variable at the nodes of the discretized domain.

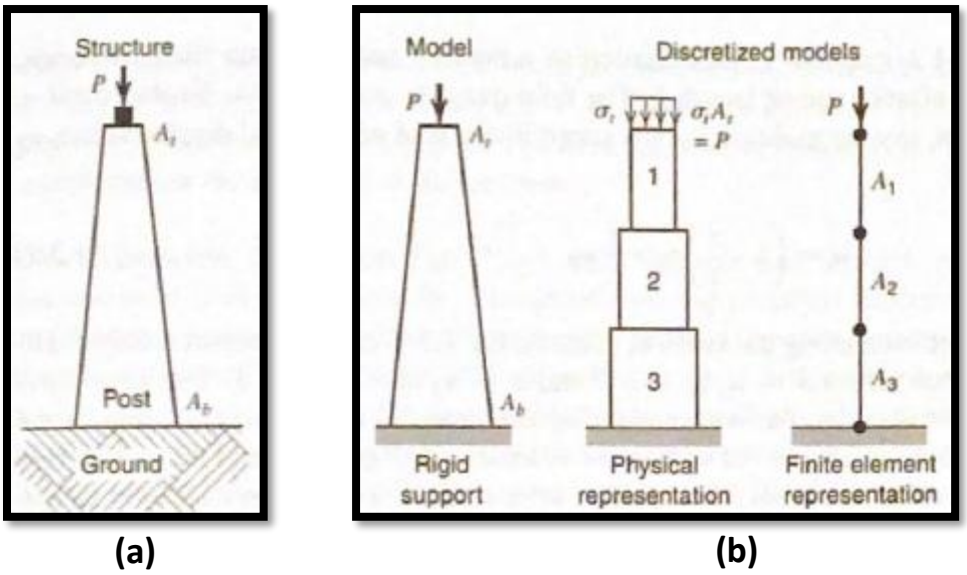

Figure 2.1 - Modeling and FE representation of a structure [32].

In linear-static analysis, an underlying principle to investigate the nodal displacements is the analogy to Hook's law, represented by equation 2.1, and written, for convenience, in matrix form. Here, f represents the applied force, k the stiffness, and x the displacement for each element, denoted by the subscript i. As summarized by this equation, each nodal element is assumed to have an associated stiffness resisting the motion as a response to an applied force. As will be discussed in the proceeding section, each corresponding element in the discretized domain is then represented in a *global stiffness matrix,* where each individual element is converted from a local coordinate system to a global coordinate system through transformation matrices. This global stiffness matrix is represented by equation 2.2. Inverting the matrix, as denoted by equation 2.3, leads to determining the value of each nodal displacement. The displacements at the non-nodal points are then approximated through piece-wise interpolation of polynomial functions, such as those in the form of equation 2.4. Additional properties of interest, such as strains and stresses can then be determined after the prediction of this main field quantity.

$$\{f\}_i = [k]_i\{x\}_i \quad (2.1)$$

$$\{F\} = [K]\{X\} \quad (2.2)$$

$$[X] = [K]^{-1}[F] \quad (2.3)$$

$$\phi(x, y) = N_1(x, y)\phi_1 + N_2(x, y)\phi_2 \quad (2.4)$$

Four popular formulation techniques are used to obtain the series of equations to assemble the global stiffness matrix for a finite elements grid in a BVP: i) equilibrium, ii) direct stiffness, iii) variational methods, and iv) weighted residuals. The first two are limited to the analysis of the simplest forms of geometry, such as bar elements or trusses. Variational methods, such as the principle of stationary potential energy, can be used to analyze most BVPs involving more complex types of geometries. Weighted residual methods, such as the Galerkin or least-squares, can be used for any type of BVP. To demonstrate the essential mathematical process of FEA on a simple element, the direct stiffness method is used in the proceeding paragraphs to predict the displacement of six nodal locations when a force, P, is applied to the post in figure 2.2a. This structure possesses a uniform circular cross-sectional area, which decreases linearly from a value A, at the base, to a value $A/3$ at the top. The analyzed structure is assumed to be isotropic, behave linear-elastically, and have the characteristics described in table 2.1. Only axial displacements are allowed in this analysis.

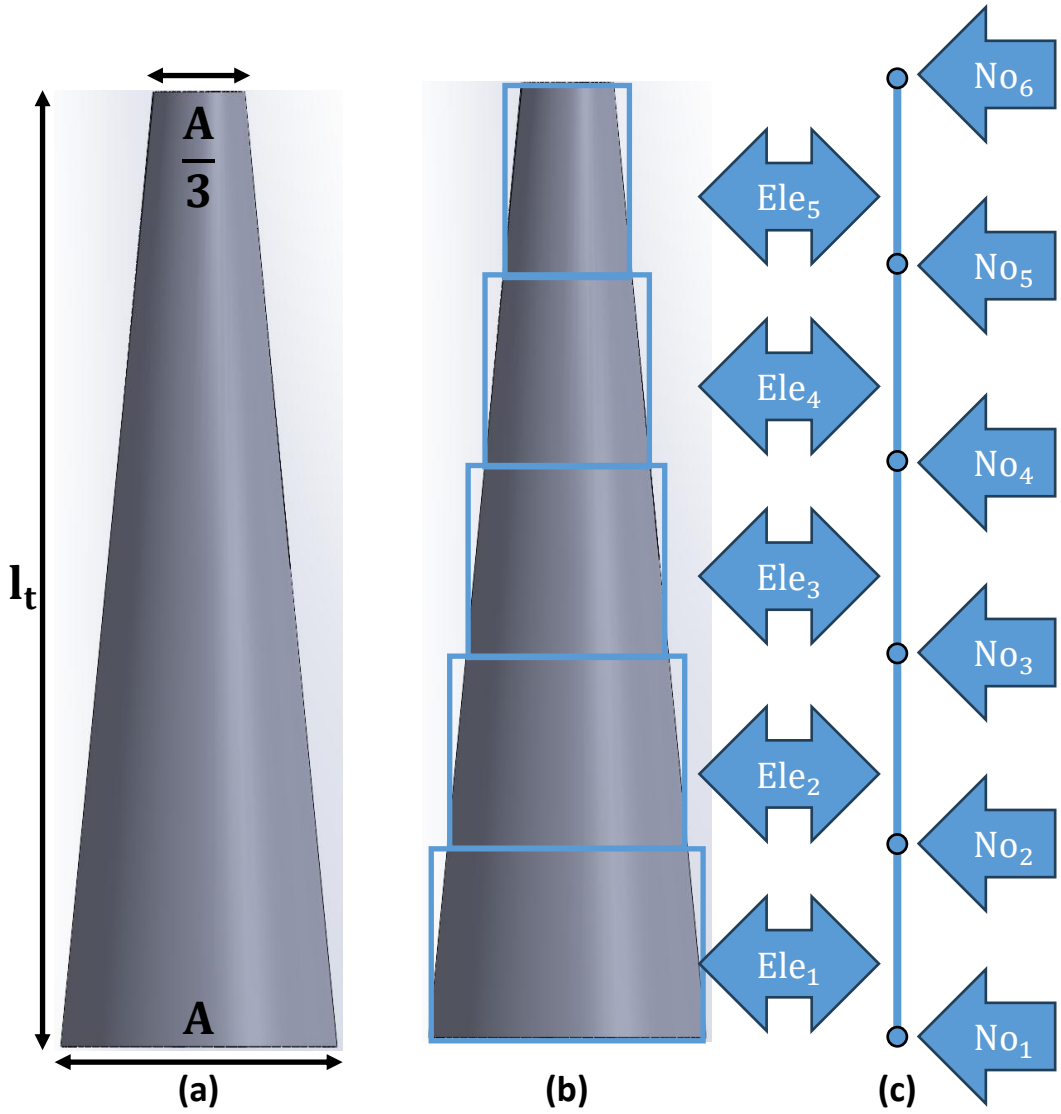

Figure 2.2 - (a) Geometrical representation of the structure, (b) Discretization into 5 finite elements, and (c) Corresponding nodal locations.

Table 2.1 - Characteristics of the conceptual structure.

Property	Units	Value
Material	Steel AISI 302	
Base Diameter	m	0.3
Base Cross-sectional Area, A	m^2	0.0707
Bar Length, l_t	m	1
Youngs Modulus, E	Pa	180E9
Applied Load, P	N	981

The FEA starts with the discretization of the conceptual structure into a finite number of elements. Specifically, the geometry is discretized into five elements, as denoted by the abbreviation "Ele_i" in figure 2.2b; this corresponding discretization yields to six nodal locations, where the displacements are to be investigated. Nodal locations are denoted by "No_i" in figure 2.2c. For a single bar element, such as that in Figure 2.3a, subject to axial forces at nodal locations 1 and 2, the corresponding free-body diagrams are represented in Figure 2.3b. As a result, for element 1, Newton's second law can be expressed by equation 2.6, where F_1 is the force applied to the nodal location, σ is the stress, and A is the cross-sectional area. The stress, σ, can then be described by equation 2.7, in terms of the Youngs Modulus E and the strain ϵ. In Equation 2.8, the strain ϵ can be expressed in terms of the nodal displacements at node 2, u_2, and node 1, u_1, divided by the element length L. Substituting equations 2.7 and 2.8 into 2.6, and defining the stiffness k according to 2.9, leads to equation 2.10. Similarly, at the second nodal element, Newton's second law is written as Equation 2.11, where F_2 is the force applied to this nodal location. Solving for F_2 and substituting the relations of equations 2.7 through 2.9, yields equation 2.12. Finally, expressing equations 2.10 and 2.11 as matrices leads to expression 2.13, where the 2x2 matrix represents the stiffness matrix of a bar element. When only axial displacements are allowed, as is the case with the analyzed post, the global stiffness matrix can be assembled by appending the individual stiffness matrices of each element, as shown by equation 2.14, so that the global stiffness matrix takes the form of 2.15. Now, including the displacements and forces matrices, denoted by 2.16 and 2.17, the system of equations can take the form reflected by 2.18.

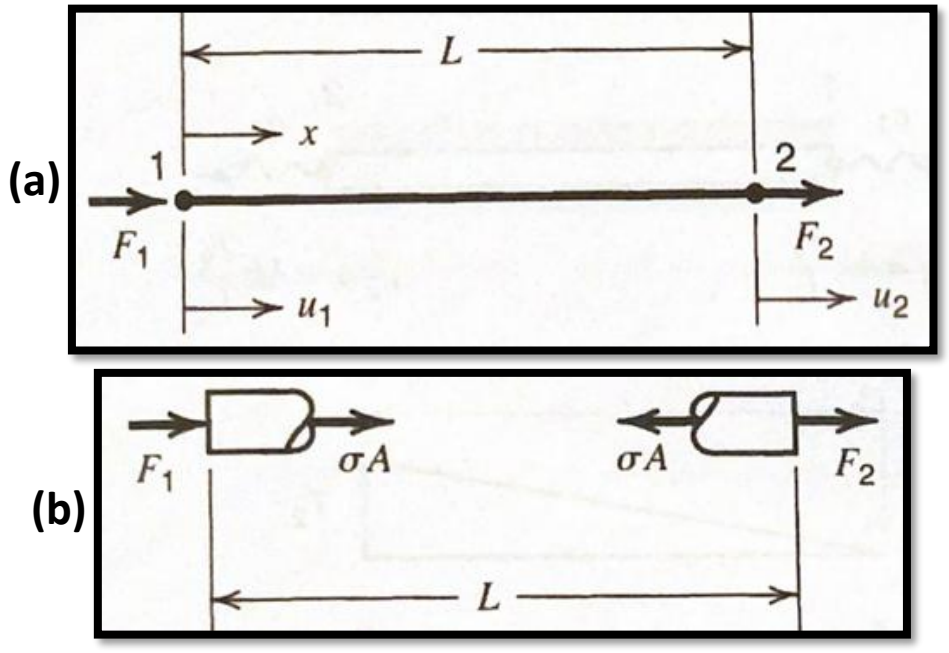

Figure 2.3 - (a) Single Bar Element and (b) Free Body Diagram.

At Node 1

$$\Sigma F_{No_1} = 0 = F_1 + \sigma A \tag{2.6}$$

$$\sigma = E\epsilon \tag{2.7}$$

$$\epsilon = \frac{u_2 - u_1}{L} \tag{2.8}$$

$$k = \frac{AE}{L} \tag{2.9}$$

$$F_1 = ku_1 - ku_2 \tag{2.10}$$

At Node 2

$$\Sigma F_{No_2} = 0 = F_2 - \sigma A \tag{2.11}$$

$$F_2 = -ku_1 + ku_2 \tag{2.12}$$

$$\begin{bmatrix} k & -k \\ -k & k \end{bmatrix} \begin{Bmatrix} u_1 \\ u_2 \end{Bmatrix} = \begin{Bmatrix} F_1 \\ F_2 \end{Bmatrix} \tag{2.13}$$

$$[\mathbf{K}] = [k_{el1}] + [k_{el2}] + [k_{el3}] + [k_{el4}] + [k_{el5}] \tag{2.14}$$

$$[\mathbf{K}] = \begin{bmatrix} k_1 & -k_1 & 0 & 0 & 0 & 0 \\ -k_1 & k_1 + k_2 & -k_2 & 0 & 0 & 0 \\ 0 & -k_2 & k_2 + k_3 & -k_3 & 0 & 0 \\ 0 & 0 & -k_3 & k_3 + k_4 & -k_4 & 0 \\ 0 & 0 & 0 & -k_4 & k_4 + k_5 & -k_5 \\ 0 & 0 & 0 & 0 & -k_5 & k_5 \end{bmatrix} \tag{2.15}$$

$$[X] = [u_1 \quad u_2 \quad u_3 \quad u_4 \quad u_5 \quad u_6]^T \tag{2.16}$$

$$[F] = [f_1 \quad f_2 \quad f_3 \quad f_4 \quad f_5 \quad f_6]^T \tag{2.17}$$

$$\begin{bmatrix} k_1 & -k_1 & 0 & 0 & 0 & 0 \\ -k_1 & k_1 + k_2 & -k_2 & 0 & 0 & 0 \\ 0 & -k_2 & k_2 + k_3 & -k_3 & 0 & 0 \\ 0 & 0 & -k_3 & k_3 + k_4 & -k_4 & 0 \\ 0 & 0 & 0 & -k_4 & k_4 + k_5 & -k_5 \\ 0 & 0 & 0 & 0 & -k_5 & k_5 \end{bmatrix} \begin{bmatrix} u_1 \\ u_2 \\ u_3 \\ u_4 \\ u_5 \\ u_6 \end{bmatrix} = \begin{bmatrix} f_1 \\ f_2 \\ f_3 \\ f_4 \\ f_5 \\ f_6 \end{bmatrix} \tag{2.18}$$

Once the system of equations has been assembled, the corresponding boundary conditions need to be applied. For a fixed post, the displacement of nodal element 1, which is fixed to the ground, is 0, expressed by equation 2.19. Node 1 also experiences a reaction force, denoted by R_1 in equation 2.20. The only applied force occurs at nodal location 6, as expressed by 2.21 and 2.22. Implementing these set of constraints into 2.18 leads to the new system of equations expressed by 2.19. Since the reaction is unknown at this at this point, and the first nodal displacement is 0, the first row and column of 2.19 are removed from the system, leading to 2.20. Solving by inverting the matrix leads to the displacements, in meters, expressed on 2.21. Finally, by substituting these displacements back into equation 2.19, the reaction force can be solved, and is equal to 850.2 N. The corresponding MATLAB code implemented to solve this problem can be found in section 1 of the Appendix.

$$u_1 = 0 \tag{2.19}$$

$$f_1 = R_1 \tag{2.20}$$
$$f_6 = -P \tag{2.21}$$
$$f_2 = f_3 = f_4 = f_5 = 0 \tag{2.22}$$
$$\begin{bmatrix} k_1 & -k_1 & 0 & 0 & 0 & 0 \\ -k_1 & k_1+k_2 & -k_2 & 0 & 0 & 0 \\ 0 & -k_2 & k_2+k_3 & -k_3 & 0 & 0 \\ 0 & 0 & -k_3 & k_3+k_4 & -k_4 & 0 \\ 0 & 0 & 0 & -k_4 & k_4+k_5 & -k_5 \\ 0 & 0 & 0 & 0 & -k_5 & k_5 \end{bmatrix} \begin{bmatrix} 0 \\ u_2 \\ u_3 \\ u_4 \\ u_5 \\ u_6 \end{bmatrix} = \begin{bmatrix} R_1 \\ 0 \\ 0 \\ 0 \\ 0 \\ -P \end{bmatrix} \tag{2.19}$$

$$\begin{bmatrix} k_1+k_2 & -k_2 & 0 & 0 & 0 \\ -k_2 & k_2+k_3 & -k_3 & 0 & 0 \\ 0 & -k_3 & k_3+k_4 & -k_4 & 0 \\ 0 & 0 & -k_4 & k_4+k_5 & -k_5 \\ 0 & 0 & 0 & -k_5 & k_5 \end{bmatrix} \begin{bmatrix} u_2 \\ u_3 \\ u_4 \\ u_5 \\ u_6 \end{bmatrix} = \begin{bmatrix} 0 \\ 0 \\ 0 \\ 0 \\ -P \end{bmatrix} \tag{2.20}$$

$$[u_2\ u_3\ u_4\ u_5\ u_6]^T = 1 * 10^{-6}[-0.0154, -0.0332, -0.0542, -0.0799, -0.1130]^T \tag{2.21}$$

In contrast, the analytical exact displacements for this bar under an axial load can be determined using Euler-Bernoulli beam theory, which is represented by equation 2.22. Using the fundamental theorem of calculus, the integration of 2.22 leads to equation 2.23. Repeating this process once more leads to equation 2.24. After applying the corresponding boundary conditions reflected by equations 2.25, the force P applied at the top of the bar, and no displacement at its base, the corresponding constants of integration are found in equation 2.26. Integrating these results, the axial displacement of the bar can be described analytically by equation 2.27. Plotting and comparing these results to those generated by FEM, as in figure 2.4, reveals that FEM results under-predict the displacements.

$$-\frac{d}{dx}\left[EA(x)\frac{du}{dx}\right] = 0 \tag{2.22}$$
$$EA(x)\frac{du}{dx} = c_1 \tag{2.23}$$
$$u(x) = \frac{3l_t c_1 \ln(3l_t - 2x)}{2EA} + c_2 \tag{2.24}$$
$$\left(EA(x)\frac{du}{dx}\right)_{x=l_t} = P, \qquad u(0) = 0 \tag{2.25}$$
$$c_1 = P, \qquad c_2 = \frac{3l_t P}{2EA}\ln(3l_t) \tag{2.26}$$
$$u(x) = \frac{3l_r P}{2EA}\ln\left(\frac{3l_t}{3l_t - 2x}\right) \tag{2.27}$$

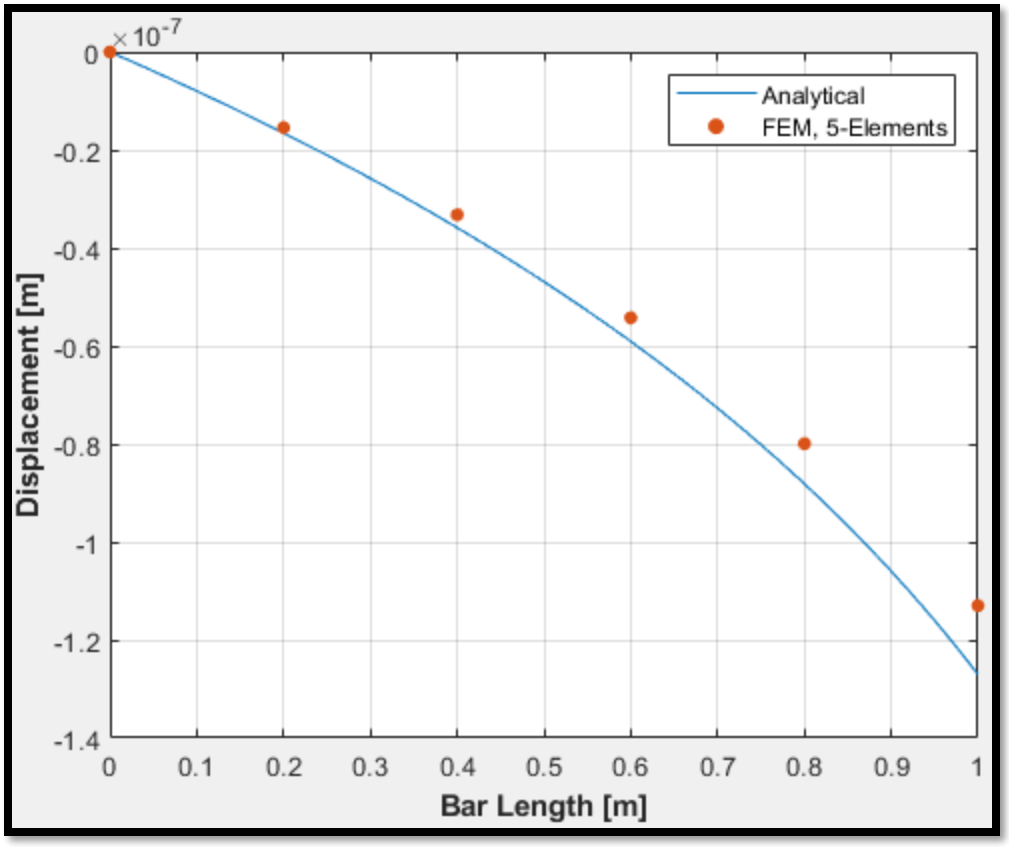

Figure 2.4 – Analytical displacements using Euler-Bernoulli beam theory versus FEM with 5 elements.

When encountering more complex geometries, equilibrium or direct stiffness method cannot be used to derive the stiffness matrix. As a result, in most FEA applications, variational methods are typically used to derive the stiffness matrix of a system. To do this, a functional is required. This is an expression that contains the governing differential equations of the studied BVP. Implementing the principle of stationary potential energy yields a functional required to conduct stress analysis. This principle states that, from all the admissible displacements a system can achieve, the equilibrium displacement minimizes its total potential energy. Admissible displacements are displacements that satisfy the boundary conditions and compatibility condition (or physical continuity of the material). This was illustrated by Cook [32], as shown in Figure 2.5b, where the upper line shows a crack, at location A, and a kink, at B, which would violate the material continuity. - The formulation of residual methods can be found in chapter 5 of Cook et al [32], but its discussion will be excluded from this work.

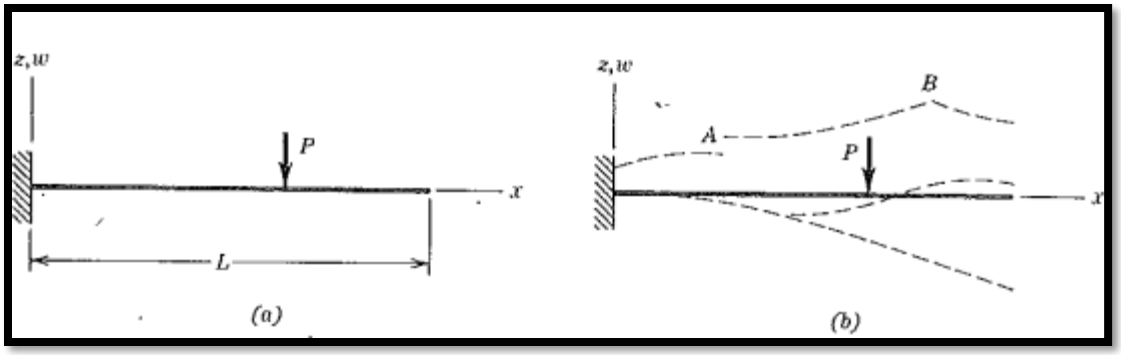

Figure 2.5 - (a) Cantilever beam. (b) One inadmissible configuration (upper dashed line) and two admissible configurations (lower dashed lines) [32].

In a system consisting of a linear spring, which is stretched by an applied force, as shown in Figure 2.6, its associated displacement can be investigated as follows. The potential energy Π_P is the sum of the internal strain energy U, and the external potential energy Ω (2.5). U and Ω are defined by equations 2.6 and 2.7, respectively, where k is the spring stiffness, D represents the associated displacement, and P is the applied force. Deriving equation 2.5 with respect to x leads to equation 2.9, where subsequently solving for the displacement, D, leads to equation 2.10. When these functions are shown graphically, as in figure 2.7, the minimum potential energy represents the equilibrium displacement of the system.

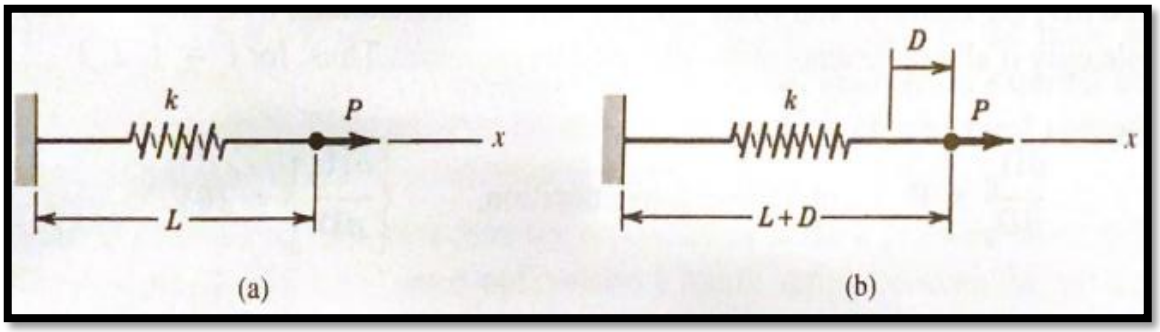

Figure 2.6 - (a) Reference configuration of a linear spring system. (b) Stretched configuration after application of force P [32].

$$\Pi_P = U + \Omega \quad (2.5)$$

$$U = \frac{1}{2}kD^2 \quad (2.7)$$

$$\Omega = -PD \quad (2.8)$$

$$\frac{d\Pi_p}{dD} = kD_{eq} - P = 0 \quad (2.9)$$

$$D_{eq} = \frac{P}{k} \quad (2.10)$$

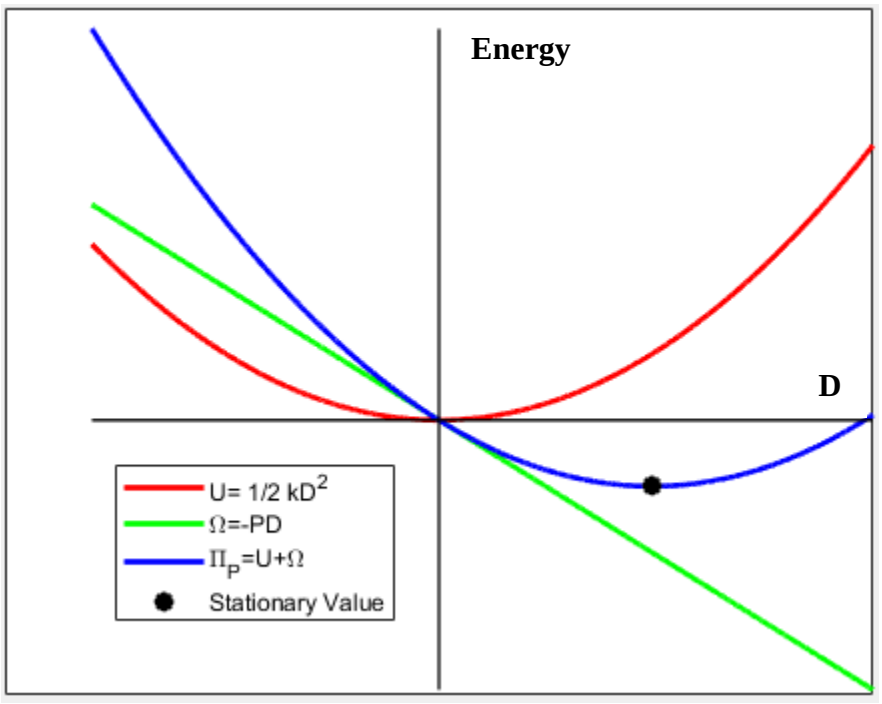

Figure 2.7 - Representation of the principle of stationary potential energy.

The previous simple system consisting of a single element is the foundation for the analysis of a mesh grid with hundreds or thousands of degrees of freedom. This was explained by Cook [32] as follows. In a system consisting of n degrees of freedom, the displacement vector D, containing admissible configurations only, has the form of equation 2.11. Since the potential energy of a system depends only on the corresponding nodal displacements of the system, or degrees of freedom, the total potential energy can be written as 2.12. Applying the principle of stationary potential energy leads to equation 2.13. Because each dD_i term is independent from the other elements and nonzero, only their corresponding coefficients, $\frac{\partial \Pi_p}{\partial D_i}$, can be zero. This fact can be written in the form of equation 2.14. The complete derivation of the stiffness matrix using the principle of potential energy of an elastic body can be found in chapter 4.4 of [32]. The results, however, reflect that the stiffness matrix [K] can be generated by equation 2.15, where [B] represents the stress-displacement matrix, denoted by equation 2.16. In three dimensions, the partial $[\partial]$ is equal to the elements contained in 2.17, namely the partial derivative operators or each corresponding direction. [N] denotes the matrix shape function, which contains the corresponding nodal locations, as equation 2.18. Moreover, the force vector {f} can be expressed as equation 2.19, where $\{f_b\}$, $\{f_s\}$, and $\{f_p\}$ denote the body forces, surface tractions, and point loads, respectively. Matrix {u} denotes the nodal displacements; after being evaluated, the corresponding strains and stresses can be determined by equations 2.21 and 2.22. The constitutive matrix is represented by [E], and the initial stresses and strains are denoted by $\{\sigma_0\}$ and $\{\epsilon_0\}$.

$$\{D\} = [D_1\ D_2\ \dots D_n]^T \tag{2.11}$$

$$\Pi_P = (D_1, D_2, \dots, D_n) \tag{2.12}$$

$$d\Pi_p = \frac{\partial \Pi_p}{\partial D_1} dD_1 + \frac{\partial \Pi_p}{\partial D_2} dD_2 + \cdots + \frac{\partial \Pi_p}{\partial D_n} dD_n \tag{2.13}$$

$$\left\{\frac{\partial \Pi_p}{\partial \mathbf{D}}\right\} = \{0\} \tag{2.14}$$

$$[K] = \int_V [B]^T [D][B] dV \tag{2.15}$$

$$[B] = [\partial][N] \tag{2.16}$$

$$[\partial] = \begin{bmatrix} \frac{\partial}{\partial x} & 0 & 0 \\ 0 & \frac{\partial}{\partial y} & 0 \\ 0 & 0 & \frac{\partial}{\partial z} \\ \frac{\partial}{\partial y} & \frac{\partial}{\partial x} & 0 \\ 0 & \frac{\partial}{\partial z} & \frac{\partial}{\partial y} \\ \frac{\partial}{\partial z} & 0 & \frac{\partial}{\partial x} \end{bmatrix} \tag{2.17}$$

$$[N] = [N_1 N_2 \cdots] \tag{2.18}$$

$$\{f\} = \int_V [N]^T \{f_b\} dV + \int_V [N]^T \{f_s\} dV + \{f_p\} \tag{2.19}$$

$$\{u\} = [N]\{d\} \tag{2.20}$$

$$\{\epsilon\} = [\partial]\{u\} \tag{2.21}$$

$$\{\sigma\} = [E](\{\epsilon\} - \{\epsilon_0\}) + \{\sigma_0\} \tag{2.22}$$

2.2.2 Basic Elements

As previously mentioned, partitioning a continuum implies dividing a bounded region into smaller units – or finite elements, - which are connected to neighboring elements at nodes and boundary lines. Depending on the dimensionality and desired analysis of the domain of interest and the desired level of simplification, these grid elements can be described in terms of various types of simple shapes, each with characteristic strengths and weaknesses. Classification and naming of these elements can vary by author, such as Reddy [34] who refers to some elements as *serendipity elements,* while Cook et al [32] simply uses the term *improved elements.* In this work, finite elements are classified by dimensionality, namely one, two, or three-dimensional; other advanced elements, such as plates and shells, are excluded from this discussion, but formulation details can be found in chapters 15 and 16 of [32] and 12 of [34]. Line (or bar) elements are used in one dimension; triangular and quadrilateral elements are used for two dimensions, and tetrahedrons and hexahedron elements in 3D. These types of 2D and 3D shapes can be represented as first or higher order elements, depending on the desired level of accuracy. Higher-order elements described the interpolation of the field quantity, such as displacements, by quadratic or higher-order polynomials. They can capture more accurately stress distributions in complex geometries,

but at the expense of greater required computational power. Examples of higher order elements are illustrated in the second row of figure 2.8, such as the 6-noded triangle or 20-noded hexahedron.

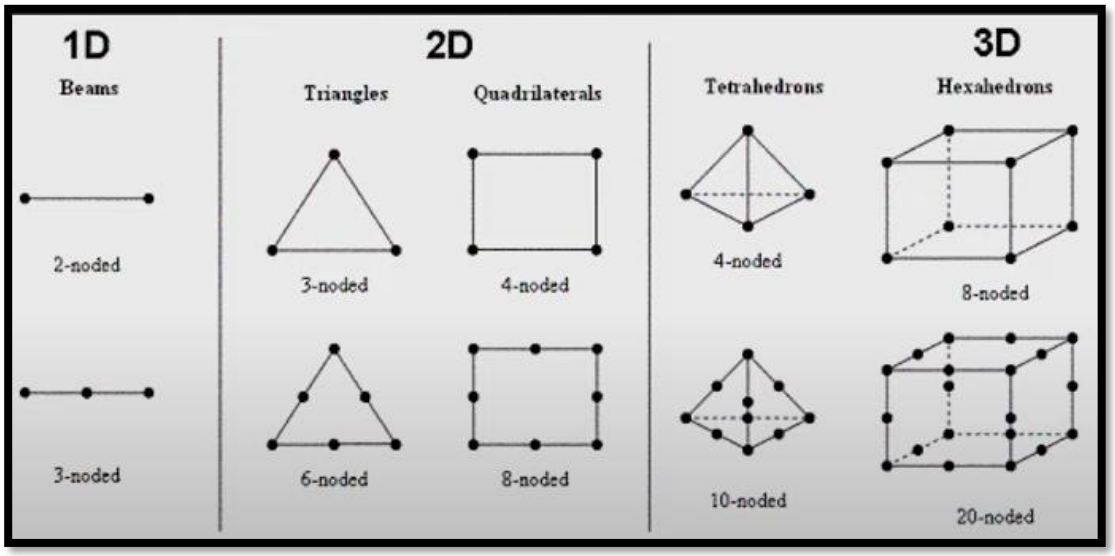

Figure 2.8 – Common types of 2D and 3D elements in FEA [33].

A. One-Dimensional Elements: Bar

BVPs where the axial dimension in the analyzed geometry is much larger than the lateral and thickness dimensions, such as a slender bar, can simplified to one-dimensional FEA. The bar element represents the simplest type of FEA, and, as a result, is the least computationally expensive element. The chief limitation associated with this element is the inability to generate displacements, strains, and stresses in the lateral and through-thickness directions. As the problem explored in section 2.2.1, the assembly of the global stiffness matrix can be achieved by appending the individual stiffness matrices of each nodal element. In the case of truss analysis, rotation matrices can be implemented to generate the global stiffness matrix in terms of the global coordinate system, and later solve for the displacements, stress, and strains.

B. Two-Dimensional Elements: Constant Strain (CST) and Linear Strain Triangle (LST)

Geometries where the axial and lateral directions must be considered to capture appropriately the studied physical phenomena require the use of two-dimensional elements. The linear triangle, illustrated in figure 2.9-a, is one of the basic elements used in 2D analysis. This element has three nodal elements, and its implementation produces a linear displacement variation of the investigated field quantity in the axial, u, and lateral, y, coordinates, as shown in 2.9-b. This is the reason why it is also referred to as the constant-strain triangle (CST). Because of its simplicity, it is typically used when high solution accuracy is not sought, and computational power is limited. Arguably, the main deficiency of this element is its inability to model deformation caused by bending. In the case of a beam loaded in bending only, such as in figure 2.10-a, the stress on each element along the x-axis, σ_x, displays a constant behavior rather than a linear variation that would be predicted by Euler-Bernoulli beam theory. Similarly, element 2, in 2.10-b displays a transverse shear strain that should not occur. As a result, this element tends to be very stiff when loading in bending conditions.

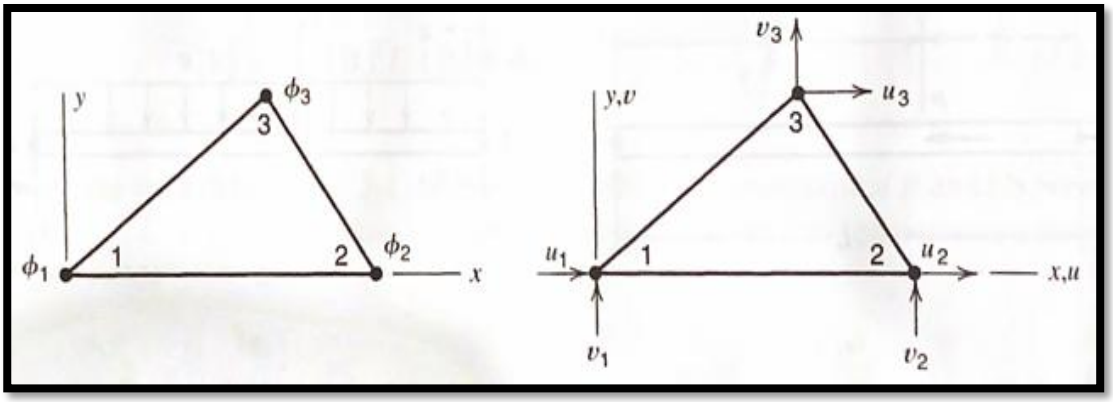

Figure 2.9 – (a) Linear Triangle Element (CST) and (b) Displacement field representation [32].

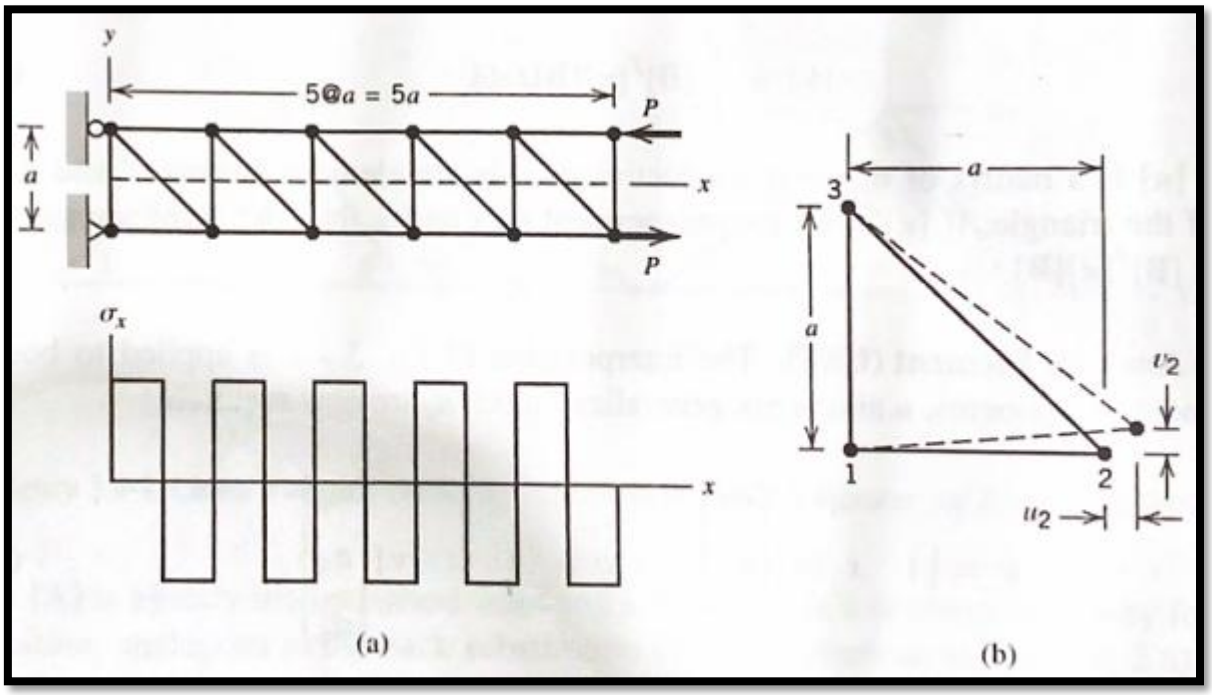

Figure 2.10 – a) Deformation of a beam modeled by CSTs along x-axis, loaded in bending and (b) Deformation of lower-left triangular element [32].

Moreover, the quadratic triangle has one additional node placed between each adjacent vertex, as shown in figure 2.11, each with two corresponding degrees of freedom. These additional nodes provide a better displacement prediction, relative to the CST, at the expense of more required computational power. This configuration yields a displacement field in terms of a complete second-order polynomial, as denoted by equations 2.23 and 2.24. In return, the computed strains can then vary linearly -reason why it is also called Linear-Strain Triangle. Despite being able to model strain variations linearly, the LST does not produce more accurate results -relative to beam theory- than the LST in some cases. For example, when modeling an isotropic cantilever beam under parabolic loading, Cook et al [32] found that increasing the number of CSTs yielded less

accurate results than the LST. Another associated limitation of the LST is that it yields a linear shear strain, γ_{xy}, rather than quadratic result in the y-direction.

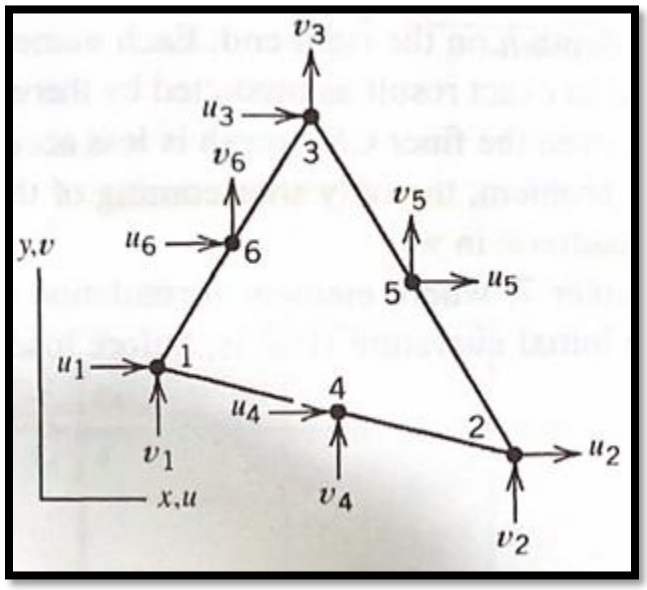

Figure 2.11 – Quadratic Triangle Element (LST) [32].

$$u_i = a_1 + a_2x + a_3y + a_4x^2 + a_5xy + a_6y^2 \quad (2.23)$$
$$v_i = a_7 + a_8x + a_9y + a_{10}x^2 + a_{11}xy + a_{12}y^2 \quad (2.24)$$

C. Two-Dimensional Elements: Bilinear (Q4) and Quadratic Rectangle (Q8, Q9)

The bilinear rectangle (Q4) has four nodal elements, as illustrated in figure 2.12. It is called "bilinear" because its displacement field is the product of two linear polynomials. Because of its simplicity, it is also used when computational resources are limited, and high accuracy is not required. Like the CST, one of its main deficiencies is its behavior in pure bending. A cantilever beam in bending, as shown in figure 2.13-a, modelled by Q4 elements exhibits *parasitic shear strain* γ_{xy}, which should be zero, but has a non-zero value. Two are the main implications of this phenomenon. First, the axial stress σ_x on the lower elements will be significantly different for the elements with constrained displacements (near the wall), as shown in figure 2.13-b. Second, the shear stress on the x-axis τ_{xy} shows a linear-like spurious variation, even though its value should be constant, as predicted by beam theory, as illustrated by figure 2.13-c.

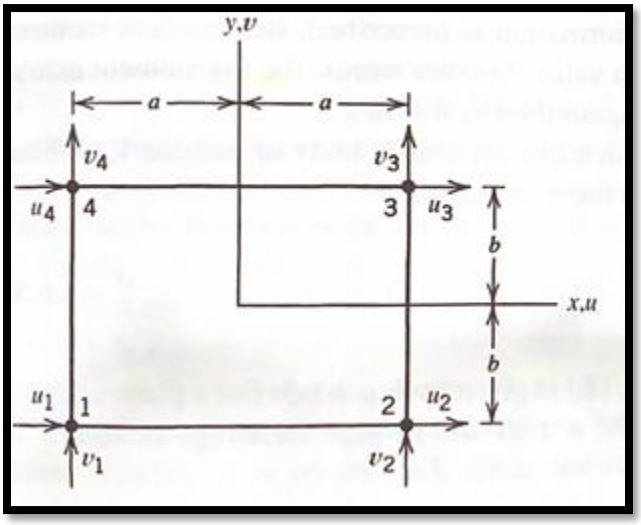

Figure 2.12 – Bilinear Quadrilateral Element (Q4) [32].

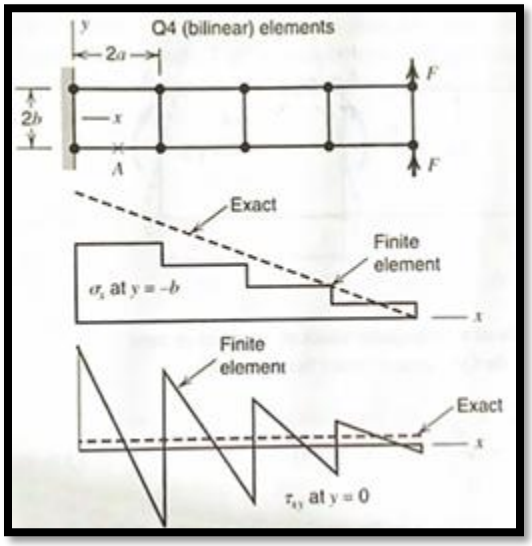

Figure 2.13 – Variations in axial stress and shear strain on a cantilever beam modeled by Q4 elements [32].

The quadratic rectangle, like the quadratic triangle element (LST), has one additional node between the original adjacent corners, as shown in figure 2.14. The 8 total nodal elements give this element its additional name, Q8. It is considered a higher-order element because its shape functions possess high-order polynomial terms which enable the better representation of displacements, strains, and stresses. Specifically, these displacements are captured by equations 2.25 and 2.26. The Q8 is the most robust element -compared to the CST, LST, and Q4- in capturing complex stress distributions and curved geometry. As a result, it is used when a higher degree of accuracy

is desired and computational power is not limited. The quadratic rectangle does not display the parasitic shear strain issue experienced by the bilinear quadrilateral element, Q4. As a result, the Q8 is typically used in applications where bending must be captured accurately.

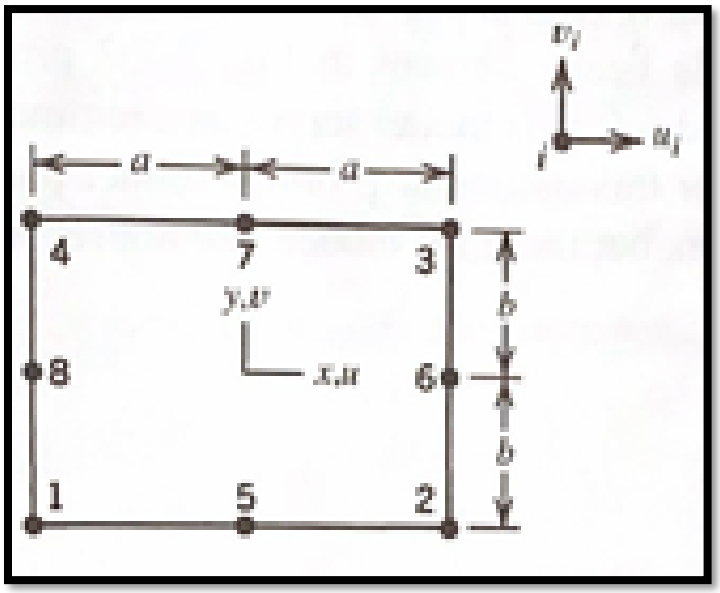

Figure 2.14 – Quadratic Rectangular Element.

$$u_i = a_1 + a_2x + a_3y + a_4x^2 + a_5xy + a_6y^2 + a_7x^2y + a_8xy^2 \quad (2.25)$$
$$v_i = a_9 + a_{10}x + a_{11}y + a_{12}x^2 + a_{13}xy + a_{14}y^2 + a_{15}x^2y + a_{16}xy^2 \quad (2.26)$$

D. Three-Dimensional Elements: T4 and T10 Tetrahedra

BVPs where interactions between width, length, and thickness must be considered altogether require the use of three-dimensional elements. One of the simplest 3D elements is the four-node tetrahedron (T4), which is illustrated in figure 2.15. These elements are typically used to discretize complex geometries, such as those asymmetrical and with high curvature. Like the CST in two-dimensional analysis, the T4 is susceptible to shear-locking behavior. Nevertheless, this issue can be overcome by implementing higher-order elements, such as the ten-nodded tetrahedron (T10), illustrated in figure 2.16. Both the T4 and T10 have shape functions represented in terms of "natural" reference coordinates, which Cook et al [32], for example, names *r, s,* and *t.* The implementation of this reference coordinate system allows the element to maintain their position with respect to itself and become independent of its orientation in the global coordinate system. The shape functions of the T4 are expressed in equation 2.27, whereas the shape functions of the T10 are expressed in 2.27. The T10 can capture better higher stress gradients and avoid shear locking behavior, but this is penalized by a higher required computational power.

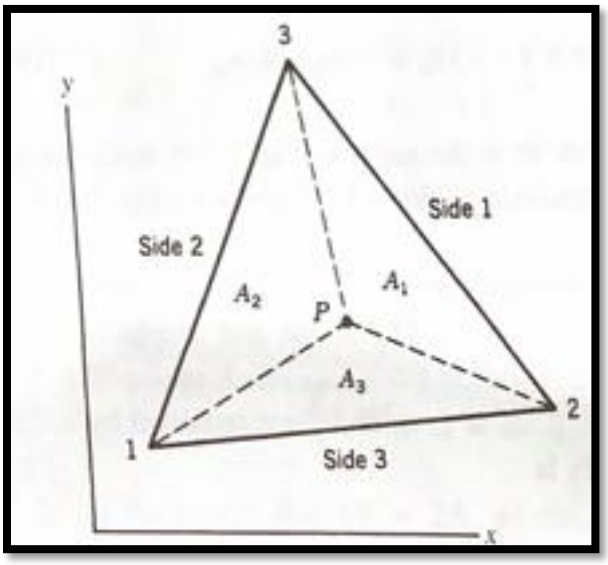

Figure 2.15 – Linear Tetrahedron Element.

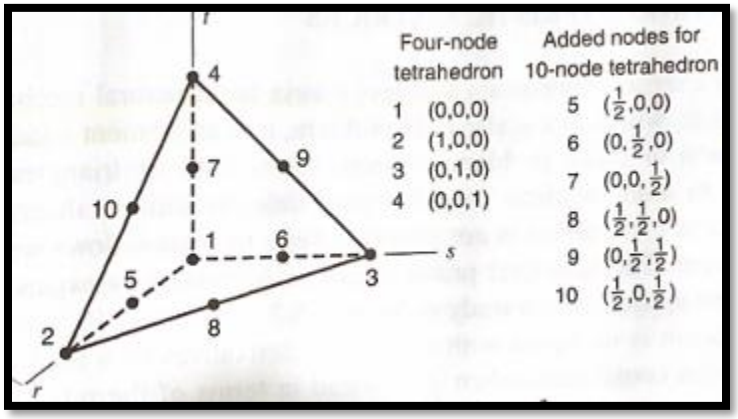

Figure 2.16 – Quadratic Tetrahedron Element.

$$\mathrm{N}_1 = 1 - r - s - t \qquad N_2 = r \qquad \mathrm{N}_3 = s \qquad \mathrm{N}_4 = t \tag{2.26}$$

$$\begin{aligned} &\mathrm{N}_1 = (1 - r - s - t)(1 - 2r - 2s - 2t) \\ &N_2 = r(2r - 1) \qquad \mathrm{N}_5 = 4r(1 - r - s - t) \qquad N_8 = 4rs \\ &N_3 = s(2s - 1) \qquad \mathrm{N}_6 = 4s(1 - r - s - t) \qquad N_9 = 4st \\ &N_4 = t(2t - 1) \qquad \mathrm{N}_7 = 4t(1 - r - s - t) \qquad N_{10} = 4rt \end{aligned} \tag{2.27}$$

E. Three-Dimensional Elements: H8 and H20 Rectangular Solid Elements

The second simplest 3D element is the eight-nodded trilinear element (H8), illustrated in figure 2.17. It receives this name because each of its shape functions is the product of three linear polynomial functions that have the form of equation 2.28. The H8 is typically used in relatively simply geometries, such as straight, symmetric shapes with no curvature. Like the T4, this element is susceptible to shear-locking behavior, but this issue can also be avoided by implementing a higher-order element, such as the twenty-node solid element (H20), depicted in figure 2.18. In addition, the H20 element can capture more accurately high stress gradients at the expense of greater computational power. Its shape functions are quartic. Both the H8 and H20 can be developed through isoparametric formulation, which is discussed in extensive detail in chapter 6 of Cook et al [32].

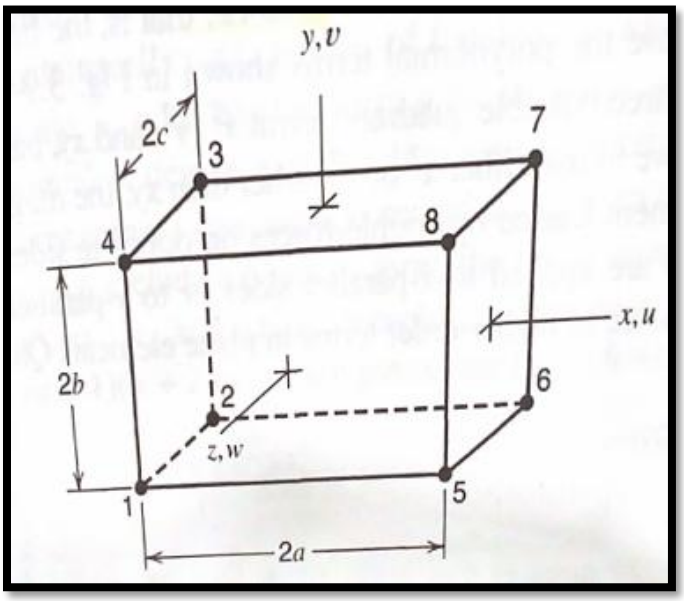

Figure 2.17 – Eight-nodded Trilinear Element.

$$N_i = \frac{(a \pm x)(b \pm y)(c \pm z)}{8abc} \qquad (2.28)$$

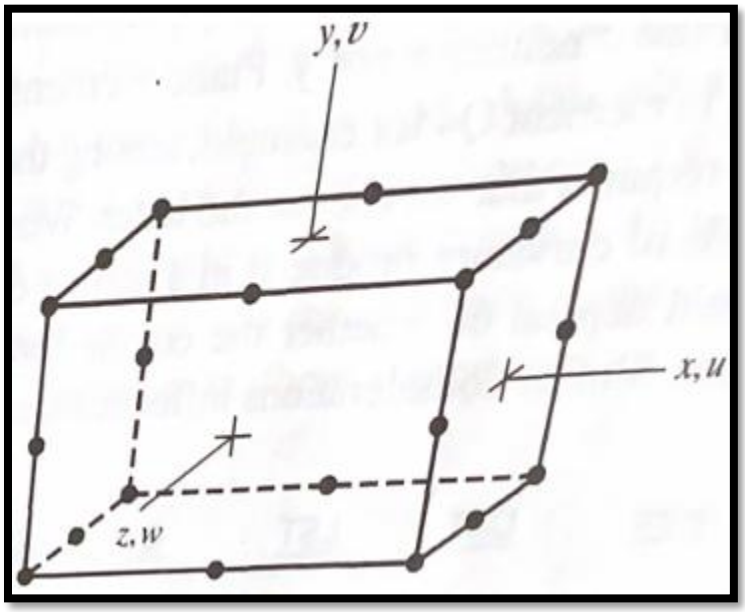

Figure 2.18 – Twenty-node Solid Element.

2.2.3 Constraints and Boundary Conditions

After the analyzed geometry has been discretized through 1D, 2D, or 3D elements, boundary conditions need to be imposed, as previously demonstrated in section 2.2.1. The purpose of this implementation is to represent mathematically support areas and forces applied to the studied BVP. Most BCs can be categorized as i) displacement constraints or ii) traction and force constraints. Displacement constraints assign a zero-value to the degrees of freedom of the selected nodal locations. In the case of a pinned beam, for example, the horizontal and vertical displacements, u and w, would be constraint to have a 0 value, and the moment would need to be specified. In contrast, in the case of a vertical roller, only the horizontal displacement would correspond to 0, and the transverse force and moment would need to be known. Commercial FEA software handles the implementation of displacement constraints by modifying the displacement in the assembled global stiffness matrix, whereas traction and force constraints are enforced by modifying the loading vector. Additional supports and its corresponding displacement and force BCs are shown in table 2.2.

Table 2.2 - Commonly used support conditions for beams and frames [34].

Type of support	Displacement boundary conditions	Force boundary conditions
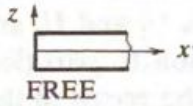 FREE	None	All, as specified
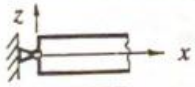 PINNED	$u = 0$ $w = 0$	Moment is specified
 ROLLER (vertical)	$u = 0$	Transverse force and moment are specified
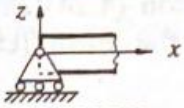 ROLLER (horizontal)	$w = 0$	Horizontal force and bending moment are specified
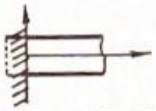 FIXED or CLAMPED	$u = 0$ $w = 0$ $dw/dx = 0$	None specified

2.2.4 Computational Approach

As a simplification, four main milestones can be outlined in this process: 1) learning about the problem, 2) developing a mathematical model, 3) modeling and simulating it, and 4) revising the results. Cook et al [32] proposed following the general methodology summarized in Table 2.3.

Table 2.3 - General methodology to solve a problem by FEA.

Stage	Description
Problem Revision	Research and prepare an appropriate model describing the physics of the system of interest according to the desired level of accuracy.
Development of Mathematical Model	Determine appropriate simplifications and create a mathematical model. Obtain approximate results from analytical calculations, handbook formulas, verified previous solutions, or experiments.
Modeling and Simulation	Generate input data describing the geometry, material properties, loads, and boundary conditions. Determine an appropriate mesh size and density, and potential areas of refinement. Specify quantities of interest to display, such as deformed shapes and stresses.
Revision of Results	Examine qualitatively whether the results seem logical. Perform adjustments to the physics model and domain discretization to obtain a satisfactory solution.

2.3 Composite Material Modeling in Ansys

In addition to enabling the implementation of the FEM, Ansys, the commercial software selected for this study, counts with the capability of analyzing composite structures. As explored in section 1.3, the main inherent challenges involved with these types of structures are the anisotropic mechanical properties, manufacturing defects, and the mechanical behavior of the individual constituents (fiber and matrix). Ansys deals with these challenges by offering a set of "composite modeling features" which aid the user in creating an accurate digital representation of the analyzed composite structure. One of these features is *ACP Pre*, whose graphic user interface (GUI) and model tree are shown in figure 2.20. As the name implies, the term "layup" refers to the collection of piles that make up the composite lamina. The material, thickness, and orientation need to be specified for each individual ply. By convention, the first ply entry is treated as the *bottom ply*, but the individual ply orientation can be customized in different manners, such as in terms of a global coordinate system, or simply top-down. The "individual" material properties of the fibers and matrix are defined on the conventional material library of Ansys, whereas the thickness and ply orientation are defined in the ACP Pre suit. For visualization, this menu is included in figure 2.21, located below.

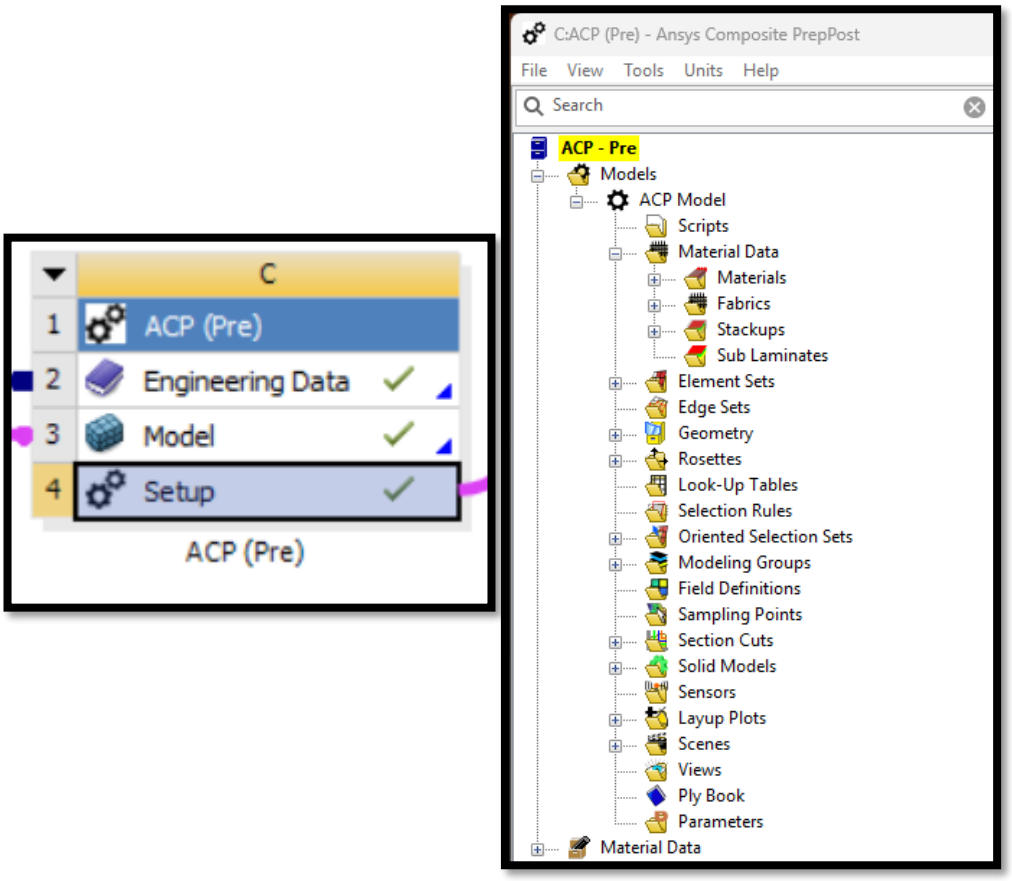

Figure 2.20. – Ansys ACP Feature and model tree [35].

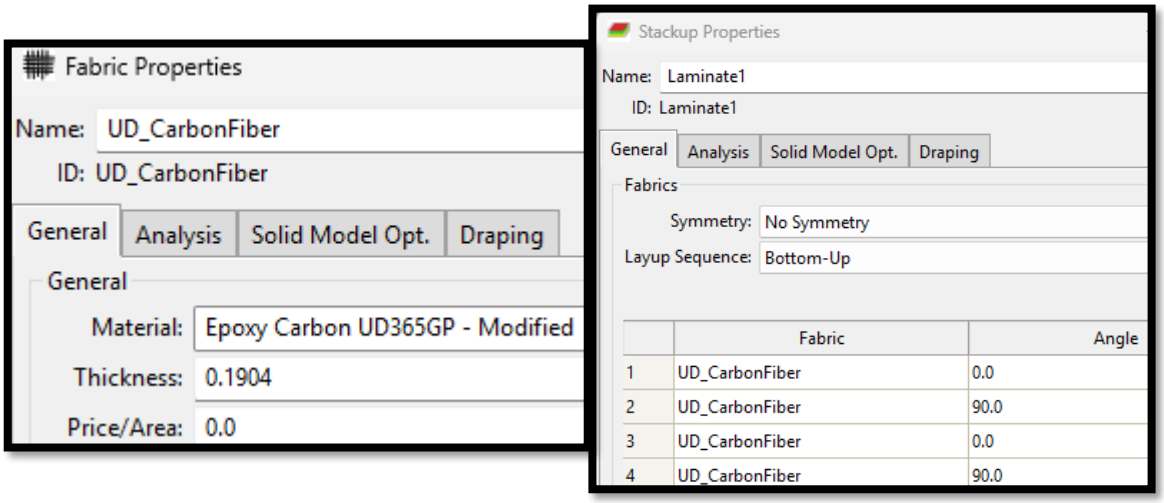

Figure 2.21 – Ansys fabric and stack up properties GUI [35].

Ansys's ACP Pre provides different methods of modeling composite layups. First is the conventional shell composite layup. This can be understood as a two-dimensional model intended for thin-walled structures, where the thickness direction is much smaller than other dimensions. This assumption implies that in-plane and interlaminar stresses are not significant. These conventional shell elements are then used to discretize the reference surface of each ply; displacement and rotational degrees of freedom are allowed. In contrast, the solid- shell composite layup provides a three-dimensional representation for thicker structures, where in-plane and interlaminar stress interactions must be considered. This model considers double-sided contact across the individual plies to better capture interlaminar interactions, such as delamination and bucking, in the composite layup. Only displacements can be captured with this type of element. A visual distinction between conventional and continuum shell composite layups is illustrated by figure 2.22. The third method is the solid composite layup, which is the most robust and detailed element to model each laminate in the composite structure. Ansys's user's manual recommends to use this element when the interlaminar stresses must be captured accurately, such as in thick structures. This type of element is the most computationally expensive, followed by the solid-shell composite layup.

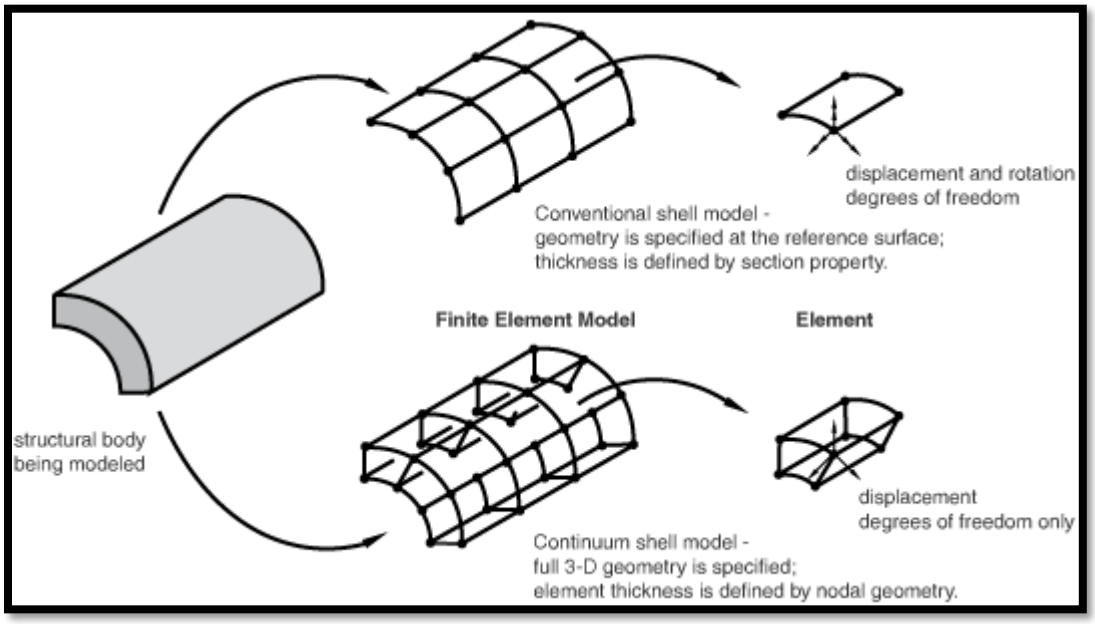

Figure 2.22 –Representation of conventional and continuum shell models in Ansys [35].

2.4 Nonlinear Structural Analysis in Ansys

When a load is applied on a conventional structure, it first experiences elastic deformation, where the displacements of the elements composing the material are very small. As a result, it can be assumed that the material properties and boundary conditions remain constant under loading. When this occurs, Ansys formulates the global stiffness matrix and then implements iterative solves to find the field variable, displacements, and secondary outputs, strains and stresses. Nevertheless, when the material surpasses the elastic deformation zone and experiences significant

deformations, non-linear problem behavior is expected. In structural mechanics problems, Cook et al [32] identified three main types of nonlinear behavior. First is material non-linearity, which occurs when the material properties depend on the stress and strain, such as during plasticity and creep. Second is contact nonlinearity, where a gap is formed between adjacent parts, creating thus sliding of frictional forces. Lastly is geometric nonlinearity, where once deformation is large enough, the equilibrium equations must be modified to conform with the newly deformed structure.

Ansys deals with these challenges by implementing a series of solution methods and convergence monitoring algorithms. Ansys's Mechanical user's manual [35], for example, states that solving nonlinear problems implies the following:

- A combination of incremental and iterative procedures
- Using the Newton-Raphson method
- Determining convergence
- Defining loads as a function of time
- Selecting Suitable time increments automatically

In more detail, when solving for a nonlinear displacement curve, such as that illustrated by figure 2.23, Ansys breaks the simulation in smaller time increments and finds the approximate equilibrium configuration. In more detail, when the structure is in equilibrium, the sum of internal and external forces, I, and P, respectively must be 0, as expressed by equation 2.29. Once the structure begins to show non-linear behavior, Ansys uses the structure's tangent stiffness, K_0, to determine the displacement correction c_a. This method is based on the elastic-limit configuration u_0, where upon the application of a small load increment, ΔP, the resulting displacement is updated to u_a,as illustrated by figure 2.24. During this initial iteration, Ansys calculates the updated structure's internal forces, I_a, and assigns the difference between the applied load and I_a to R_a, the force residual for the corresponding iteration. The default tolerance for this value is 0.5% but can be adjusted. If R_a is smaller than the specified tolerance, the displacement is assumed to be in equilibrium. Otherwise, an additional iteration is performed by determining a different correction, c_b, as illustrated in figure 2.25. In addition to these iterative solution methods, Ansys also provides additional methods to troubleshoot and aid in convergence, such as performing non-linear diaglostics, tracking convergence graphicallty, and non-linear stabilization, as outlined in section 8.12 of the user's manual [35].

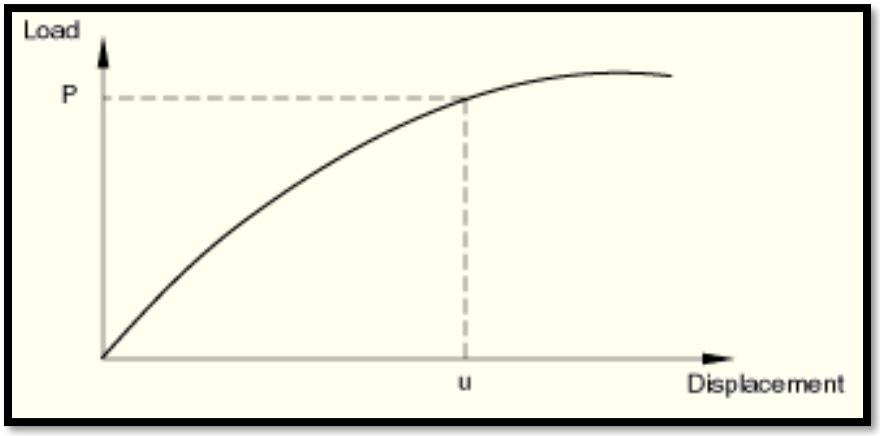

Figure 2.23 – Nonlinear Displacement Curve [36].

$$P + I = 0 \tag{2.29}$$

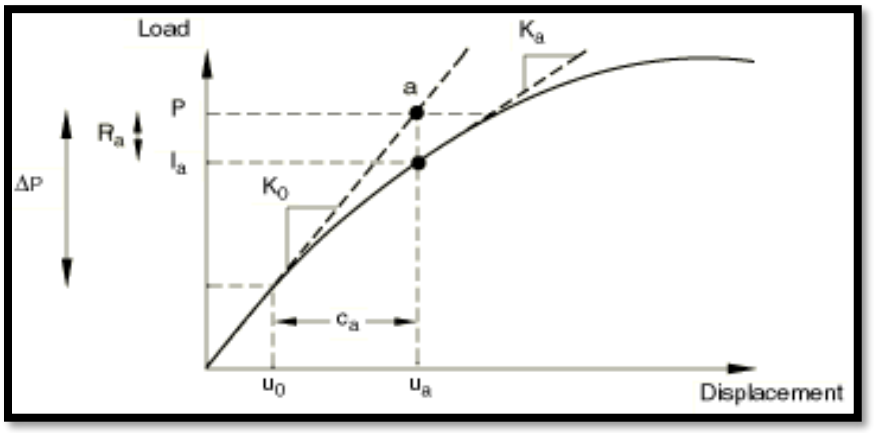

Figure 2.24 – First iteration of the nonlinear stress analysis solver method [36].

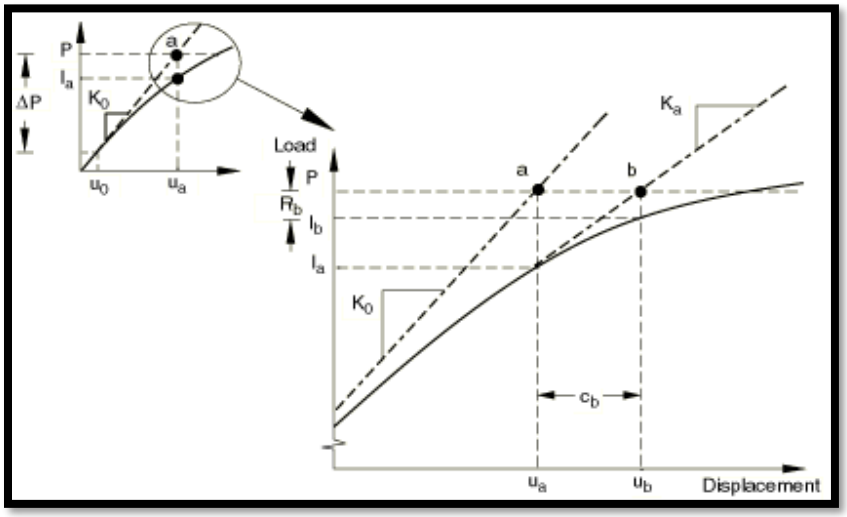

Figure 2.25 – Second iteration of the nonlinear stress analysis solver method [36].

3. Geometry Model of the Titan Submersible

3.1 General Methodology

To conduct the proposed structural analysis of the Titan submersible, the geometry model, material assignment, and material properties were first prepared. Unsurprisingly, the nature of reverse-engineering an invention requires that the investigator consults all available resources and uses sound engineering judgement in certain areas to generate the most reasonable approximation to the actual product design. While the dimensions and material assignments of some structural components were available at the time this report was prepared, others had to be estimated. These main sources and assumptions are discussed in greater detail in each of the subsections under section 3.2, titled *Main Components*. The general process followed to develop the geometry model of the Titan Submersible is shown in figure 3.1. This process started with the gathering of *intelligence*, which in this context refers to descriptive pictures, visualizations, dimensions, and material assignments of each of the main components of the Titan Submersible. Consequently, this information was categorized and compared. Logical tests were then performed; some of these example questions can be found in table 3.1, located below. Conducting each of these tests encouraged the consistent and active evaluation of the obtained dimensions and material selections. Once these characteristics were deemed satisfactory, each major component was developed and subsequently assembled in SolidWorks ®, as explained in the following section.

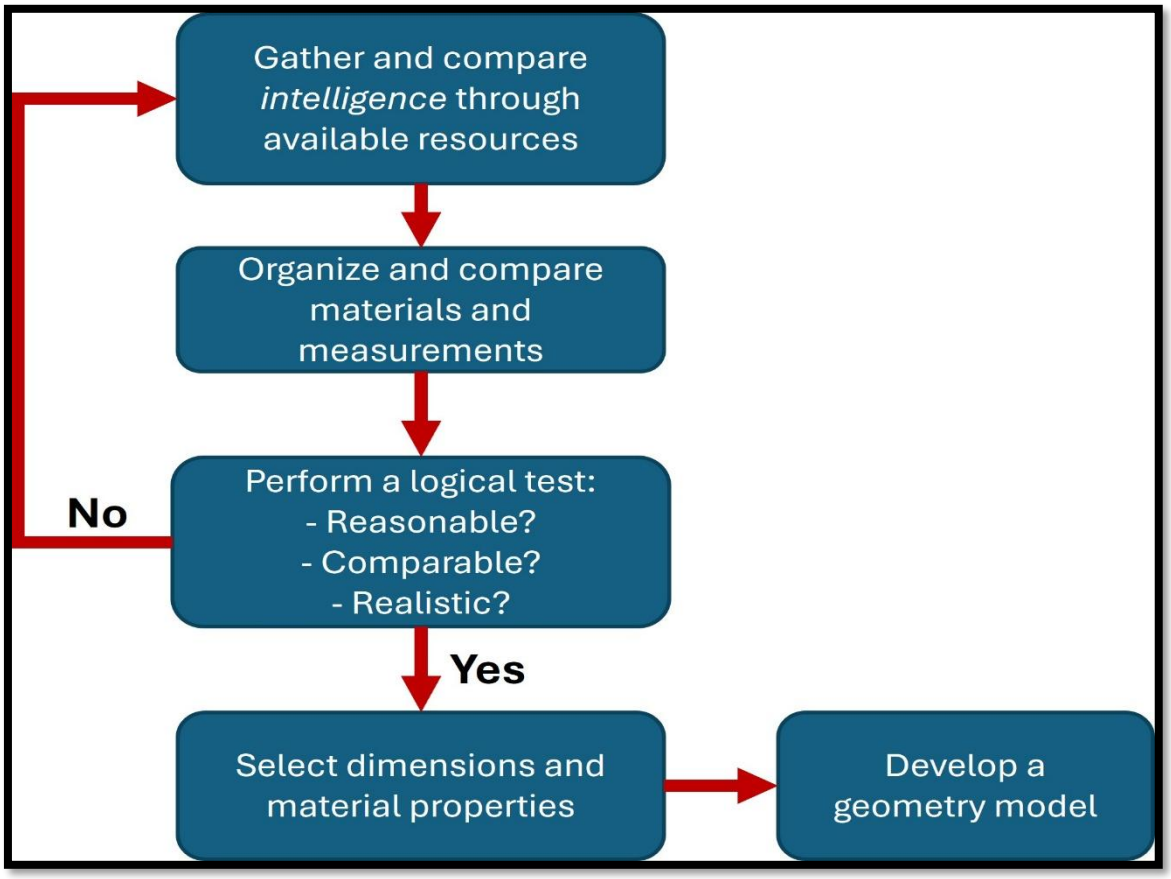

Figure 3.1 – General methodology followed to develop the geometry model of the Titan Submersible.

Table 3.1 - Examples of logical tests performed on the gathered information.

Logical Test	Example Question
Reasonable	Is it reasonable that the flange thickness of an O-Ring be 1.0m? Is it reasonable for an observation window diameter to be 5cm?
Comparable	The cylindrical pressure hull is reported by resource A to have a wall thickness of 5.0 and 5.1inches respectively, whereas resource C reports 100inches. Does resource C provide a reasonably comparable dimension?
Realistic	Visually, the thickness of a component is suspected to be identical to the width of a thumb. Resource D reports this thickness to be 1mm. Is this realistic, knowing that the width of a thumb is roughly 22mm?

3.2 Main Components

A general description and visualization of the Titan submersible was first presented in section 1.2, but, for readability, more detailed pictures of the vehicle are reintroduced below. Figure 3.2 shows an isometric view of the submersible outside the water. Figure 3.3 was presented by Stockton Rush at a conference in 2022 [37], during which he described the main structural components of the submersible. The right image in figure 3.3 is further adapted to identify and label these main structural components, as shown in figure 3.4. Because these components were the *main line of defense* protecting the passengers in the submersible, the author proposes to conduct the structural analysis by focusing on these components only. In short, the carbon-fiber cylindrical hull is flanked by two spherical sections, which are connected to the main cylinder through two interface *O-Rings*. For convenience, these main components are bulletized after paragraph. Although conventional reading direction suggests that the first discussed component be the observation window, followed by the bow, spherical section, the author chooses to introduce the components by *logical assembly order*. In other words, these components will be developed in the most intuitive way, starting with the simplest. Corresponding dimensions and computer-aided drawing development are discussed in detail in the proceeding sections.

- Cylindrical Pressure Hull
- Interface O-Rings
- Stern, Spherical Section
- Bow, Spherical Section
- Observation Window

Figure 3.2 – Isometric view of the Titan Submersible [7].

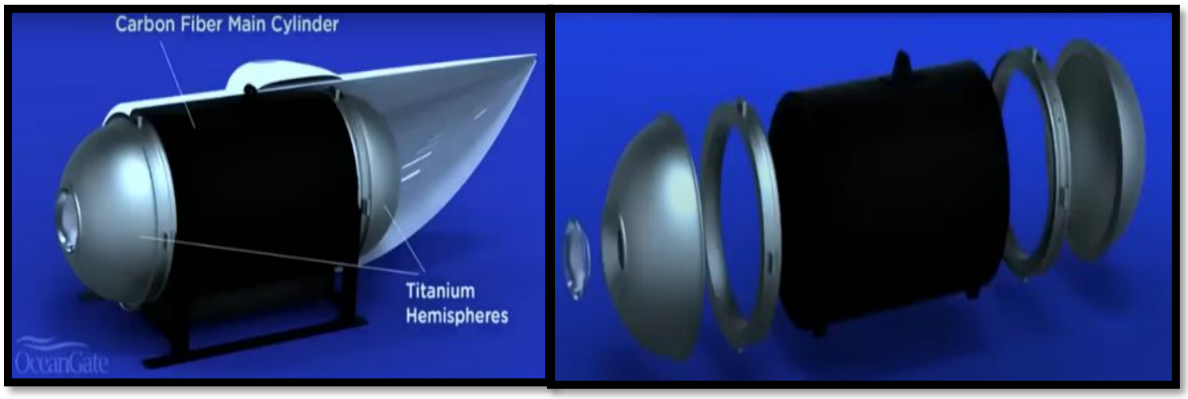

Figure 3.3 – Schematic of the Titan Submersible and main structural components [37].

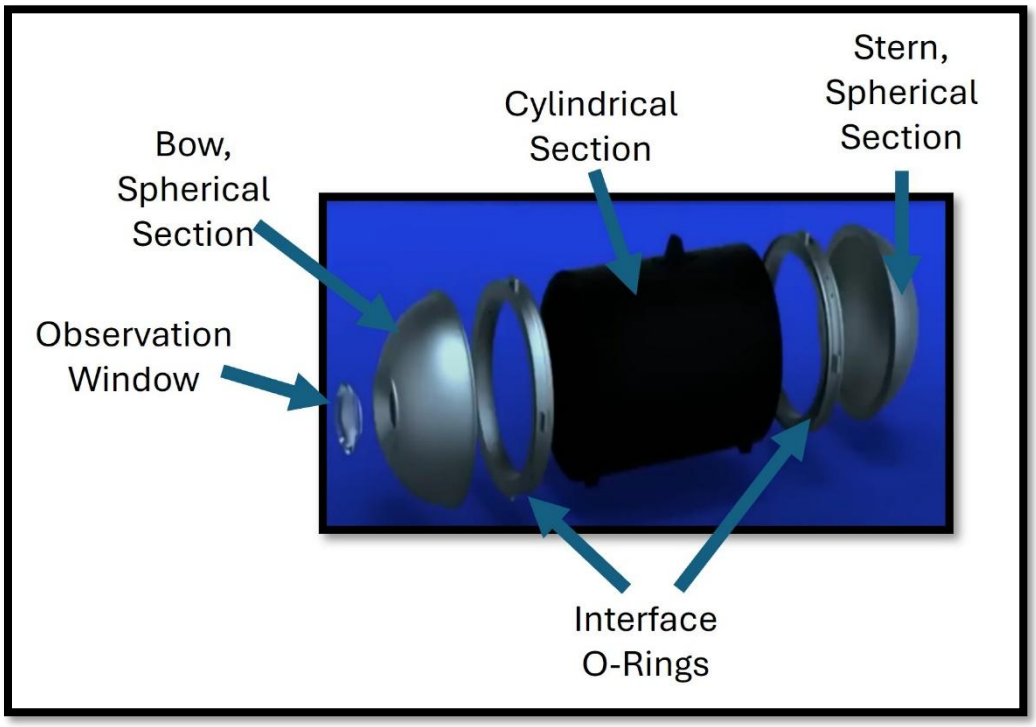

Figure 3.4 – Adaptation of main structural components of the Titan Submersible.

3.2.1 Cylindrical Pressure Hull

The cylindrical pressure hull of the submersible could be described as the *middle section* of the structure, as signaled in figure 3.5. During normal operations, it was analogous to the fuselage section of a passenger aircraft, where the passengers were seated. The most valuable real-life picture -found at the time this report was written- was shown by Stockton Rush in his 2022 business presentation [37] and is labeled as figure 3.6. It shows the cylindrical pressure hull, as workers apply an adhesive paste to the top surface, which is connected to the interface O-ring. This component is characterized by three main dimensions: inner diameter, length, and thickness. In Wikipedia [7] and a Seattle Times article [8], these values were reflected as 5.5ft, 8.3ft, and 5.0in, respectively. Converting these values to metric units, as equations 3.30 to 3.32 show, leads to the numbers summarized in table 3.2.

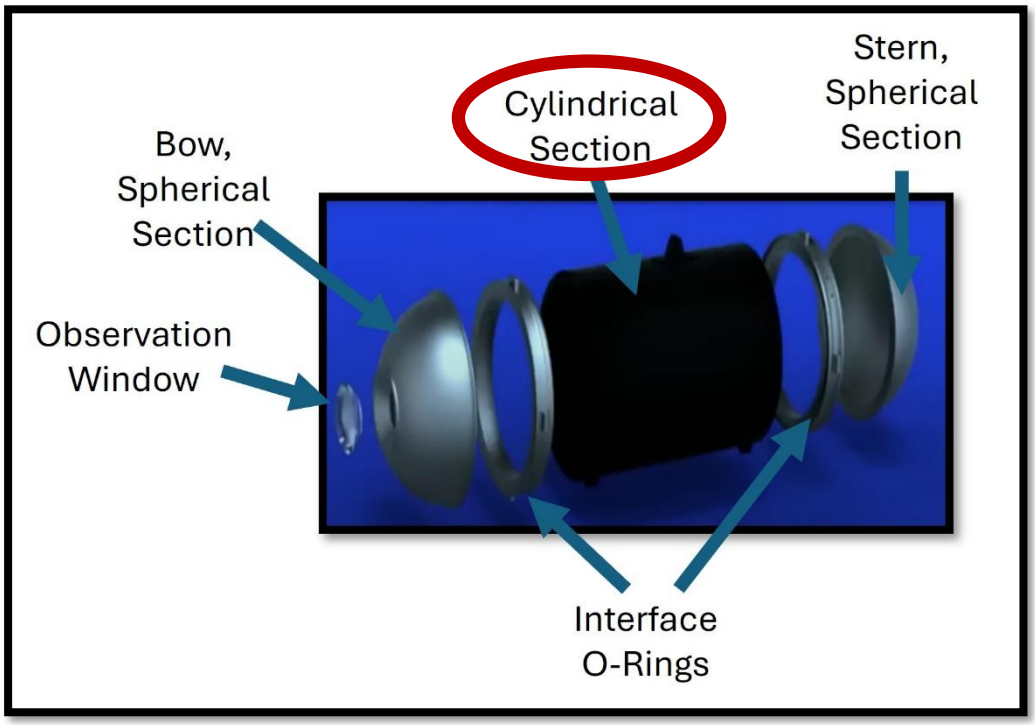

Figure 3.5 – Cylindrical section and additional components of the Titan Submersible.

Figure 3.6 – Cylindrical pressure hull used in first design iteration of the Titan Submersible [37].

Table 3.2 - Cylindrical pressure hull dimensions and information source.

Component Name	Dimension		Source
Cylindrical Section	Inner Diameter [m]	1.4022	Seattle Times [8]
	Length [m]	2.5298	Wikipedia [7]
	Thickness [cm]	12.70	Wikipedia [7]

$$4.6\text{ft} * \left(\frac{30.48\text{m}}{1\text{ft}}\right) = 140.21\text{cm} \quad (3.1)$$

$$8.3\text{ft} * \left(\frac{30.48\text{cm}}{1\text{ft}}\right) = 252.98\text{cm} \quad (3.2)$$

$$5.0\text{in} * \left(\frac{2.54\text{cm}}{1\text{in}}\right) = 12.7\text{cm} \quad (3.3)$$

Once these values were compiled, a two-dimensional sketch model was developed in SolidWorks ®, as shown in figure 3.7. The grey cross-sectional area enclosed by the black lines was then revolved 360 degrees about the x-axis, which enabled the creation of the three-dimensional pressure hull. Starting from the top left corner, and proceeding clockwise, figure 3.8 shows the isometric, top, and front views, respectively, of this component.

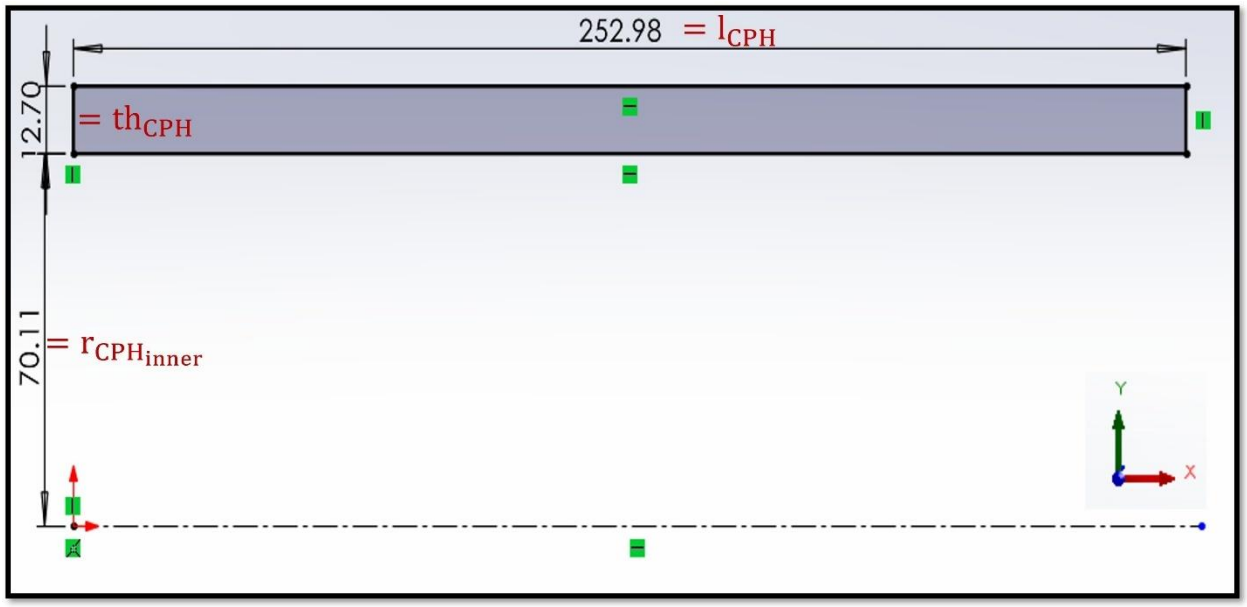

Figure 3.7 – Two-dimensional sketch model of the cylindrical pressure hull.

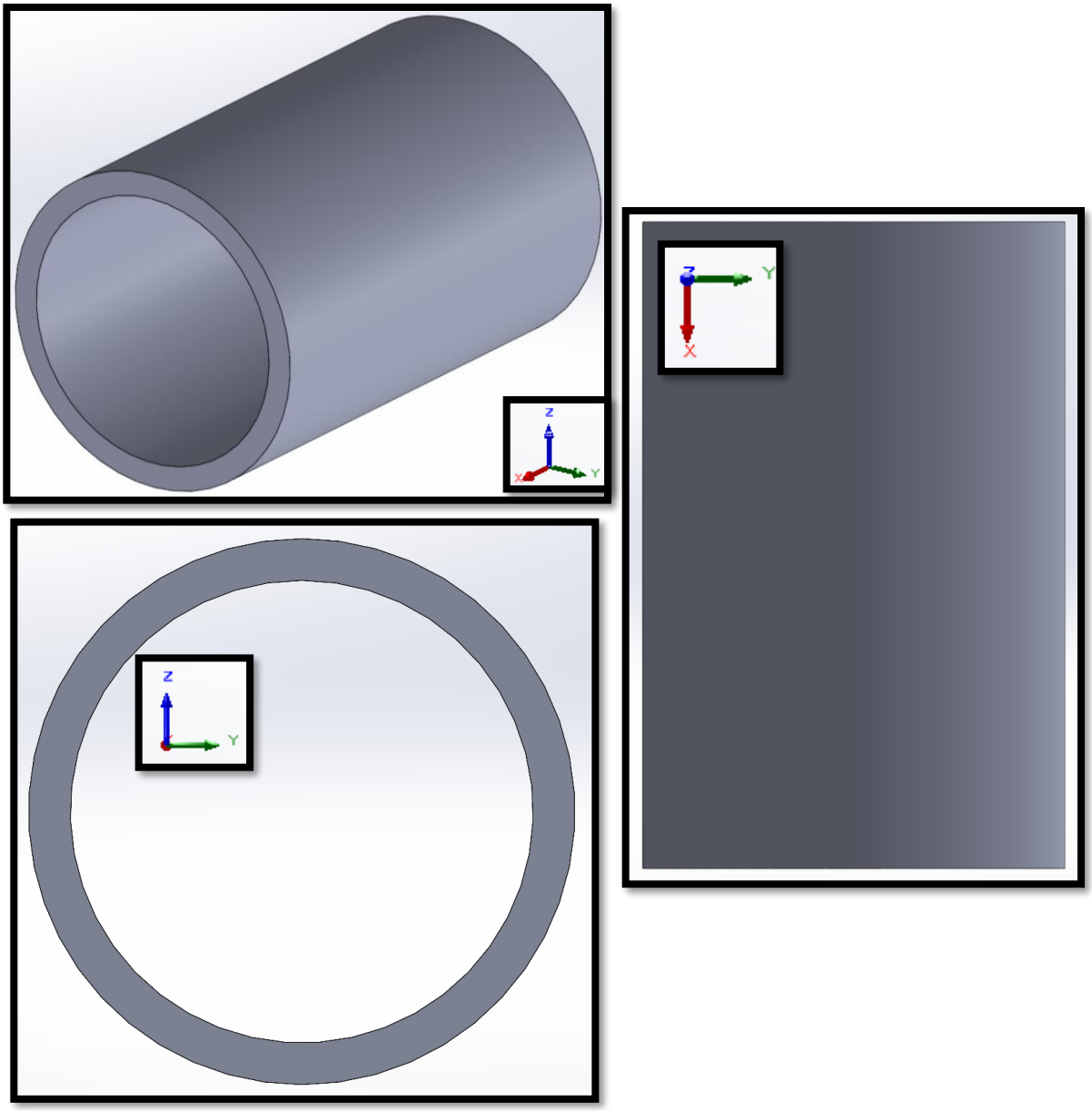

Figure 3.8 – Isometric, top, and front view of the cylindrical pressure hull component in SolidWorks ®.

3.2.2 Interface O-Rings

As the name implies, the Interface O-Rings are the connecting bodies between the CFRE cylindrical pressure hull and the Titanium spherical sections, as shown in figure 3.9. The purpose of these rings was to create a seal between its two flanking components and prevent fluid leakage, such as air outside or water inside the submersible. The most insightful available visualizations of this component are compiled in figure 3.10. The top left image shows the surface connecting to the spherical section, while the top right shows the surface joining the cylindrical section. The bottom right image provides additional details about the cross-section mating with the CFRE hull,

and the bottom left provides the outer profile of the O-Ring. Four valuable details that can be observed from this image are bulletized below. These observations are annotated in figure 3.11 for clarification.

- The side meeting the spherical section is flat and slightly protruded in the radial direction, away from the central axis.
- The side joining the CFRE cylindrical pressure hull is not flat but C-shaped. The lower half of this C section holds the inner diameter edge of the pressure hull surface, while the upper half holds the outer diameter surface.
- The lower C section appears to be uniformly extended to the opposite end, which meets the spherical section. Both protrude in the axial direction, pointing toward the cylindrical section.
- The middle section is of uniform shape and smaller than connecting end.

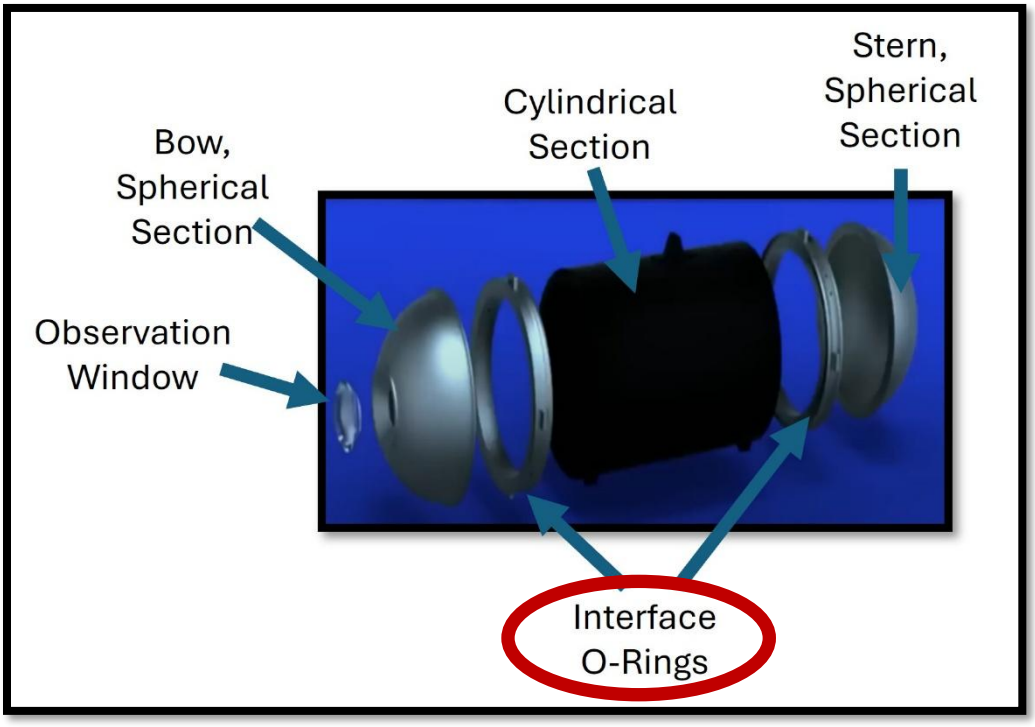

Figure 3.9 – Interface O-Rings and additional components of the Titan Submersible.

Figure 3.10 – Most valuable visualizations of the Interface O-Rings [37].

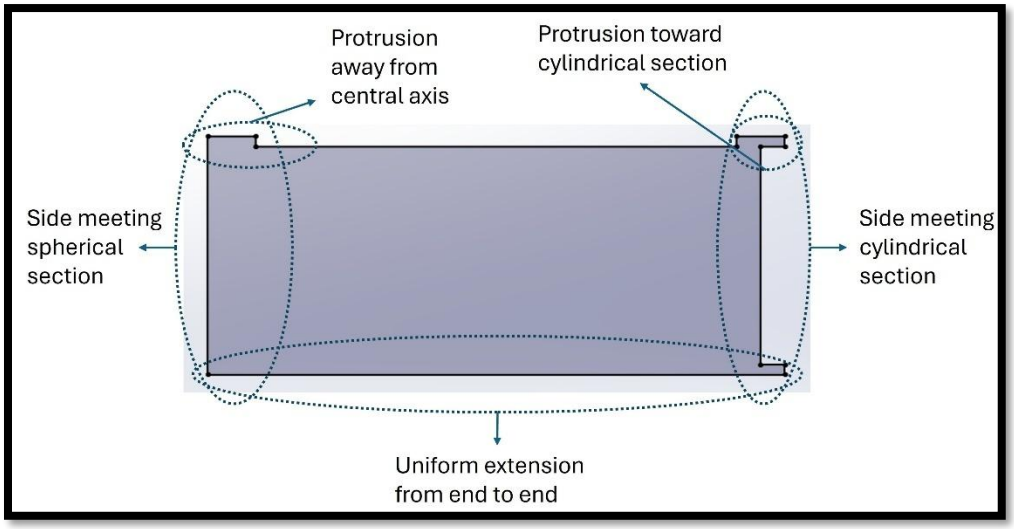

Figure 3.11 – Qualitative Cross-sectional profile of the O-Ring.

Because no available resources provided information about the measurements of this component, digital scaling and engineering judgement were used to determine the most reasonable component dimensions. A male, adult human thumb can be observed in the amplified bottom right image in figure 3.10, labeled now figure 3.12. The average thumb width, Tb, measured at the

knuckle (see bottom right corner of 3.11) was reported as 22mm by a ring-maker website [41]. Figure 3.12 was a frame obtained from a video [40] and is the closest approximation to a near-perpendicular camera angle. As a result, figure 3.12 is assumed to be an ideal, scalable representation of the real O-Ring component. Using digital scaling, the magnitude of the arrow placed over the thumb was rotated and scaled to match the dimensions illustrated in the upper and lower images of figure 3.12. These dimensions were then compiled and recorded in table 3.3.

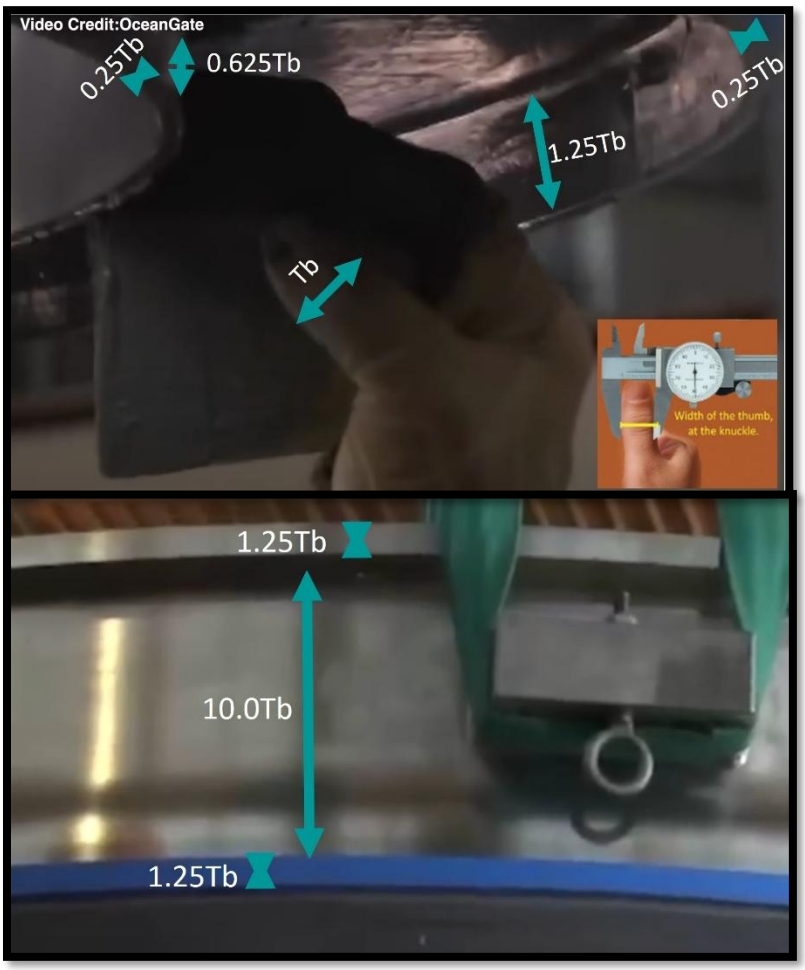

Figure 3.12 – Digital scaling of the O-Ring dimensions.

Table 3.3 - Titanium O-Ring interface dimensions and information source.

Component Name	Dimension		Source
O-Ring Interface	Inner Diameter, C-Section [m]	1.4022	Wikipedia [7]
	Outer Diameter, C-Section [m]	1.6562	Wikipedia [7]
	Thickness, C-Section [cm]	0.60	Engineering Judgement
	Width, C-Section [cm]	1.40	Engineering Judgement
	Web Thickness, C-Section [cm]	2.80	Engineering Judgement
	Length, O-Ring Mid-Section [cm]	28.00	Engineering Judgement
	Thickness, Spherical Section Interface [cm]	2.80	Engineering Judgement

Using the previous dimensions as the most reasonable estimates, the two-dimensional sketch depicted in figure 3.13 was then developed. For clarity, figure 3.13-a shows only two dimensions, the radial inner and outer distances from the origin, r_{inn} and r_{out}. The space between these two dimensions encloses the cylindrical pressure hull thickness. Figure 3.13-b includes the remaining measurements: thickness of spherical section interface th_{SSI}, length of the O-Ring middle section l_{mid}, web thickness of the C-section $t_{web_{CSec}}$, width of the C-section w_{CSec}, and thickness of the C-section t_{CSec}. To create the three-dimensional O-ring, the gray, enclosed area was revolved 360 degrees about the x-axis. Starting from the top left, and moving clockwise, the isometric, front, and top views are compiled in figure 3.14.

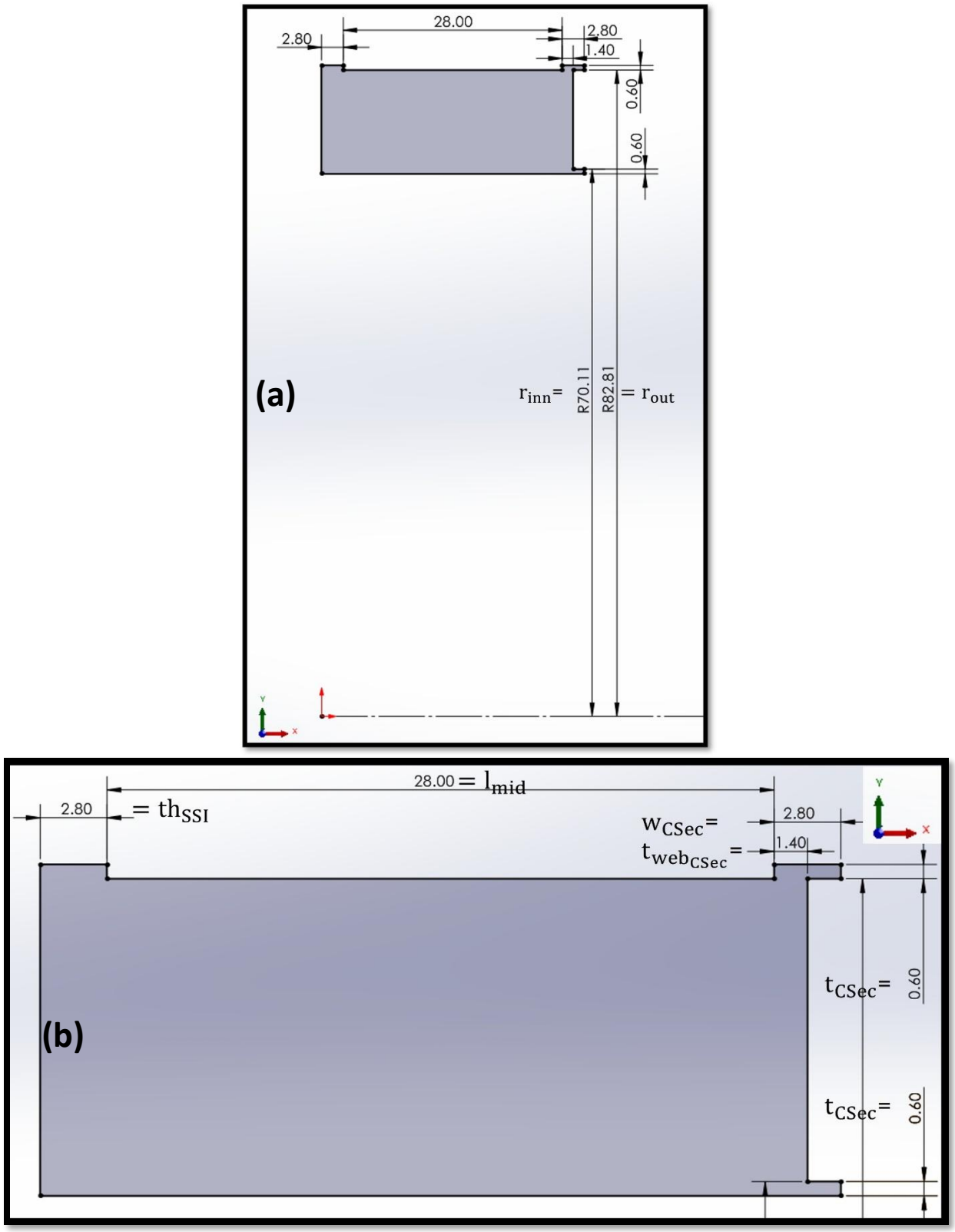

Figure 3.13 - Two-dimensional sketch model of the Titanium Interface O-Ring.

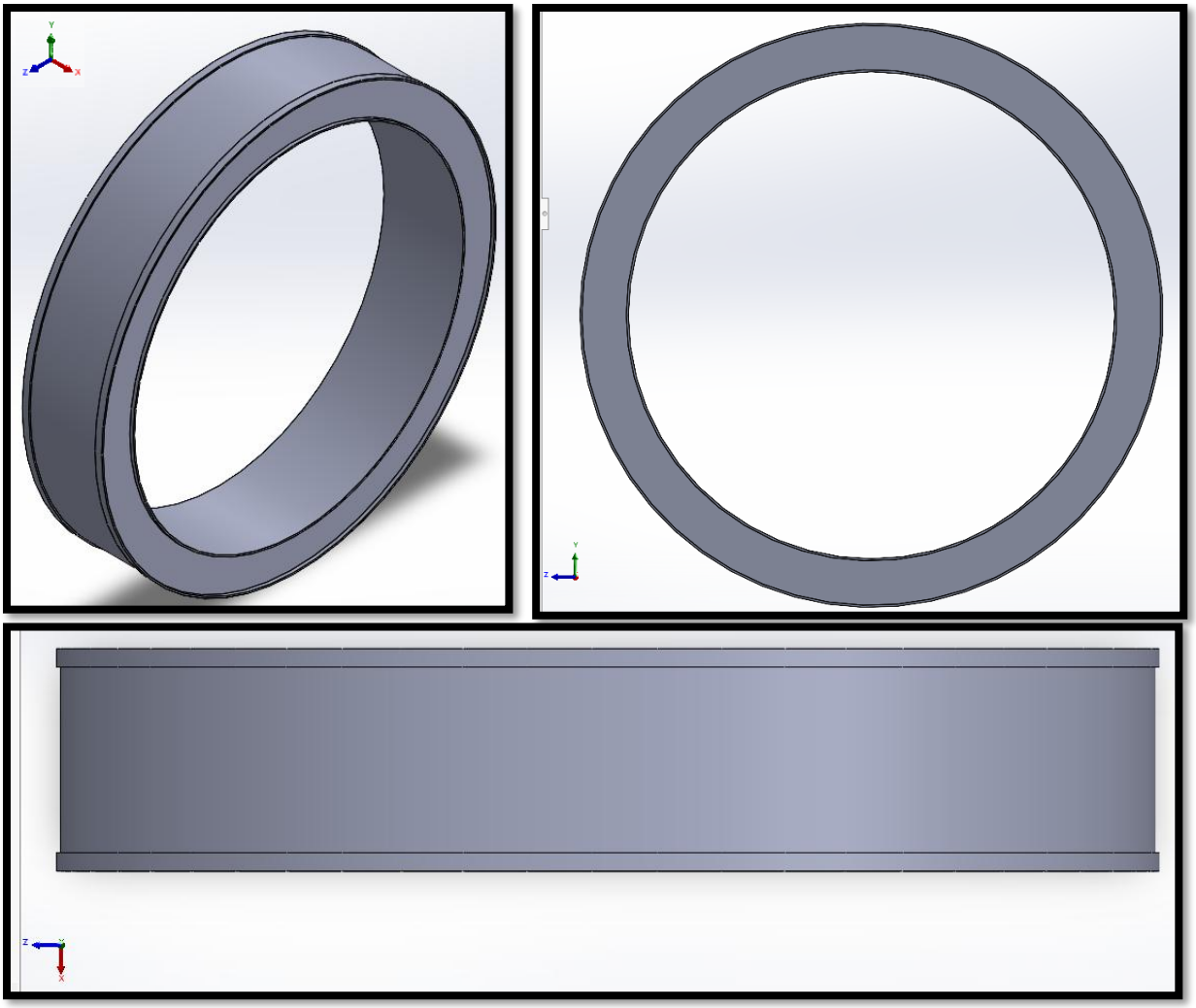

Figure 3.14 – Isometric, front, and top view of the Titanium O-ring Interface in SolidWorks ®.

3.2.3 Stern, Spherical Section

The general geometry of the stern and bow spherical directions is nearly identical. The distinction between the two is the embedded observation window, which is only present at the bow section, as can be observed in figure 3.15. The purpose of the stern spherical section was to store mission-essential equipment for the survivability of humans at normal atmospheric conditions. Among this equipment were soda lime pellets, required to remove the CO_2 from the cabin, and electrical systems for navigation and control of the submersible [39]. Although no real-life pictures of the stern spherical section were available, figure 3.16, representing the bow section [42], provides three pieces of valuable insight into the geometry of this component. First is the realization that surface meeting the O-Ring is slightly protruded in the radial direction to match the outer diameter of the O-Ring. Second is the observation that the thickness of this protruded surface is similar to the O-Ring section. Third is the visual confirmation that the section is, in fact, spherical rather than ellipsoidal. This component is characterized by four dimensions: inner diameter, wall thickness, thickness of O-Ring interface wall, and outer diameter of O-Ring

interface wall. The first two values were extracted from Wikipedia [7], while engineering judgment was used to determine the values of the last two, as summarized in table 3.4, below.

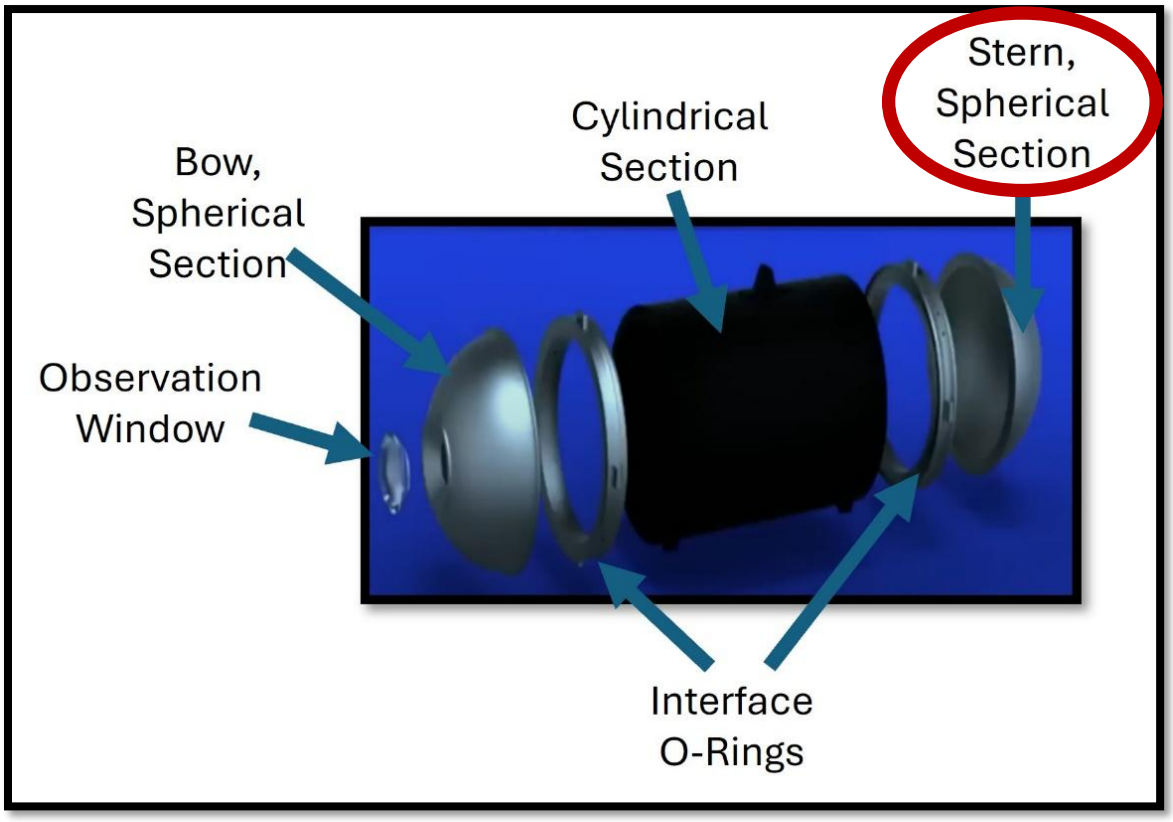

Figure 3.15 – Stern, Spherical Section and additional components of the Titan Submersible.

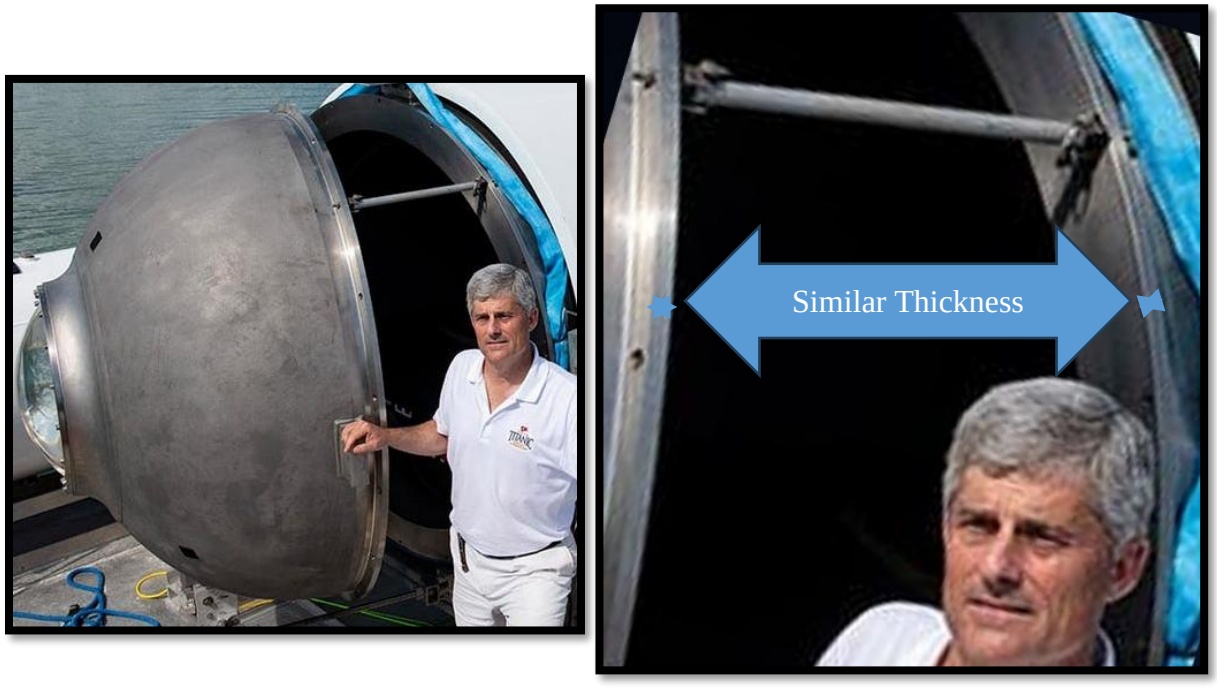

Figure 3.16 – Bow, Spherical Section (in lieu of the Stern, Spherical Section) [42].

Table 3.4 - Stern, spherical section dimensions and information source.

Component Name	Dimension		Source
Stern Spherical Section	Inner Diameter [m]	1.4022	Wikipedia [7]
	Thickness [cm]	8.26	Wikipedia [7]
	Thickness, O-Ring Interface Wall [cm]	2.80	Engineering Judgement
	Outer Diameter, O-Ring Interface Wall [m]	1.7762	Engineering Judgement

The two-dimensional sketch based on the dimensions of table 7 was then developed and is shown in figure 3.17. After revolving this enclosed surface once about the x-axis, its corresponding three-dimensional profile was created. From the top left corner, proceeding clockwise, figure 3.18 shows the isometric, side, and back profiles of this component.

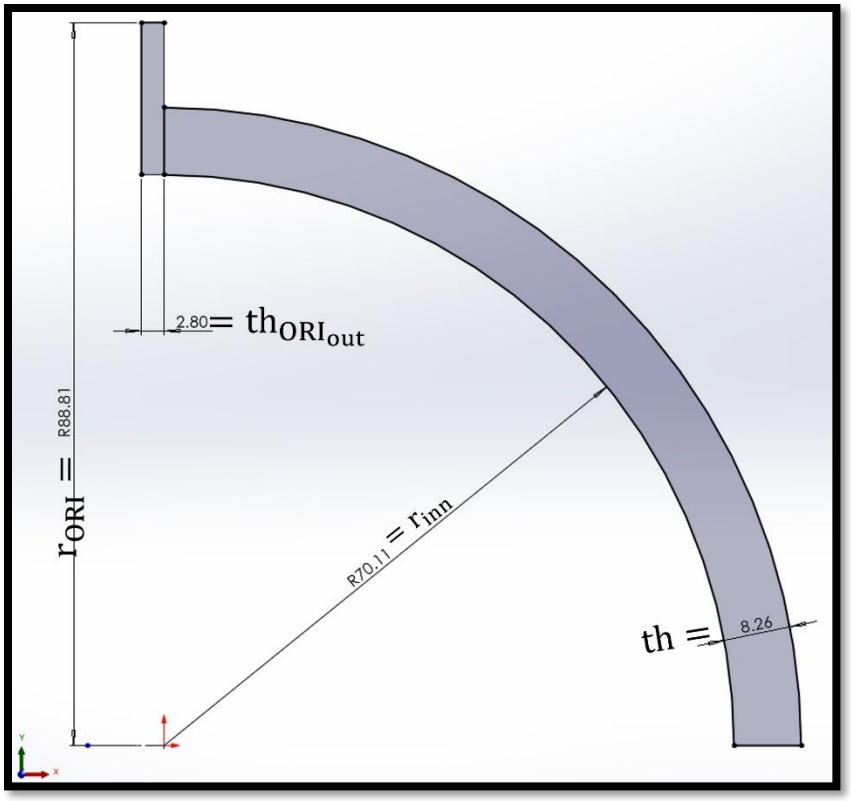

Figure 3.17 - Two-dimensional sketch model of the Stern, Spherical Section.

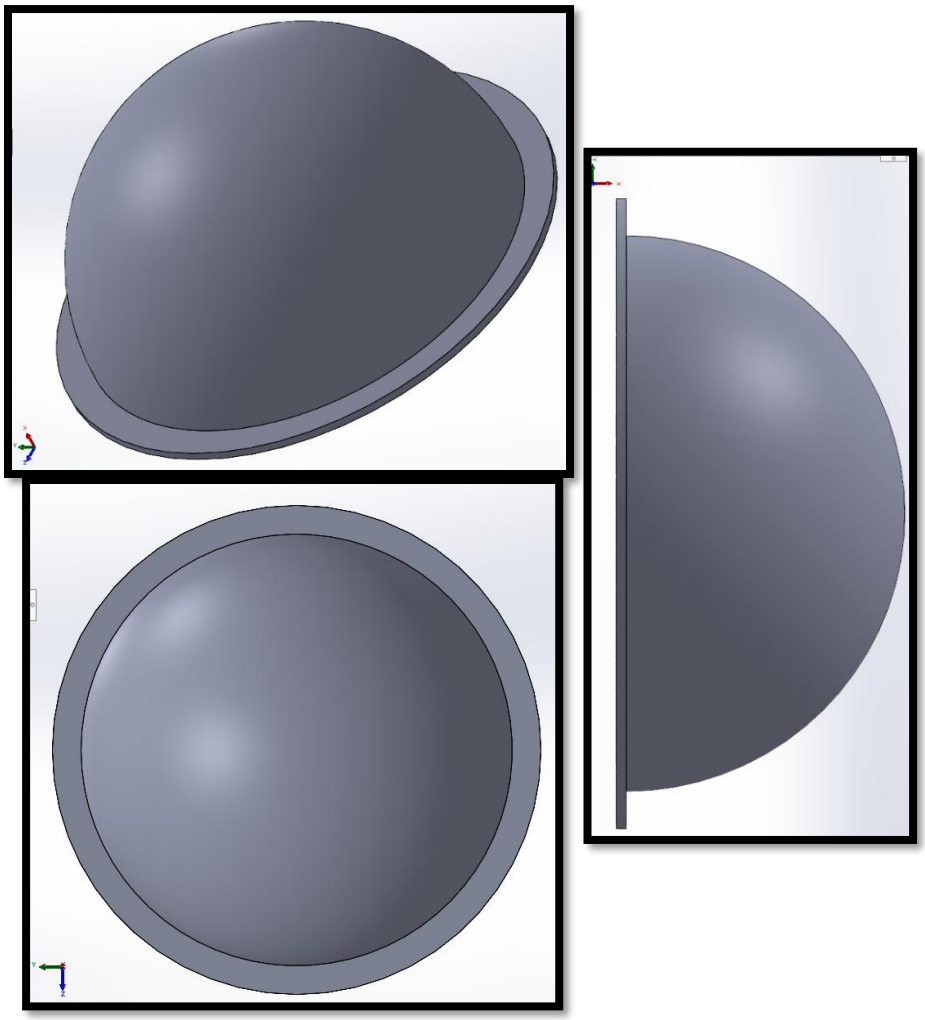

Figure 3.18 - Isometric, side, and front view of the Stern, Spherical Section in SolidWorks ®.

3.2.4 Bow, Spherical Section

As signaled in the previous subsection, the bow spherical section has an embedded observation window; this is illustrated by figure 3.19. In addition to providing access and the structural connection to the observation window, this section was reported to be assigned as a latrine area. The same procedure to develop the base sketch of the stern, spherical section was followed at first, implementing the first four dimensions in table 3.5. Since the geometry of the observation window was described to have an inner and outer diameter of 38 and 53 cm, respectively [7, 38], the corresponding intersection coordinates were found, as shown in figure 3.20. Then, a revolved cut was performed, which led to the creation of its corresponding three-dimensional profile. From the top left, moving clockwise, figure 3.21 shows the side, isometric, and front profiles of this component.

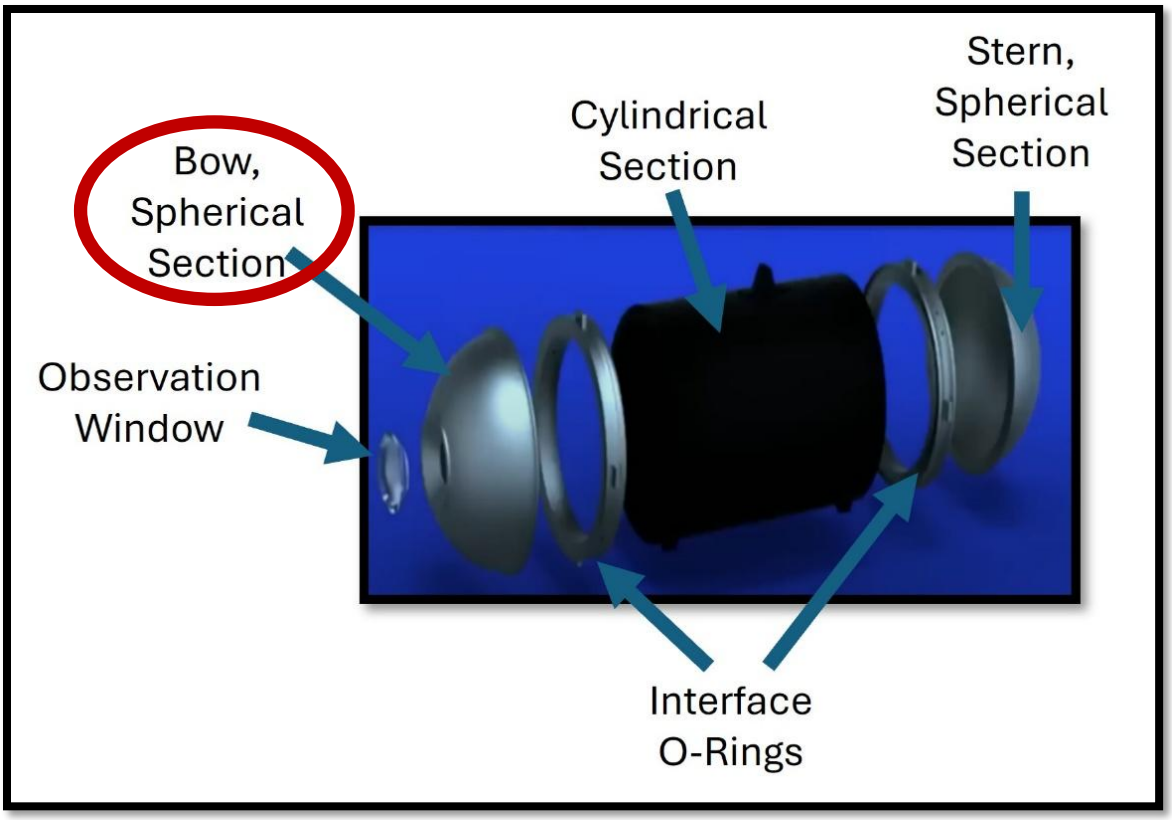

Figure 3.19 – Bow, Spherical Section and additional components of the Titan Submersible.

Table 3.5 - Bow, spherical section dimensions and information source.

Component Name	Dimension		Source
Bow Spherical Section	Inner Diameter [m]	1.4022	Wikipedia [7]
	Thickness [cm]	8.26	Wikipedia [7]
	Thickness, O-Ring Interface Wall [cm]	2.80	Engineering Judgement
	Outer Diameter, O-Ring Interface Wall [m]	1.7762	Engineering Judgement
	Base Diameter Intersection, Observation Window [cm]	38.0	Wikipedia [7]
	Outer Diameter Intersection, Observation Window [cm]	53.0	ThinkReliability.com [38]

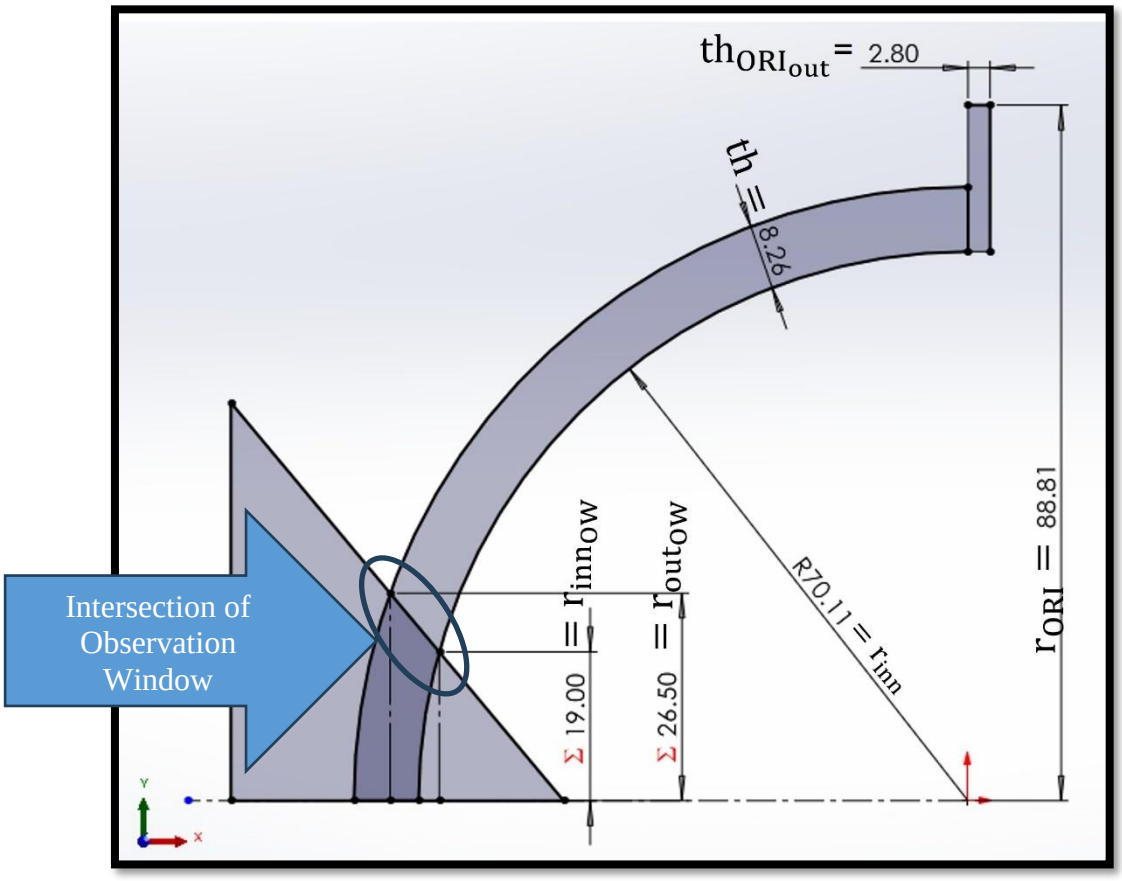

Figure 3.20 - Two-dimensional sketch model of the Bow, Spherical Section.

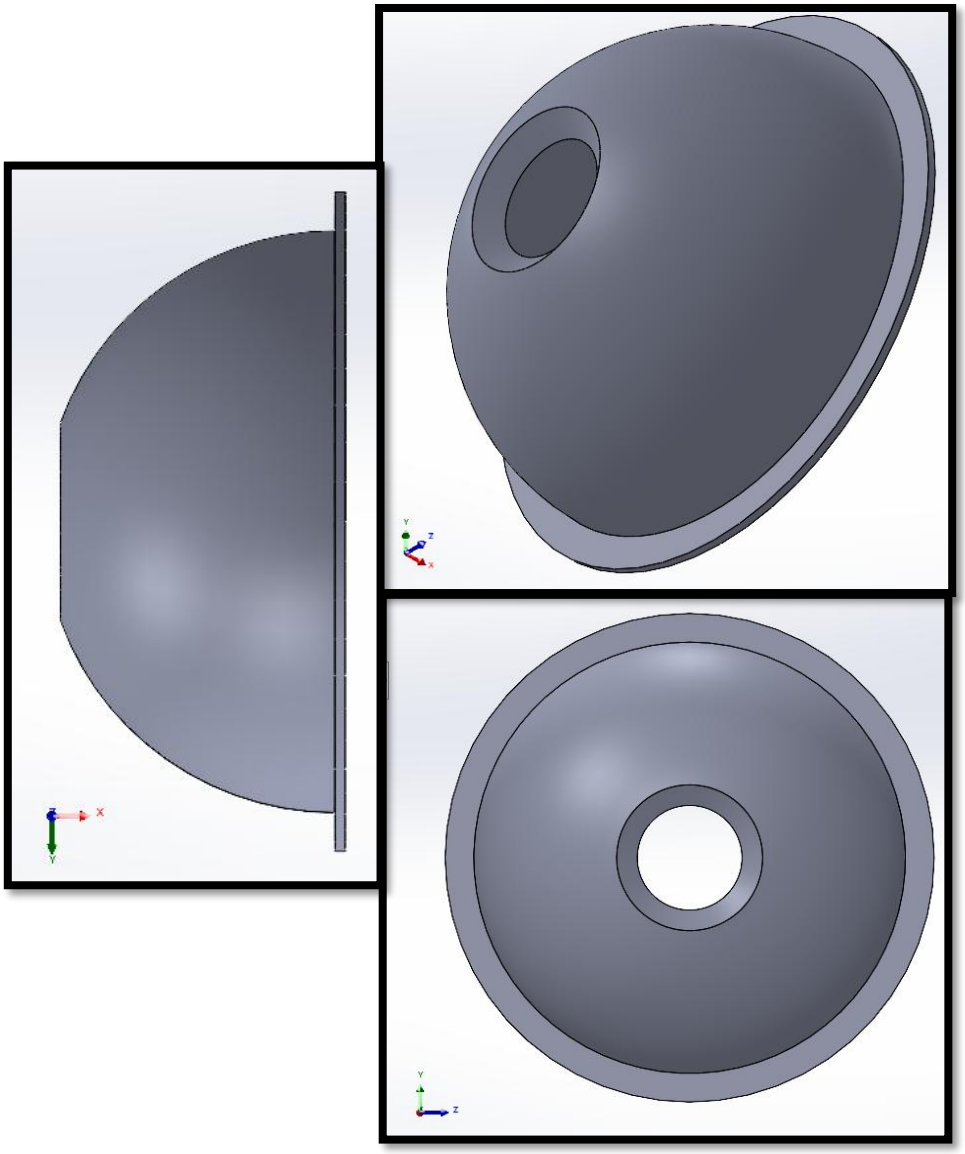

Figure 3.21 - Side, isometric, and front view of the Stern, Spherical Section in SolidWorks ®.

3.2.5 Observation Window

The observation window of the submersible provided the passengers with a direct access port to observe the wreckage of the Titanic. It is labeled below, in figure 3.22. The most valuable real-life image is shown in figure 3.23. This frame was taken from a video [37], where OceanGate employees appear to carry the uninstalled PPMA observation window. Measurements provided by Wikipedia [7] and ThinkReliability,com [38] appear to be in qualitative agreement: the base and outer diameter of this component are recorded as 38.0 and 53.0 cm, respectively. While the radius of curvature of the window was not included, engineering judgement strongly suggests that this curvature is similar to that followed by the bow spherical section. Using SolidWorks ®, the horizontal intersection coordinates of the window base and outer diameters were found to be 67.49

and 73.75cm, while the radius of the spherical section was 78.37cm. These dimensions are summarized in table 3.6, located below.

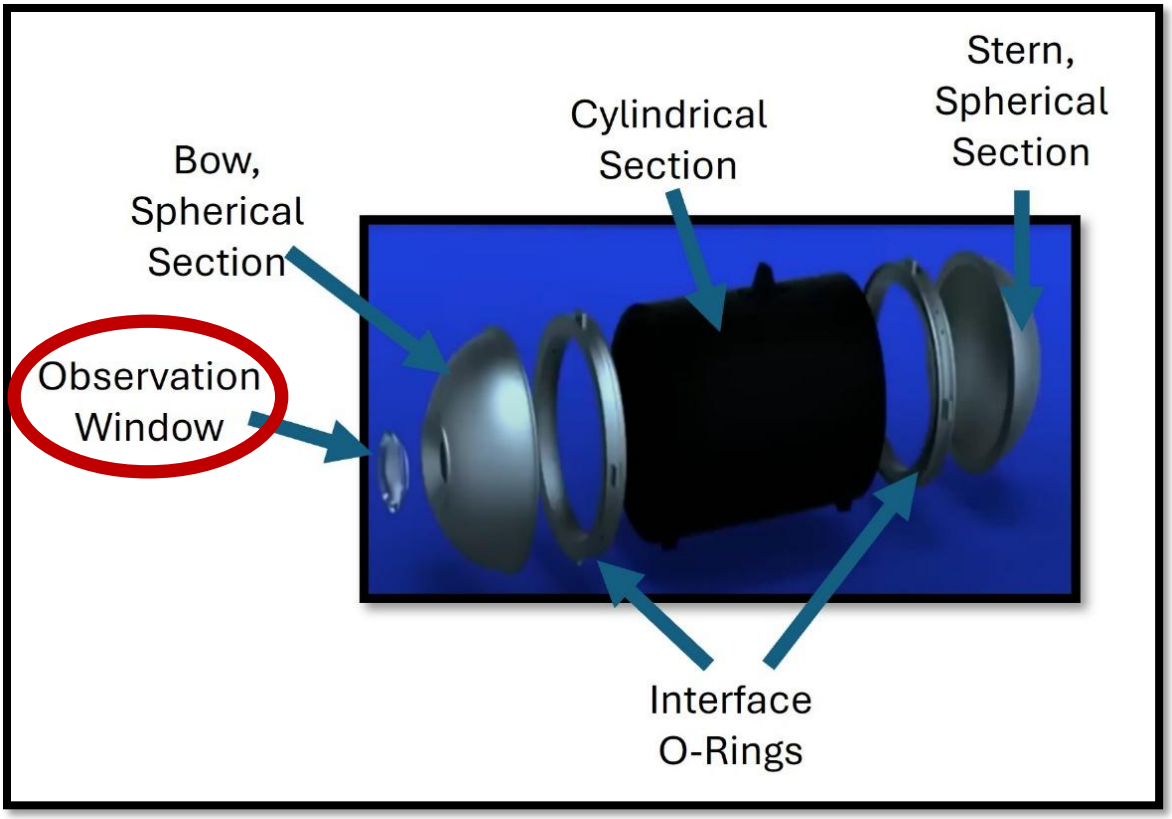

Figure 3.22 – Observation Window and additional components of the Titan Submersible.

Figure 3.23 – Uninstalled Observation Window [37].

Table 3.6 - Observation window dimensions and information source.

Component Name	Dimension		Source
PPMA Observation Window	Base Window Diameter [m]	38.0	Wikipedia [7]
	Exterior Window Diameter [cm]	53.0	TinnkReliability.com [38]
	Base Window Diameter, x-intersection [cm]	67.49	Engineering Judgement
	Exterior Window Diameter, x-intersection [cm]	73.75	Engineering Judgement
	Window Outer Radius of Curvature [cm]	78.37	Engineering Judgement

Implementing the previous dimensions, a two-dimensional base profile was then created, as shown in figure 3.24. This enclosed area was revolved 360 degrees about the x-axis, which

created a three-dimensional profile. From the top, moving clockwise, figure 3.25 shows the isometric, side and front views of the observation window.

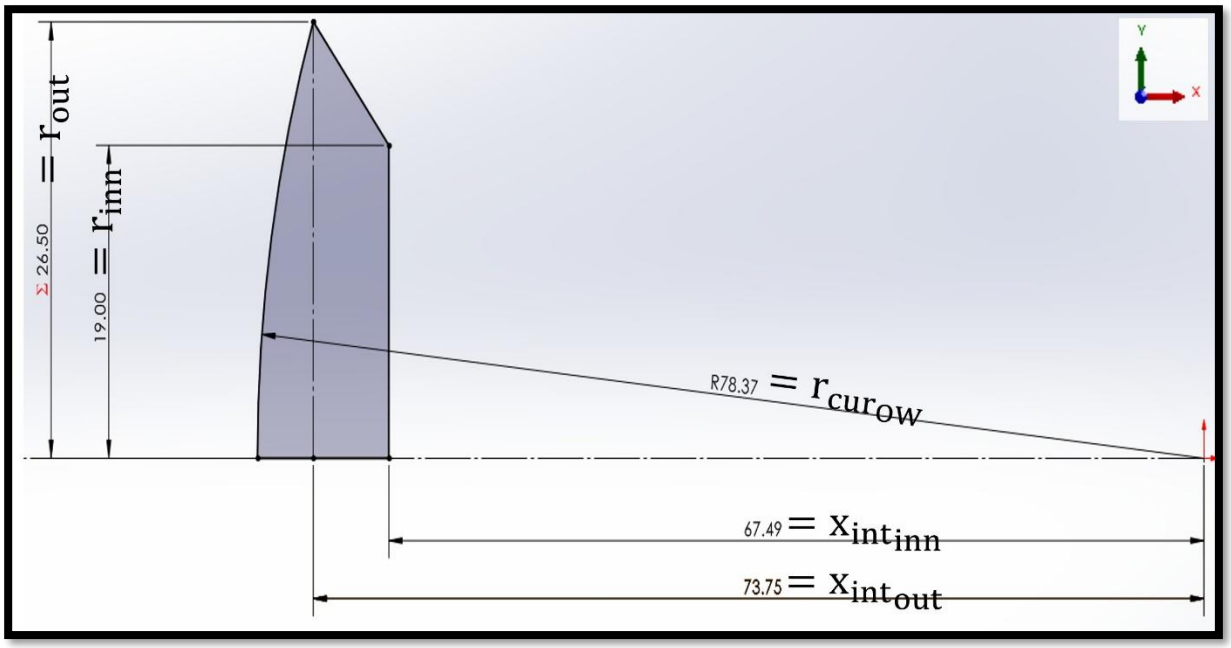

Figure 3.24 - Two-dimensional sketch model of the Observation Window.

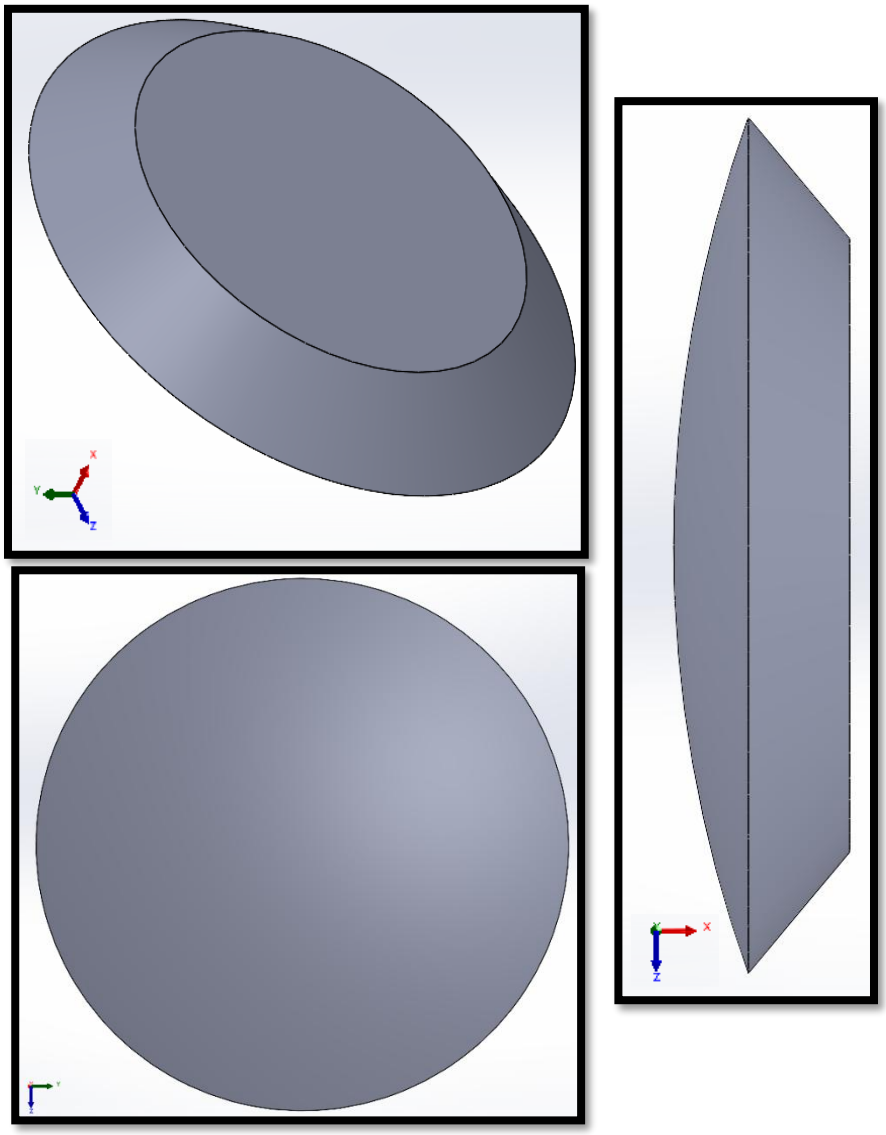

Figure 3.25 - Side, isometric, and front view of the Stern, Spherical Section in SolidWorks ®.

3.2.6 Final Assembly

After the three-dimensional representation of each of the previous components was developed, the assembly process followed. Creating a 3D representation of an object in SolidWorks is also known, more informally, as a creating a *part*. In this context, the assembly refers to the process of constructing a final, single 3D representation using a several parts. As a result, the assembly of the five components developed in sections 3.2.1 to 3.2.5 led to the final Titan Submersible model shown in figure 3.26. From the top left, moving clockwise, the isometric, front, and side views are contrasted in figure 3.27.

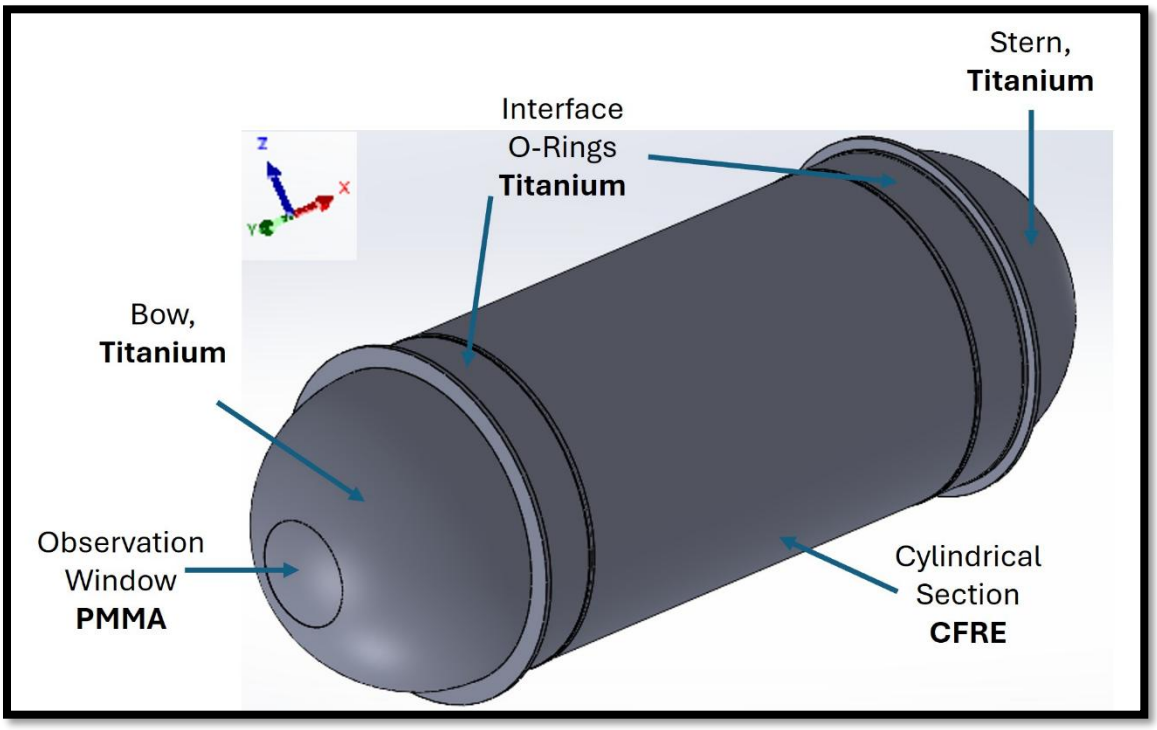

Figure 3.26 – Assembly of the Titan Submersible using its five main components.

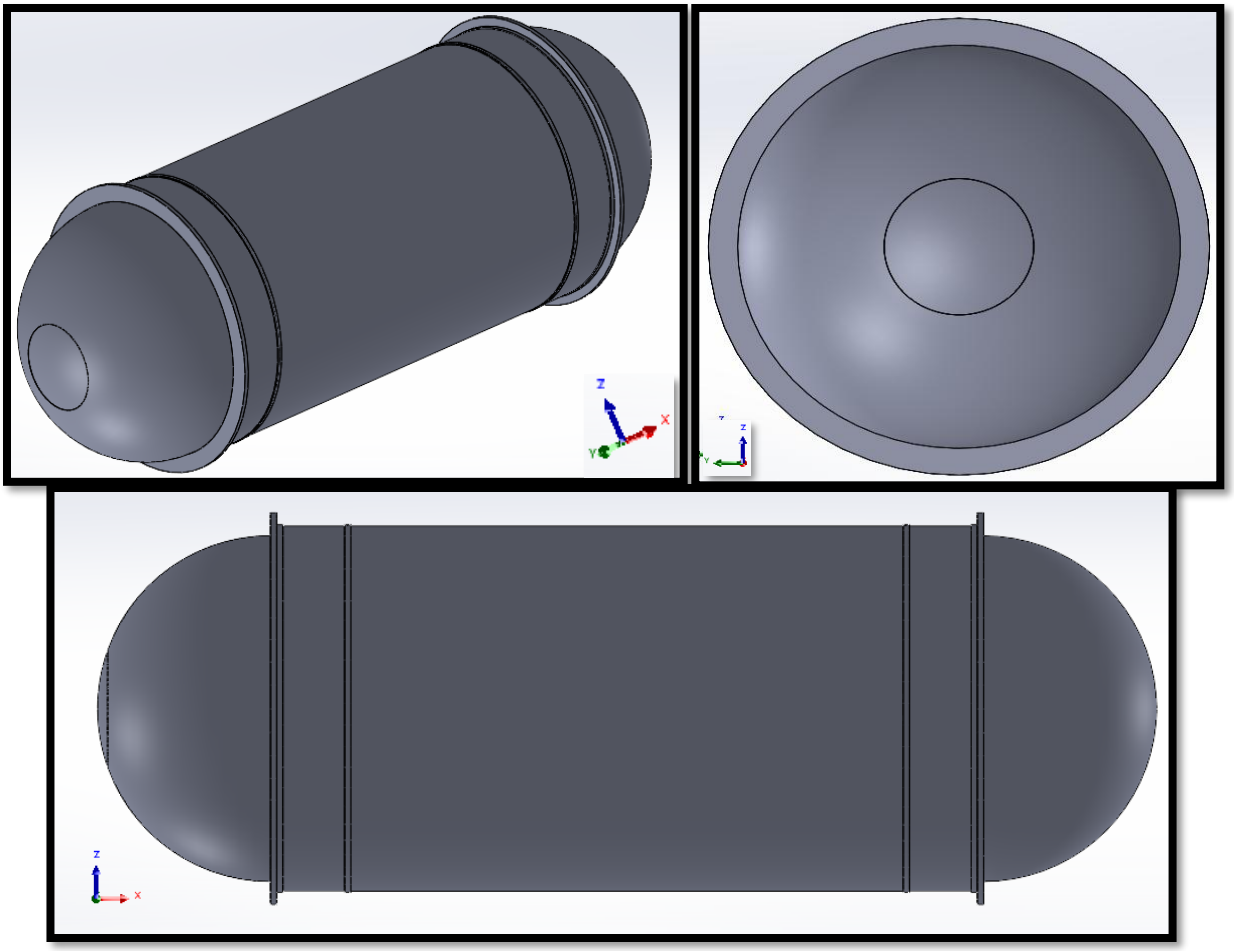

Figure 3.27 – Isometric, front, and side views of the final assembly of the Titan Submersible.

3.3 Assumptions and Limitations

The proposed, rapid three-dimensional prototype of the Titan Submersible was constructed implementing a series of assumptions, for which there are associated limitations. One of these principal assumptions is the component simplification in the geometry model. Components that can be observed in footage of the operational Titan Submersible, such as those denoted in figure 3.28, are examples of exclusions from the presented geometry model. These are, for example, electrical wiring cables, navigation thrusters, the outer white shell, and the landing skids. The second chief assumption is the bonding between connecting components is unbreakable. During the manufacturing process of the submersible [40], OceanGate collaborators were observed applying adhesive to glue the CFRE pressure hull to the Titanium Interface O-Rings. Similarly, footage shows that the bow hemisphere was attached to the O-Ring through bolts [42]. These two characteristics can be visualized in figure 3.29. In third place is the adoption of a simplified topology compared to that of the Titan Submersible. For example, the proposed model does not include the fillets that can be observed in the O-Ring, or the protruded prismatic surfaces to connect other components, as these were excluded from the analysis. The observation window seat is another example. Because it was assumed to be perfectly bonded to the bow hemisphere, no bolts

or connecting surface were modeled. These aspects can be observed in figure 3.30. Lastly, there is unavoidable uncertainty in implementing dimensions from available resources, and the only way to verify the veracity of these sources is by physically measuring these dimensions. All these discussed assumptions and limitations are summarized in table 3.7, located below.

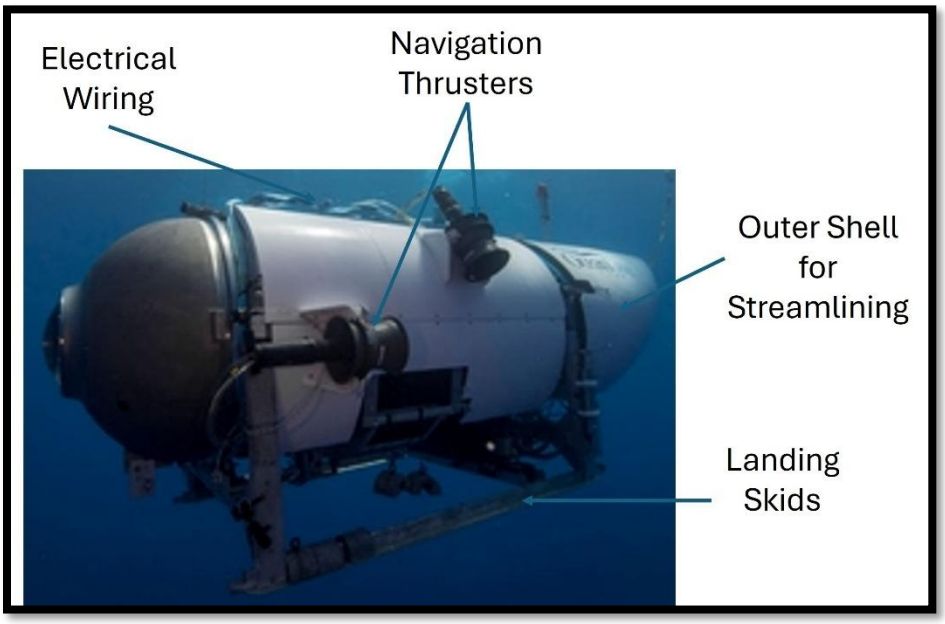

Figure 3.28 – Visualization of some components excluded from the simplified geometry model [7].

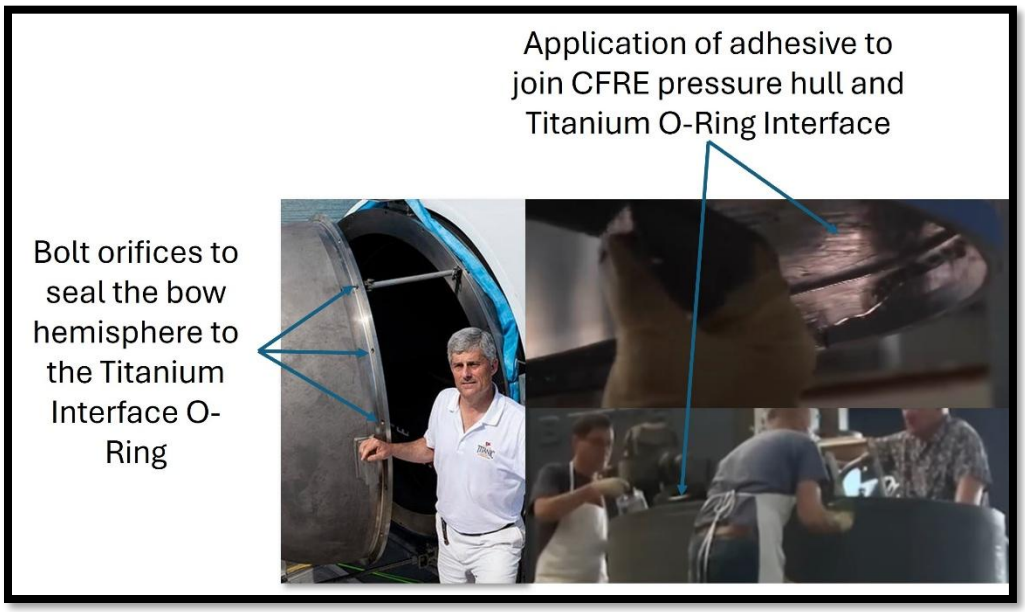

Figure 3.29 – Instances of component bonding in the operational Titan Submersible [42, 40].

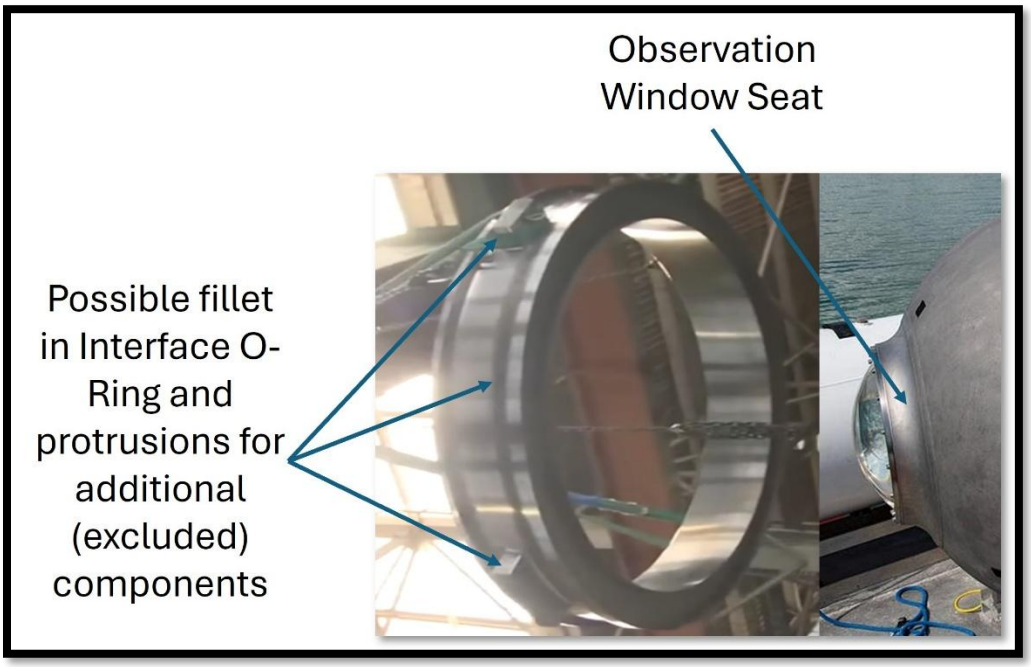

Figure 3.30 – Visualization of some components excluded from the simplified geometry model [40, 42].

Table 3.7 - Summarized assumptions and limitations with the proposed geometry model.

Assumption	Associated Limitation
Component Simplification	Failure could have originated in the small, excluded components, such as connecting bolts, cables, or corresponding orifices. This possibility is excluded from this analysis.
Component Bonding	Components are assumed to have a perfectly unbreakable bond. The possibility of failure caused by the adhesive use to bond the CFRE pressure full and the Titanium Interface O-Rings is not considered. The same is assumed for the boding between the PPMA observation window and the bow, Titanium spherical section.
Simplified Topology	Specific topological features, such as fillets in corners of the interface O-Ring and the base collar of the observation window are not considered in this stage of the analysis. This topology will be optimized in chapter XXXX.
Uncertainty in Dimensions	Without physical confirmation of these dimensions, they are no more than an approximation.

4. Analytical Prediction of Displacement and Buckling Load of the Cylindrical Laminated Composite Section of Titan Submersible

4.1 Mathematical Model: Introduction

In preparation to generate the FEM solution for the proposed problem using Ansys, a rapid analytical approach was first implemented. Unlike isotropic materials, such as metals, the mechanical properties of laminated composite structures are heavily dependent on the selected constituents and orientation. This was previously identified in the literature review, conducted in section 1.3. As a result, the cylindrical section of the Titan Submersible, composed of CFRE, was selected to predict the displacements and buckling load using shell theory for laminated composites. These properties are bulletized for convenience to the reader.

- Displacements: Axial, Radial, and Circumferential, in [mm].
- Buckling Load, in [N]

Although analytical solutions are limited and constricted under a set of assumptions, these methods can provide three main advantages before the use of computer-aided engineering to investigate a problem of interest. The first and most obvious advantage is to gain a fundamental understanding of the physical phenomena being studied, identify properties of interest, and understand the set of assumptions under which the mathematical model is valid. Another benefit of analytical methods is the generation of benchmarking data which can then be compared to numerical solutions produced through computer software. This can provide the engineering analyst with an appropriate qualitative and quantitative judgement of the properties of interest, such as magnitude of displacement and locations where stresses are the largest. Lastly, the dimensions of the cylindrical component, estimated in section 3.2.1, can be easily corroborated by first assessing the analytical results. This can save the analyst computational resources (available computational time, electricity, wear-and-tear of computer equipment) before undertaking the task of developing a FEA simulation.

To investigate the displacements and buckling of the laminated composite geometry of interest, three different approaches were first considered, as reflected in Table 4.1. These were flat plate theory, composite beam theory, and shell theory. As its name implies, flat plate theory is limited to geometries with no significant curvature. While a cylindrical structure, such as the one subject of this study, can be considered as a cylindrical beam, composite beam theory is not intended to account for curvature effects. Moreover, shell theory is intended for inherently curved structures, such as spheres and cylinders. As a result, this theory was adopted to develop the analytical mathematical model and generate the properties of interest.

Table 4.1 - Comparison of analytical methods for composite structures [43].

Method	Flat Plate Theory	Composite Beam Theory	Shell Theory
Intended Geometry	Thin, flat plates	Long, slender beams	Cylindrical and spherical shapes
Brief Description	Used for analysis of large, flat panels with no curvature.	Used for beams where axial and flexural behaviors are dominant.	Used for structures with curvature.
Main Assumptions	Thickness is smaller compared to other dimensions. Strains vary linearly across plate. Shear deformations are negligible. The dominant stresses are in-plane: $\sigma_x, \sigma_y, \tau_{xy} >> \sigma_z$	Shear deformations are neglected. Axial, transverse, and torque loads can be applied to the model. Curvature effects are not well accounted.	Thin shells resist loads by membrane forces, which are tangent to the reference surface at any point. Bending moments are neglected. Results are reasonable except near supports and areas of abrupt changes in loading.

4.1.1 Shell Theory for Cylindrical Laminated Composites: Critical Assumptions

Unlike plates, which resist transverse loads through bending and transverse shear forces, thin shells resist these loads through membrane forces. These membrane forces exist in the corresponding plane tangential to the reference surface. The mathematical model associated to determine these membrane forces is referred to as *the membrane theory of shells* by Kollar and Springer [43], whose work and findings are developed in the entirety of this and the following two subsections. They outlined the following assumptions and limitations to the proposed theory.

- The theory uses underlying assumptions of thin plate theory:
  - The laminate undergoes small displacements.
  - Strains vary linearly across the thickness direction (out-of-plane).
  - Shear deformations are negligible.
  - Out-of-plane normal stress σ_z and shear stress τ_{xz} and τ_{yz} are small compared to the in-plane normal σ_x, σ_y, and shear τ_{xy} stresses.
- Bending moments are neglected.
- Cylinder thickness, h, is small compared with all other dimensions.
- Membrane forces are dependent on geometry, boundary conditions, and applied loads; they are independent of material properties.
- Changes in curvature do not affect the stresses.

- Results predicted through this theory are reasonable except near the supports and areas of abrupt changes in loads.

As mentioned in the third series of assumptions, this analysis starts assuming that the thickness, h, is smaller than other dimensions, so that the membrane forces can be determined according to equations 4.1 to 4.4. Coordinates x, y, and z represent the local coordinates, where x and y exist in the plane tangential to the reference point of interest, while z is perpendicular. This is better visualized in figure 4.1, adapted from [43]. In the previous equations, N_x, N_x, N_x, and N_x represent the membrane forces acing at the reference surface of an infinitesimal element; R_x and R_y are the local radii of curvature. The origin of the coordinate system is taken to be the midsurface, so that the limits of integration h_b and h_t correspond to the back coordinate and top distance of the shell thickness. Implementing the assumption of a thin shell, so that z approaches 0, reduces equations 4.1 through 4.4 into 4.5 to 4.8

$$N_x = \int_{-h_b}^{h_t} \sigma_x \left(1 + \frac{z}{R_y}\right) dz \quad (4.1)$$

$$N_y = \int_{-h_b}^{h_t} \sigma_y \left(1 + \frac{z}{R_x}\right) dz \quad (4.2)$$

$$N_{xy} = \int_{-h_b}^{h_t} \tau_{xy} \left(1 + \frac{z}{R_y}\right) dz \quad (4.3)$$

$$N_{yx} = \int_{-h_b}^{h_t} \tau_{yx} \left(1 + \frac{z}{R_x}\right) dz \quad (4.4)$$

$$N_x = \int_{-h_b}^{h_t} \sigma_x dz \quad (4.5)$$

$$N_y = \int_{-h_b}^{h_t} \sigma_y dz \quad (4.6)$$

$$N_{xy} = \int_{-h_b}^{h_t} \tau_{xy} dz \quad (4.7)$$

$$N_{yx} = \int_{-h_b}^{h_t} \tau_{yx} dz \quad (4.8)$$

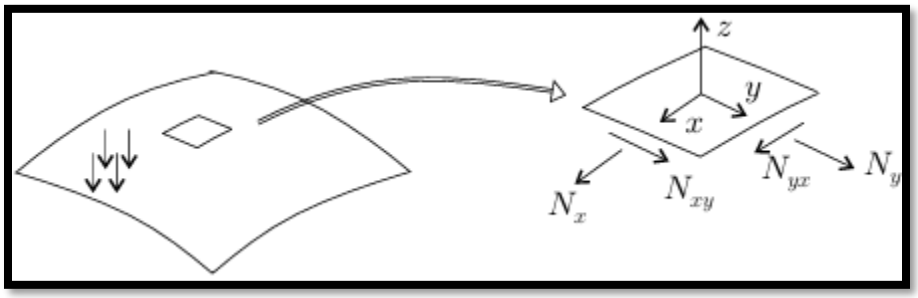

Figure 4.1 – Representation of membrane forces in a shell [43].

Implementing the fourth critical assumption, namely the independence of membrane forces on the material properties of the analyzed geometry, the equations of static equilibrium, 4.9, can be used to determine the membrane forces. In more detail, the 6-by-6 matrix in equation 4.9 is referred to as the ABD matrix, which can be understood as the *stiffness* response of a laminate to in-plane forces and moments.

$$\begin{Bmatrix} N_x \\ N_y \\ N_{xy} \\ M_x \\ M_y \\ M_{xy} \end{Bmatrix} = \begin{bmatrix} A_{11} & A_{12} & A_{16} & B_{11} & B_{12} & B_{16} \\ A_{12} & A_{22} & A_{26} & B_{12} & B_{22} & B_{26} \\ A_{16} & A_{26} & A_{66} & B_{16} & B_{26} & B_{66} \\ B_{11} & B_{12} & B_{16} & D_{11} & D_{12} & D_{16} \\ B_{12} & B_{22} & B_{26} & D_{12} & D_{22} & D_{26} \\ B_{16} & B_{26} & B_{66} & D_{16} & D_{26} & D_{66} \end{bmatrix} \begin{Bmatrix} \epsilon_x^0 \\ \epsilon_y^0 \\ \gamma_{xy}^0 \\ \kappa_x \\ \kappa_y \\ \kappa_{xy} \end{Bmatrix} \quad (4.9)$$

Although the derivation of the ABD matrix is beyond the scope of this work, the details leading to its development can be obtained in chapters 2 and 3 of [43]. Mathematically, the ABD matrix of a laminate is defined by the stiffness matrices in equations 4.10 through 4.12, and are defined by the elements i, j = 1, 6. Because [Q] is constant across each ply, these equations can take the form of the summations in equations 4.13 through 4.15, where k reflects to each individual ply number. For a laminate of an arbitrary number of layers, oriented at any angle, its ABD matrix can be assembled by first developing the reduced stiffness coefficient matrix Q, which is expressed by equation 4.16. The elastic modulus in the longitudinal and transverse directions are represented by E_1 and E_2, respectively, while the longitudinal Poisson's ratio is denoted by ν_{12}. The longitudinal shear modulus is given by G_{12}, and the engineering constant D, is expressed by equation 4.17, and created merely for convenience. This set of mechanical properties are dependent on the composite structure constituents, namely the fiber and the matrix, and can be determined mathematically through the "rules of mixture", whose development is deferred to section 4.2. Once the Q matrix has been built, the ABD matrix can be developed by considering the contribution of each other laminate with respect to an arbitrarily defined reference plane, as illustrated in figure 4.2. When a ply is oriented at a non-zero angle, like the reference Q matrix, rotation matrices must be used to reflect the express the properties of that matrix in the original frame of refence. To achieve this objective, the rotation matrices outlined by equations 4.18a and 4.18b must be built and later multiplied by Q, as expressed by 4.19. Letters c and s denote the cosine and sine of the corresponding fiber orientation of ply k, at angle theta, assumed to be positive when measured from the +x to the +y axis.

$$[A] = \int_{-h_b}^{h_t} [Q]dz = A_{i,j} = \int_{-h_b}^{h_t} Q_{i,j}dz \quad (4.10)$$

$$[B] = \int_{-h_b}^{h_t} z[Q]dz = B_{i,j} = \int_{-h_b}^{h_t} zQ_{i,j}dz \quad (4.11)$$

$$[D] = \int_{-h_b}^{h_t} z^2[Q]dz = D_{i,j} = \int_{-h_b}^{h_t} z^2Q_{i,j}dz \quad (4.12)$$

$$A_{i,j} = \sum_{k=1}^{K} \left(Q_{ij}\right)_k (z_k - z_{k-1}) \quad (4.13)$$

$$B_{i,j} = \frac{1}{2}\sum_{k=1}^{K} \left(Q_{ij}\right)_k (z_k^2 - z_{k-1}^2) \quad (4.14)$$

$$D_{i,j} = \frac{1}{3}\sum_{k=1}^{K} \left(Q_{ij}\right)_k (z_k^3 - z_{k-1}^3) \quad (4.15)$$

$$[\mathrm{Q}] = \begin{bmatrix} \frac{E_1}{D} & \frac{\nu_{12}E_2}{D} & 0 \\ \frac{\nu_{12}E_2}{D} & \frac{E_2}{D} & 0 \\ 0 & 0 & G_{12} \end{bmatrix} \quad (4.16)$$

$$D = 1 - \frac{E_2}{E_1}\nu_{12}^2 \quad (4.17)$$

$$[\mathrm{T}_\sigma] = \begin{bmatrix} c^2 & s^2 & 2cs \\ s^2 & c^2 & -2cs \\ = cs & cs & c^2 - s^2 \end{bmatrix} \tag{4.18a}$$

$$[\mathrm{T}_\epsilon] = \begin{bmatrix} c^2 & s^2 & cs \\ s^2 & c^2 & -cs \\ -2cs & 2cs & c^2 - s^2 \end{bmatrix} \tag{4.18b}$$

$$[Q^k] = [[\mathrm{T}_\sigma]][Q][\mathrm{T}_\epsilon] \tag{4.19}$$

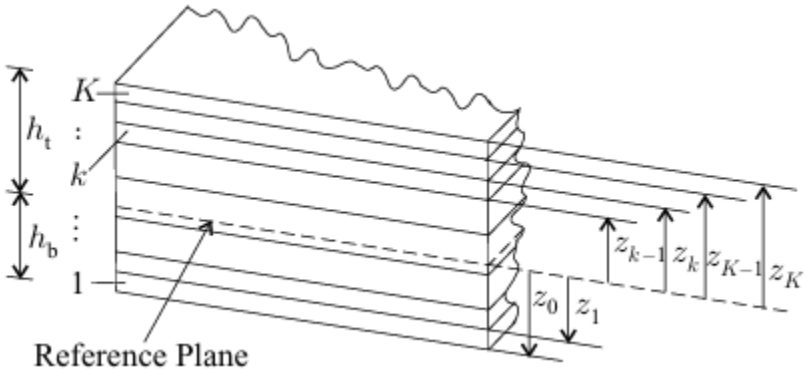

Figure 4.2 – Visualization of the distances of other laminates with respect to the reference plane [43].

Consequently, implementing the fifth assumption, the curvatures become 0, and 4.9 reduces to equation 4.20, where ϵ_x^0, ϵ_y^0, and γ_{xy}^0 represent the strains of the reference surface. By neglecting the variations of strains across the shells, the strains can be described by equation 4.21. Finally, this implies that the stresses in each layer can be calculated by equation 4.22. These fundamental assumptions are the base to develop the resulting mathematical models for composite shells described in the next two sub-sections, 4.1.2 and 4.1.3.

$$\begin{Bmatrix} \epsilon_x^0 \\ \epsilon_y^0 \\ \gamma_{xy}^0 \end{Bmatrix} = \begin{bmatrix} A_{11} & A_{12} & A_{16} \\ A_{12} & A_{22} & A_{26} \\ A_{16} & A_{26} & A_{66} \end{bmatrix}^{-1} \begin{Bmatrix} N_x \\ N_y \\ N_{xy} \end{Bmatrix} \tag{4.20}$$

$$\begin{Bmatrix} \epsilon_x \\ \epsilon_y \\ \gamma_{xy} \end{Bmatrix} = \begin{Bmatrix} \epsilon_x^0 \\ \epsilon_y^0 \\ \gamma_{xy}^0 \end{Bmatrix} \tag{4.21}$$

$$\begin{Bmatrix} \sigma_x \\ \sigma_y \\ \tau_{xy} \end{Bmatrix} = \begin{bmatrix} Q_{11} & Q_{12} & Q_{16} \\ Q_{12} & Q_{22} & Q_{26} \\ Q_{16} & Q_{26} & Q_{66} \end{bmatrix} \begin{Bmatrix} \epsilon_x \\ \epsilon_y \\ \gamma_{xy} \end{Bmatrix} \tag{4.22}$$

4.1.2 Membrane Theory: Prediction of Displacements

The analyzed geometry is treated as a thin-walled cylinder with built-in ends, such as the one in figure 4.3a. It can be subjected to a pressure P_z, which may vary linearly along the radial direction, and a constant axial load $\hat{N}$ and constant torque $\hat{T}$. For these applied loads, the corresponding forces and moments inside the wall of the cylinder are shown in figure 4.3b. The uppercase letters M, N, and V represent the moments, forces, and shear forces, and the subindices x, y, and z denote the corresponding direction or plane where they occur. R represents the radial distance from the main axis of the cylinder to its outer surface. Consequently, five equilibrium relationships can now be established, as summarized by 4.23 through 4.27. The strains and curvatures of the reference surface are then expressed by equations 4.28a through 4.29c. Axial, circumferential, and radial displacements, the properties of interest for this subsection, are denoted by u^0, v^0, and w^0, respectively.

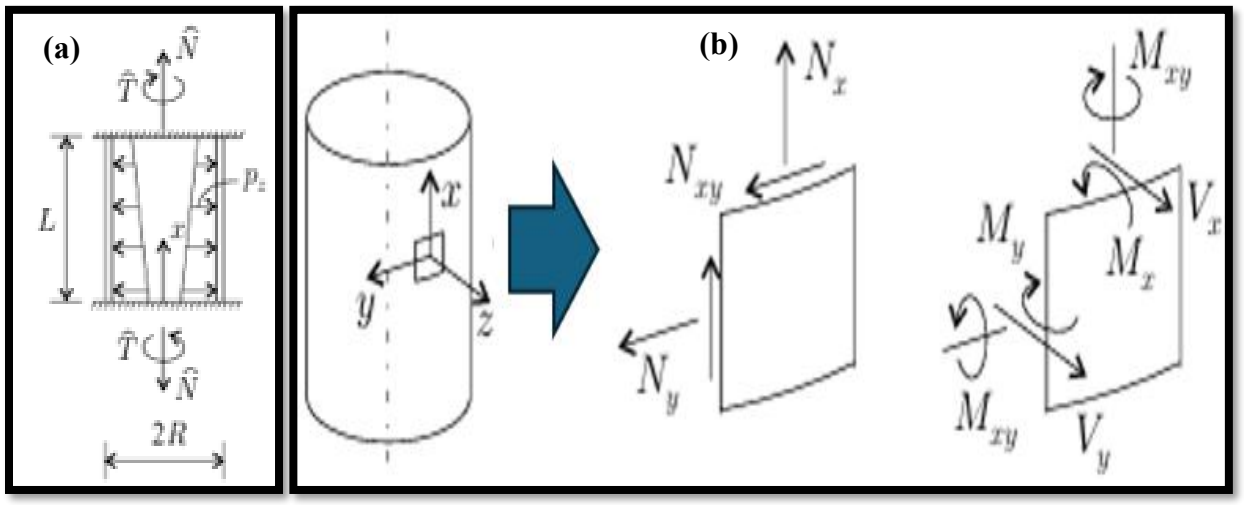

Figure 4.3 – a) Cylinder model and its acceptable applied loads. b) Forces and moments inside the wall [43].

$$\frac{dN_x}{dx} = 0 \tag{4.23}$$

$$\frac{d}{dx}\left(RN_{xy} + M_{xy}\right) = 0 \tag{4.24}$$

$$\frac{N_y}{R} - \frac{d^2M_x}{dx^2} = P_z \tag{4.25}$$

$$V_x = \frac{dM_x}{dx} \tag{4.26}$$

$$V_y = \frac{dM_{xy}}{dx} \tag{4.27}$$

$$\epsilon_x^0 = \frac{du^0}{dx} \tag{4.28a}$$

$$\epsilon_y^0 = \frac{w^0}{R} \tag{4.28b}$$

$$\gamma_{xy}^0 = \frac{dv^0}{dx} \tag{4.28c}$$

$$\kappa_x = -\frac{d^2w^0}{dx^2} \tag{4.29a}$$

$$\kappa_y = -\frac{\mathrm{d}^2 w^0}{dx^2} \tag{4.29b}$$

$$\kappa_{xy} = -\frac{2}{R}\frac{dv^0}{dx} \tag{4.29c}$$

Chapter 8.2 of [43] provides specific details about the formulation of the results leading to the development of the equations of interest to describe the axial, circumferential, and radial displacements. The purpose of this section, however, is to provide a top-level overview of the process leading to this result. The equations of equilibrium, 4.23 through 4.27, strain-displacement, 4.28 through 4.29, and force-strain, 4.9, provide relationships for all the forces, moments, and displacements of the wall. Integration of the first two equilibrium equations leads to equations 4.30a and 4.30b, where D_1 and D_2 denote unknown constants. Substituting the force-strain relationship, 4.9 into 4.27a-b leads to equation 4.31. For convenience and simplicity of terms, the collection of matrices $[a_1]$ through $[a_4]$, [H], **g,** and elements f_1 through f_5 will be collected in table 4.2. The derivatives of $u^0$and v^0, which appear on the second element of equation 4.31 can then be expressed by 4.32; the internal forces N_y and M_y are then expressed as equation 4.33. Substituting the strain and curvature relationships, equations 4.28a through 4.29c, into 4.33 leads to equation 4.34. Additional substitution of equation 4.32 into 4.34 results in 4.35, which is then re-expressed as equations 4.36a-b.

$$D_1 = N_x \tag{4.30a}$$

$$D_2 = N_{xy} + \frac{M_{xy}}{R} \tag{4.30b}$$

$$\begin{Bmatrix} D_1 \\ D_2 \end{Bmatrix} = [a_2]\begin{Bmatrix} \frac{w^0}{R} \\ -\frac{\mathrm{d}^2 w^0}{dx^2} \end{Bmatrix} + [a_3]\begin{Bmatrix} \frac{du^0}{dx} \\ \frac{dv^0}{dx} \end{Bmatrix} \tag{4.31}$$

$$\begin{Bmatrix} \frac{du^0}{dx} \\ \frac{dv^0}{dx} \end{Bmatrix} = -[a_3]^{-1}[a_2]\begin{Bmatrix} \frac{w_0}{R} \\ -\frac{d^2 w^0}{dx^2} \end{Bmatrix} + [a_3]^{-1}\begin{Bmatrix} D_1 \\ D_2 \end{Bmatrix} \tag{4.32}$$

$$\begin{Bmatrix} N_y \\ M_x \end{Bmatrix} = \begin{bmatrix} A_{12} & A_{22} & A_{26} & B_{12} & B_{22} & B_{26} \\ B_{11} & B_{12} & B_{16} & D_{11} & D_{12} & D_{16} \end{bmatrix}\begin{Bmatrix} \epsilon_x^0 \\ \epsilon_y^0 \\ \gamma_{xy}^0 \\ \kappa_x \\ \kappa_y \\ \kappa_{xy} \end{Bmatrix} \tag{4.33}$$

$$\begin{Bmatrix} N_y \\ M_x \end{Bmatrix} = [a_1]\begin{Bmatrix} \frac{w^0}{R} \\ -\frac{\mathrm{d}^2 w^0}{dx^2} \end{Bmatrix} + [a_4]\begin{Bmatrix} \frac{du^0}{dx} \\ \frac{dv^0}{dx} \end{Bmatrix} \tag{4.34}$$

$$\begin{Bmatrix} N_y \\ M_x \end{Bmatrix} = [H]\begin{Bmatrix} \frac{w^0}{R} \\ -\frac{\mathrm{d}^2 w^0}{dx^2} \end{Bmatrix} + \begin{Bmatrix} g_1 \\ g_2 \end{Bmatrix} \tag{4.35}$$

$$N_y = H_{11}\frac{w^0}{R} - H_{12}\frac{d^2 w^0}{dx^2} + g_1 \tag{4.36a}$$

$$M_x = H_{21}\frac{w^0}{R} - H_{12}\frac{d^2 w^0}{dx^2} + g_2 \tag{4.36b}$$

Table 4.2 - Parameters required for equations 4.31 - 4.36b.

$$[\mathrm{a_1}] = \begin{bmatrix} A_{22} - \frac{B_{22}}{R} & B_{12} \\ B_{12} - \frac{D_{12}}{R} & D_{11} \end{bmatrix} \qquad [\mathrm{a_3}] = \begin{bmatrix} A_{11} & A_{16} - \frac{2B_{16}}{R} \\ A_{16} + \frac{B_{16}}{R} & A_{66} - \frac{B_{66}}{R} - \frac{2D_{66}}{R^2} \end{bmatrix}$$

$$[\mathrm{a_2}] = \begin{bmatrix} A_{12} - \frac{B_{12}}{R} & B_{11} \\ A_{26} - \frac{D_{26}}{R^2} & B_{16} + \frac{D_{16}}{R} \end{bmatrix} \qquad [\mathrm{a_4}] = \begin{bmatrix} A_{12} & A_{26} - \frac{2B_{26}}{R} \\ B_{11} & B_{16} - \frac{2D_{16}}{R} \end{bmatrix}$$

$$[\mathrm{H}] = \begin{bmatrix} H_{11} & H_{12} \\ H_{21} & H_{22} \end{bmatrix} = [a_1] - [a_4][a_3]^{-1}[a_2]$$

$$\mathbf{g} = \begin{Bmatrix} g_1 \\ g_2 \end{Bmatrix} = [a_4][a_3]^{-1} \begin{Bmatrix} D_1 \\ D_2 \end{Bmatrix}$$

$$\mathrm{f_1} = \mathrm{H_{22}} \qquad f_2 = -\frac{1}{R}(H_{21} + H_{12}) \qquad f_3 = \frac{H_{11}}{R^2} \qquad \mathrm{f_4} = \mathrm{P_{z_0}} - \frac{g_1}{R} \qquad \mathrm{f_5} = \mathrm{P_{z_1}}$$

Inserting equations 4.36a-b into 4.25 leads to equation 4.37. The solution to this equation yields the radial displacement of the reference surface, the first equation of interest, expressed by 4.38. The length of the cylinder is represented by L; λ and β denote the real and imaginary components of the roots of the characteristic polynomial, as expressed in equations 4.40a-b and 4.39. The constant $\mathrm{D_1}$ represents the membrane force component in the x-axis caused by the magnitude of the axial force $\widehat{N}$, as in equation 4.41. $\mathrm{D_2}$, expressed by 4.43, is obtained by inserting the total torque acting on the cylinder, 4.42, into 4.30b. Implementing the boundary conditions outlined by 4.44a-b, the constants $\mathrm{C_1} - \mathrm{C_4}$ leads to the equations summarized in 4.45. The terms $\mathrm{Y_{ij}}$ are summarized in table 4.3, for convenience.

$$f_1 \frac{d^4 w^0}{dx^4} + f_2 \frac{d^2 w^0}{dx^2} + f_3 w^0 = f_4 + x f_5 \tag{4.37}$$

$$\mathrm{w^0} = e^{-\lambda x}[C_1 \cos(\beta x) + C_2 \sin(\beta x)] + e^{-\lambda(L-x)}[C_3 \cos\big(\beta(L-x)\big) + C_4 \sin\big(\beta(L-x)\big)]\} + [\frac{1}{f_3}(f_4 + x f_5)] \tag{4.38}$$

$$\gamma = \sqrt{\frac{-f_2 + \sqrt{f_2^2 - 4 f_1 f_3}}{2 f_1}} \tag{4.39}$$

$$\lambda = \mathrm{Re}(\gamma) \tag{4.40a}$$

$$\beta = \mathrm{Im}(\gamma) \tag{4.40b}$$

$$\mathrm{D_1} = N_x = \frac{\widehat{N}}{2\pi R} \tag{4.41}$$

$$\widehat{T} = \big(N_{xy} R\big) 2\pi R + M_{xy} 2\pi R \tag{4.42}$$

$$\mathrm{D_2} = \frac{\widehat{T}}{2\pi R^2} \tag{4.43}$$

$$\mathrm{w^0} = 0 \qquad \frac{\mathrm{dw^0}}{dx} = 0 \qquad \text{at x = 0} \tag{4.44a}$$

$$w^0 = 0 \qquad \frac{dw^0}{dx} = 0 \qquad \text{at } x = L \tag{4.44b}$$

$$\begin{bmatrix} 1 & - & Y_{13} & Y_{14} \\ -\lambda & \beta & Y_{23} & Y_{24} \\ Y_{31} & Y_{32} & 1 & 0 \\ Y_{41} & Y_{42} & \lambda & \beta \end{bmatrix} \begin{Bmatrix} C_1 \\ C_2 \\ C_3 \\ C_4 \end{Bmatrix} = \begin{Bmatrix} \frac{f_4}{f_3} \\ \frac{f_5}{f_3} \\ \frac{f_4 + L f_5}{f_3} \\ \frac{f_5}{f_3} \end{Bmatrix} \tag{4.45}$$

Table 4.3 - Parameters in equation 4.45.

$Y_{13} = e^{-\lambda L}\cos\beta L$	$Y_{14} = e^{-\lambda L}\sin\beta L$
$Y_{23} = e^{-\lambda L}(\lambda\cos\beta L + \beta\sin\beta L)$	$Y_{24} = e^{-\lambda L}(-\beta\cos\beta L + \lambda\sin\beta L)$
$Y_{31} = e^{-\lambda L}\cos\beta L$	$Y_{32} = e^{-\lambda L} sin\,\beta L$
$Y_{41} = -e^{-\lambda L}(\lambda\cos\beta L + \beta\sin\beta L)$	$Y_{42} = e^{-\lambda L}(\beta\cos\beta L - \lambda\sin\beta L)$

Finally, integrating expressions 4.32 leads to the axial and circumferential displacements, expressed by equation 4.46. These are the additional two properties of interest for this analysis. The corresponding terms in this equation, namely the derivates and integral of w^0, are summarized in table 4.4, included below. The terms u_0^0 and v_0^0 denote the rigid-body motions, which will be neglected in this analysis. The strains can then be calculated by using equation 4.28a – 4.29c.

$$\begin{Bmatrix} u^0 \\ v^0 \end{Bmatrix} = -[a_3]^{-1}[a_2] \begin{Bmatrix} \frac{\int w^0 dx}{R} \\ -\frac{dw^0}{dx} \end{Bmatrix} + x[a_3]^{-1} \begin{Bmatrix} D_1 \\ D_2 \end{Bmatrix} + \begin{Bmatrix} u_0^0 \\ v_0^0 \end{Bmatrix} \tag{4.46}$$

Table 4.4 - Parameters in equation 4.46.

$$w^0 = \frac{1}{f_3}(f_4 + x f_5) + e^{-\lambda x}\cos(\beta x)\,C_1 + e^{-\lambda x}\sin(\beta x)\,C_2 + e^{-\lambda(L-x)}\cos(\beta(L-x))\,C_3 + e^{-\lambda(L-x)}\sin(\beta(L-x))\,C_4$$

$$\frac{dw^0}{dx} = \frac{f_5}{f_3} + e^{-\lambda x}\cos(\beta x)\,(-\lambda C_1 + \beta C_2) + e^{-\lambda x}\sin(\beta x)\,(-\beta C_1 - \lambda C_2) + e^{-\lambda(L-x)}\cos\big(\beta(L-x)\big)\,(\lambda C_3 - \beta C_4) + e^{-\lambda(L-x)}\sin(\beta(L-x))\,(\beta C_3 - \lambda C_4)$$

$$\int w^0 dx = \frac{1}{f_3}\left(f_{4x} + \frac{x^2}{2} f_5\right) + e^{-\lambda x}\cos(\beta x)\frac{-\lambda C_1 - \beta C_2}{\lambda^2+\beta^2} + e^{-\lambda x}\sin(\beta x)\frac{\beta C_1 - \lambda C_2}{\lambda^2+\beta^2} + e^{-\lambda x}\cos(\beta(L-x))\frac{\lambda C_3 - \beta C_4}{\lambda^2+\beta^2} + e^{-\lambda x}\sin(\beta(L-x))\frac{\beta C_3 - \lambda C_4}{\lambda^2+\beta^2}$$

4.1.3 Membrane Theory: Prediction of Critical Buckling Load

This analysis starts by considering a composite shell subjected to surface loads on the wall and compressive and shear loads at the edges. Once this set of applied loads becomes larger than a critical limit, the shell buckles, either locally or globally. For a small shell element exposed to these loads, as the one in in figure 4.4a, the corresponding membrane forces acting on it can be visualized in figure 4.4b. These relationships are expressed by equations 4.46a – 4.46c. The load parameter is denoted by λ, which for some value causes local bucking and becomes λ_{cr}. As mentioned in the previous section, the derivation leading to these results is reserved to chapter 8.4 of [43], but key results are outlined in this sub-section. First, in the region where the local buckling occurs, the shell has constant curvatures, as expressed by equations 4.47a-c, and the reference surface can be described in terms of two variables, as shown by 4.48. Various curvatures of typical shells can be observed in figure 4.5 [43]. The radii of curvatures can then be expressed by 4.49a-c. Implementing these assumptions, equation 4.50 can be formulated. The in-plane and out-of-plane amplitude of the buckling waves are represented by u_1, v_1, u_2, v_2, and w_1, and w_2, respectively. These wavelengths are assumed to be short. For convenience, the matrices [O], [L], [J], and the parameters Φ_1 and Φ_2 are grouped in table 4.5.

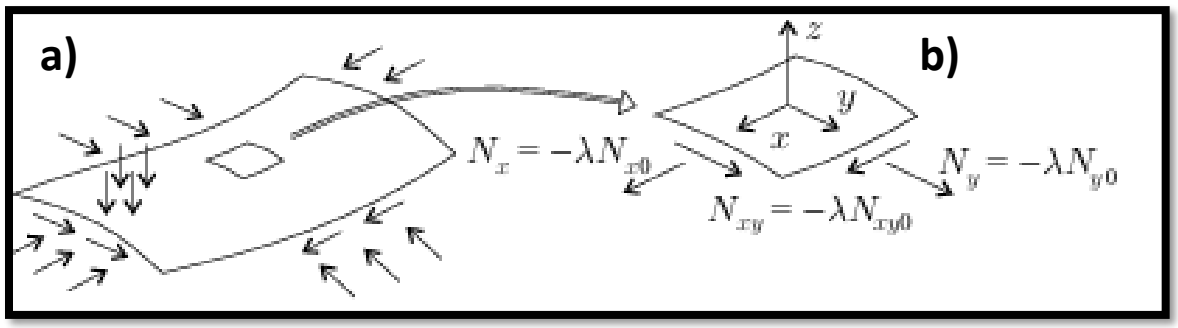

Figure 4.4 – a) Applied loads on the shell and the membrane forces. b) Membrane forces acting on the shell element [43].

$$N_x = -\lambda N_{x0} \quad (4.46a)$$
$$N_y = -\lambda N_{y0} \quad (4.46b)$$
$$N_{xy} = -\lambda N_{xy0} \quad (4.46c)$$
$$R_x = constant \quad (4.47a)$$
$$R_y = constant \quad (4.47b)$$
$$R_z = constant \quad (4.47c)$$
$$f(x, y) = S \quad (4.48)$$
$$\frac{1}{R_x} = -\frac{\partial^2 f}{\partial x^2} \quad (4.49a)$$
$$\frac{1}{R_y} = -\frac{\partial^2 f}{\partial y^2} \quad (4.49b)$$
$$\frac{1}{R_{xy}} = -\frac{2\partial^2 f}{\partial x \partial y} \quad (4.49c)$$

$$\left(\begin{bmatrix} O & L \\ L & O \end{bmatrix}\begin{bmatrix} M_o & M_n \\ M_n & M_o \end{bmatrix}\begin{bmatrix} O & L \\ L & O \end{bmatrix}^T - \lambda\begin{bmatrix} \Phi_1[\mathrm{J}] & \Phi_2[\mathrm{J}] \\ \Phi_2[\mathrm{J}] & \Phi_1[\mathrm{J}] \end{bmatrix}\right)\begin{Bmatrix} u_1 \\ v_1 \\ w_1 \\ u_2 \\ v_2 \\ w_2 \end{Bmatrix} = 0 \tag{4.50}$$

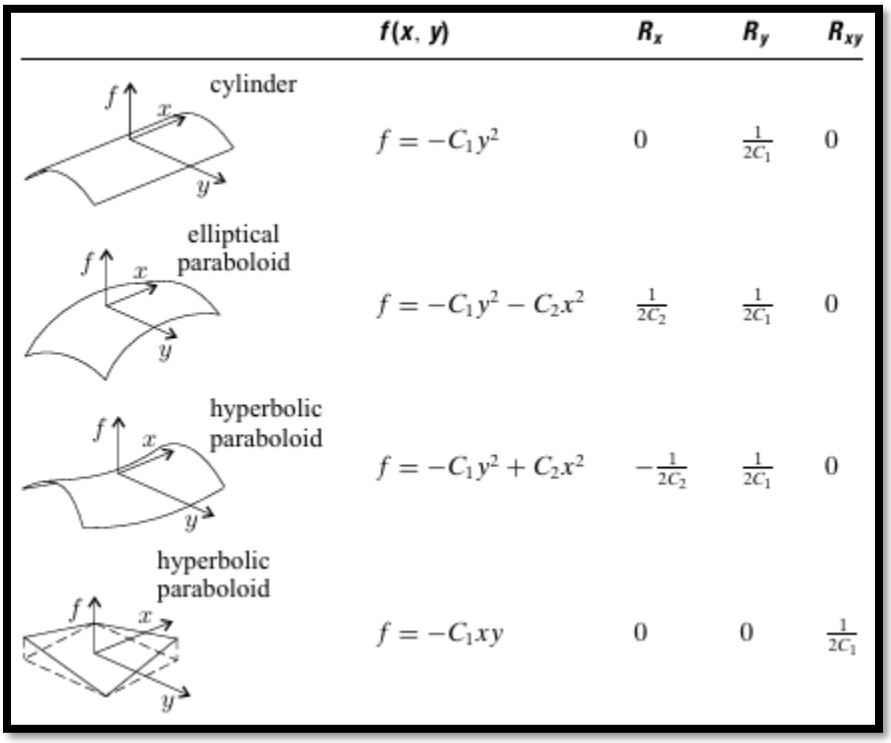

Figure 4.5 – Various curvatures of typical shells [43].

Table 4.5 - Parameters in equation 4.50.

$$[O] = \begin{bmatrix} -\alpha & 0 & \beta & 0 & 0 & 0 \\ 0 & -\beta & \alpha & 0 & 0 & 0 \\ \frac{1}{R_x} & \frac{1}{R_y} & 0 & \alpha^2 + \beta^2 c_2^2 & \beta^2 + \alpha^2 c_1^2 & -2\alpha\beta(1 + c_1 c_2) \end{bmatrix}$$

$$[L] = \begin{bmatrix} \beta c_2 & 0 & -\alpha c_1 & 0 & 0 & 0 \\ 0 & \alpha c_1 & -\beta c_2 & 0 & 0 & 0 \\ 0 & 0 & \frac{1}{R_{xy}} & -2\alpha\beta c_2 & -2\alpha\beta c_1 & 2(c_1\alpha^2 + c_2\beta^2 \end{bmatrix}$$

$$[M_o] = \begin{bmatrix} A_{11} & A_{12} & 0 & B_{11} & B_{12} & 0 \\ A_{12} & A_{22} & 0 & B_{12} & B_{22} & 0 \\ 0 & 0 & A_{66} & 0 & 0 & B_{66} \\ B_{11} & B_{12} & 0 & D_{11} & D_{12} & 0 \\ B_{12} & B_{22} & 0 & D_{12} & D_{22} & 0 \\ 0 & 0 & B_{66} & 0 & 0 & D_{66} \end{bmatrix}$$

$$[M_n] = \begin{bmatrix} A & B \\ B & D \end{bmatrix} - [M_o]$$

$$[J] = \begin{bmatrix} 0 & 0 & 0 \\ 0 & 0 & 0 \\ 0 & 0 & 1 \end{bmatrix}$$

$$\Phi_1 = N_{x0} = (\alpha^2 + \beta^2 c_2^2) + N_{xy0} 2(\alpha^2 c_1 + \beta^2 c_2^2) + N_{y0}(\alpha^2 c_1 + \beta^2)$$

$$\Phi_2 = -2\alpha\beta(N_{x0} c_2 + N_{xy0}(1 + c_1 c_2) + N_{y0} c_1)$$

Notably, among the parameters required to solve equation 4.50 are four constants: $\alpha, \beta, c_1,$ and c_2. These values describe the wave pattern of the buckled wave; an instance of buckling pattern of a shell is shown in figure 4.6. Determining the eigenvalues presented by equation 4.50 correspond to the critical load parameters of interest, namely λ_{cr}. The finite, lowest value, greater than zero, will be the solution of interest for the set of selected four constants. For short wavelengths, consistent with the assumption made in the previous paragraph, real, positive, and arbitrary values can be used to determine the critical buckling load.

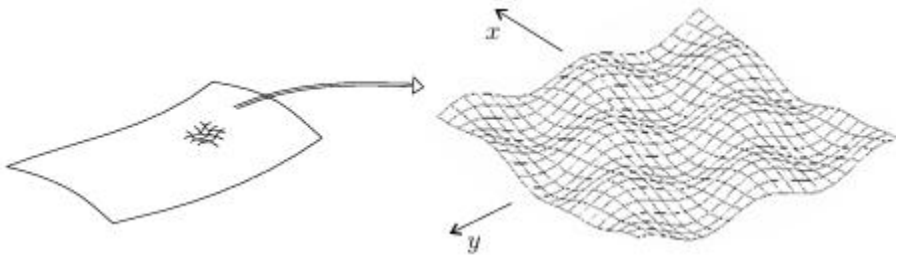

Figure 4.6 – Visualization of local buckling pattern.

4.2 Laminate Model, Material Properties and Loading Conditions

While no peer-reviewed study has corroborated the laminate composition of the Titan Submersible, an available online source [44] cited the ply layout to be composed of 667 plies, alternatingly aligned in the axial and circumferential direction. In other words, this stacking sequence can be represented as follows: $[(0, 90)_{333s}\ 0]$. It also identified the matrix and fiber constituents to be Grafil 37-800 30K and Epoxy Resin 862. The mechanical properties of the resin are highly dependent on the curing agent. Some of these chemicals can be Diethyltoluenediamine (DETDA) epoxy curing agent and EPIKURE ™ Anhydride-based curing agent. In this stage of the study, mechanical properties for the fiber and matrix were obtained from [43] and are outlined in table 4.6, located below. As signaled in the fourth paragraph of subsection 4.1.1, *the rules of mixture* for composite materials were then used to determine the final mechanical properties of interest: Young's Modulus in the longitudinal, E_1, and transverse directions, E_2, the longitudinal shear modulus, G_{12}, and the longitudinal Poisson's ratio ν_{12} for a reference ply, oriented at a 0-degree angle. The derivation of these properties can be found in chapter 11 of [43], and the series of equations to model these properties are summarized by 4.51 to 4.54. With these quantities, the reduced stiffness coefficient matrix, Q, can then be formulated, as expressed by equation 4.16, shown below again for convenience to the reader.

$$E_1 = E_{f_1} V_f + E_m(1 - V_f) \tag{4.51}$$

$$\mathrm{E_2} = \left(\frac{\mathrm{V_f}}{\mathrm{E_{f_1}}} + \frac{1-V_f}{E_m}\right)^{-1} \tag{4.52}$$

$$\mathrm{G_{12}} = \left(\frac{\mathrm{V_f}}{\mathrm{G_{f_{12}}}} + \frac{1-V_f}{G_m}\right)^{-1} \tag{4.53}$$

$$\nu_{12} = \nu_{f_{12}} V_f + \nu_m(1 - V_f) \tag{4.54}$$

$$[\mathrm{Q}] = \begin{bmatrix} \frac{E_1}{D} & \frac{\nu_{12}E_2}{D} & 0 \\ \frac{\nu_{12}E_2}{D} & \frac{E_2}{D} & 0 \\ 0 & 0 & G_{12} \end{bmatrix} \tag{4.16}$$

$$D = 1 - \frac{E_2}{E_1}\nu_{12}^2 \tag{4.17}$$

Table 4.6 - Mechanical properties of matrix constituents [43].

Material	Property	Symbol	Units	Value
Grafil 37-800 (30k TOW)	Longitudinal Young's Modulus	E_{f_1}	GPa	231
	Longitudinal Shear Modulus	$G_{f_{12}}$	GPa	91
	Longitudinal Poisson's Ratio	$\nu_{f_{12}}$	-	0.27
	Volume Fiber Fraction	V_f	-	0.7
Epon Resin 862	Matrix Young's Modulus	E_m	GPa	2.8
	Matrix Shear Modulus	G_m	GPa	1
	Matrix Poisson's Ratio	ν_m	-	0.35

As previously identified, the pressure at the maximum operational depth of the Titan, 4 km under the surface of the ocean, corresponds to 40.33 MPa. To determine the axial load, the cross-sectional area of the cylindrical had to be considered, as visualized in figure 4.7. The inner radius of the cylinder and its thickness are denoted by r_i and h, and these values are 70.11cm and 12.7cm, respectively. Since the pressure can be expressed by equation 4.55, solving for the force leads to 4.56. The cross-sectional area is then determined by 4.57, for which the corresponding magnitude of the axial force is found to be $24.606 * 10^6$N. Following the convention established by figure 4.3a, a compressive force is negative. Table 4.7 summarizes the loading conditions implemented to generate the displacements of interest.

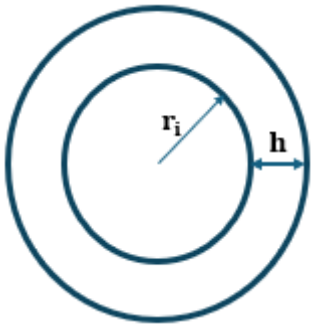

Figure 4.7 – Cross-sectional view of the cylindrical section.

$$P = \frac{F}{A_{cross\ section}} \quad (4.55)$$

$$\mathrm{F_{axial}} = P * A_{cross\ section} \quad (4.56)$$

$$\mathrm{A_{cross-section}} = \pi(r_{outer}^2 - r_{inner}^2) \quad (4.57)$$

$$\mathrm{F_{axial}} = 24.606 * 10^6 N \quad (4.58)$$

Table 4.7 - Implemented loading conditions.

Loading Condition	Units	Value
Constant Pressure	MPa	40.33
Axial Load	N	-24.606 x10^6
Torque	N*m	0

4.3 Algorithm Workflow and Implementation in MATLAB ®

The two algorithms developed by the author to predict the buckling load and displacements of interest can be found in sections 2 and 3 of the appendix. Although the series of equations used to generate the properties of interest were discussed in chapters 4.1 through 4.2, the purpose of this subsection is to provide a visualization of this process to the reader. At this stage of the investigation, interested readers can perform customized calculations by copy-pasting these scripts into MATLAB and modifying the loading conditions, geometry, and laminate stacking sequence. Once this is completed, results will be generated and stored accordingly. Comments have been added to guide the reader in understanding the units, significance of the variables, and calculation at hand.

The first section of the algorithm determines and plots the axial, circumferential, and radial displacements. It achieves this objective by first gathering a series of inputs; these are the cylinder geometry and loading conditions, ply layout, and mechanical properties of the fiber and matrix. Consequently, the calculation of the engineering constants are performed to populate the reduced stiffness matrix. With this information, the ABD matrix can be assembled. Along with the cylinder geometry and loading conditions, the characteristic polynomial equation 4.39 can be built and its roots solved. Once these values are known, the elements of equation 4.45 can be developed to then invert the matrix and find the values of the constants in matrix "C". After these computations are completed, the axial, radial, and circumferential displacements can then be determined. This process can be better visualized in figure 4.8.

Figure 4.9 describes the process followed in the script to investigate the buckling load. Similar to the previous script, the ply layout and mechanical properties of the fiber and matrix are half of the required inputs. The cylinder geometry and an array of positive and arbitrary values for four constants, α, β, c_1, and c_2 represent the second half. With this information, the engineering constants are calculated and the reduced stiffness matrix then assembled. After the ABD matrix is developed, the second half of the inputs is used to develop the matrices M_0, M_n, and J; consequentlty, the matrices OL, G, Φ_1 and Φ_2 are assembled for each corresponding possible combination of the four inputted constants. The eigenvalues are determined and stored for each iteration. Finally, the lowest, finite, and positive eigenvalue is selected, along with the constants used to achieve this, for reference. This value corresponds to the solution of interest, the critical buckling load.

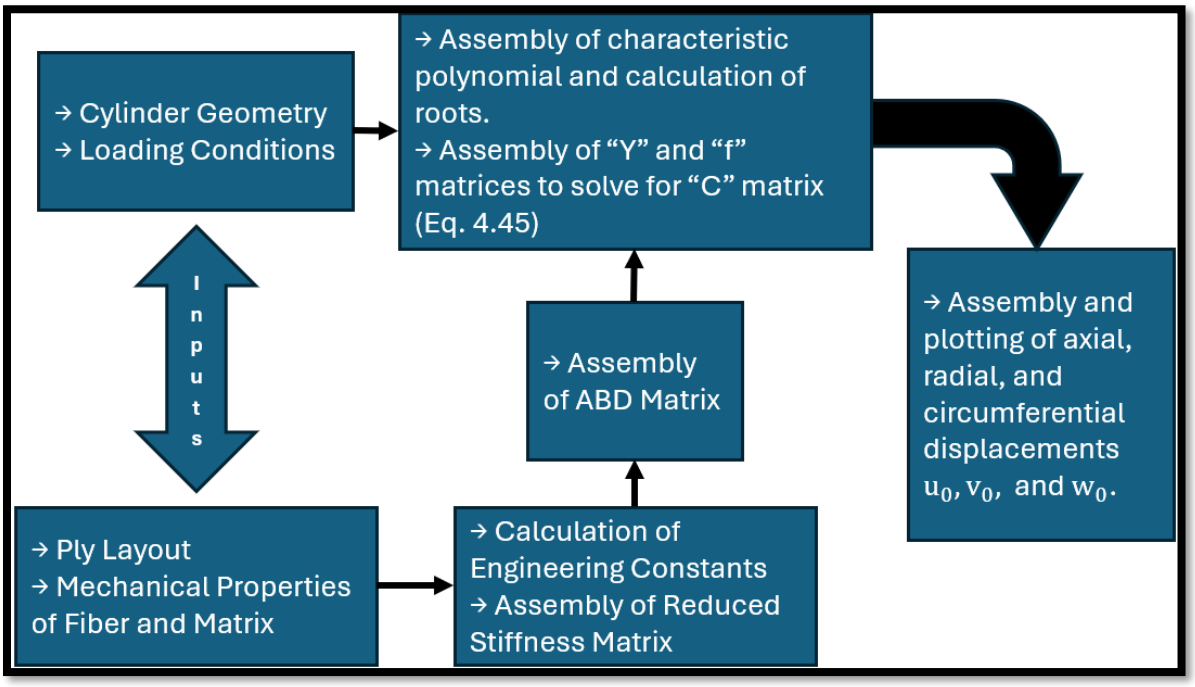

Figure 4.8 – Workflow of MATLAB® script to find the displacements.

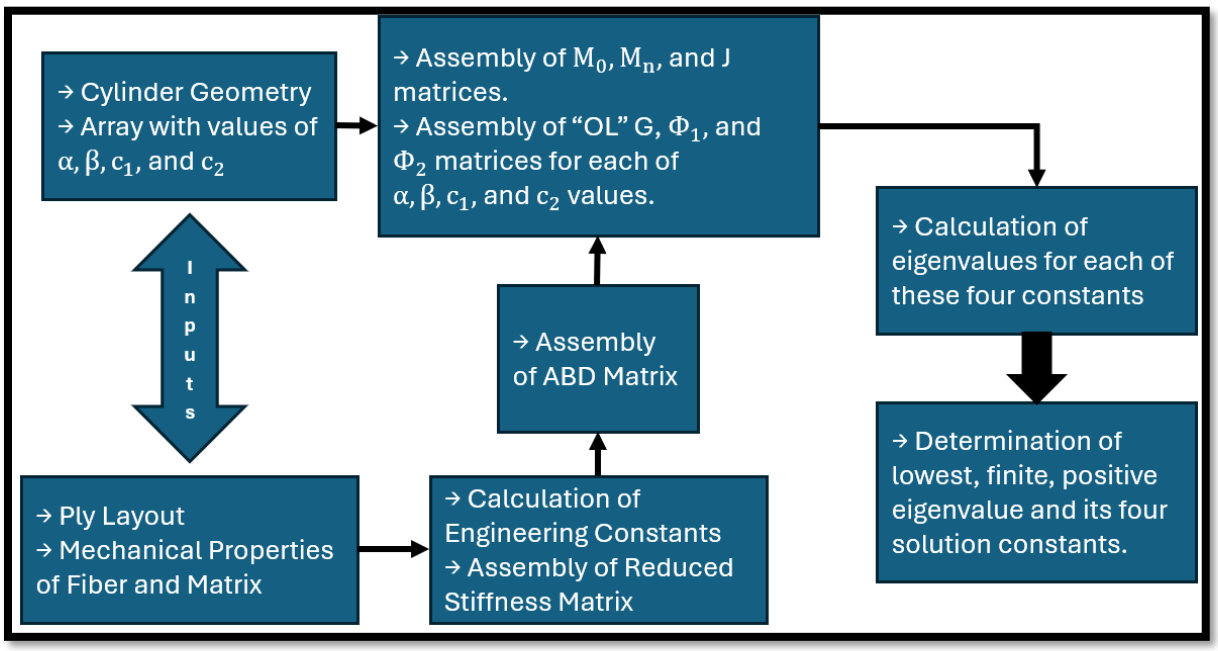

Figure 4.9 – Workflow of MATLAB® script to find the buckling load.

4.4 Results and Discussion

4.4.1 Critical Buckling Load

Although the author decided to first introduce the theory behind the calculation of displacements in subsection 4.1.1, the first calculation performed to assess the results was the critical buckling load. If the determined buckling load was very close to the applied axial load, the displacements would be expected to be excessively large and exceed the fundamental assumptions under classical laminate theory (CLT): small displacements are allowed only. In other words, if the applied load neared 2 or 3 times the critical buckling load, CLT could not be soundly used to predict the displacements, since the development of shell theory uses the CLT underlying assumptions. The values of the four positive, arbitrary constants required to determine the critical buckling load are summarized in table 4.8. The computed critical buckling load was found to be $292.7866481 * 10^6$ N; figure 4.10 is a screen capture once the calculations were executed with MATLAB ®. This value is 11.9 times larger than the maximum operational axial load, at the lowest sea depth, corresponding to $24.606 * 10^6$ N. As a result, the displacements are anticipated to be acceptably small, and shell theory suitable for the prediction of the displacements.

Table 4.8 - Positive, arbitrary constants used in the calculation of the buckling load.

Constant	Minimum Value	Maximum Value	Total Elements
$\boldsymbol{\alpha}$	1	50	100
$\boldsymbol{\beta}$	1	50	100
$\boldsymbol{c_1}$	0	2	21
$\boldsymbol{c_2}$	0	2	21

```
Minimum finite la: 292786648.098516
Occurs at: al = 21.29, be = 21.29, c1 = 0.90, c2 = 0.90
```

Figure 4.10 – Calculated critical buckling load and its corresponding four constants.

4.4.2 Displacements: Axial, Radial, and Circumferential

Figures 4.11 through 4.13 show the predicted axial u_0, circumferential v_0, and radial w_0 displacements. Conventionally, for applications not related to the depths of the ocean, the magnitude of the displacements is typically in the range of the micro-meters ($1 * 10^{-6}$). The first observation from these results is that the magnitude of the displacement is in the millimeters $1 * 10^{-3}$. Most intuitively, since the cylinder is compressed by the axial load applied at its edges, the radial displacements are positive and symmetrical throughout the axial distance of the cylinder, graphed in the vertical axis for all figures. In other words, the material constituents displace away from the axis of symmetry of the cylinder, by as much as 2.26mm. The thickness of a single US dime measures 1.35mm [45]; consequently, the displacement of the material constituents is less than that of two piled 10-cent coins. Although this might seem excessive, given the colossal operational pressure, 40.33MPA, it is expected that this material geometry experiences such displacement under this operating conditions. Similarly, the most drastic axial and circumferential displacements approach the magnitude of 2.5mm. Since the theory assumes that the displacements

are not accurate at the edges, this value is taken as a reasonable approximation. Unlike the radial displacements, these two do not show a symmetrical variation, across the axial distance of the cylinder, as is expected. This set of values will be used as a comparison for the FEM solution, discussed in the next chapter.

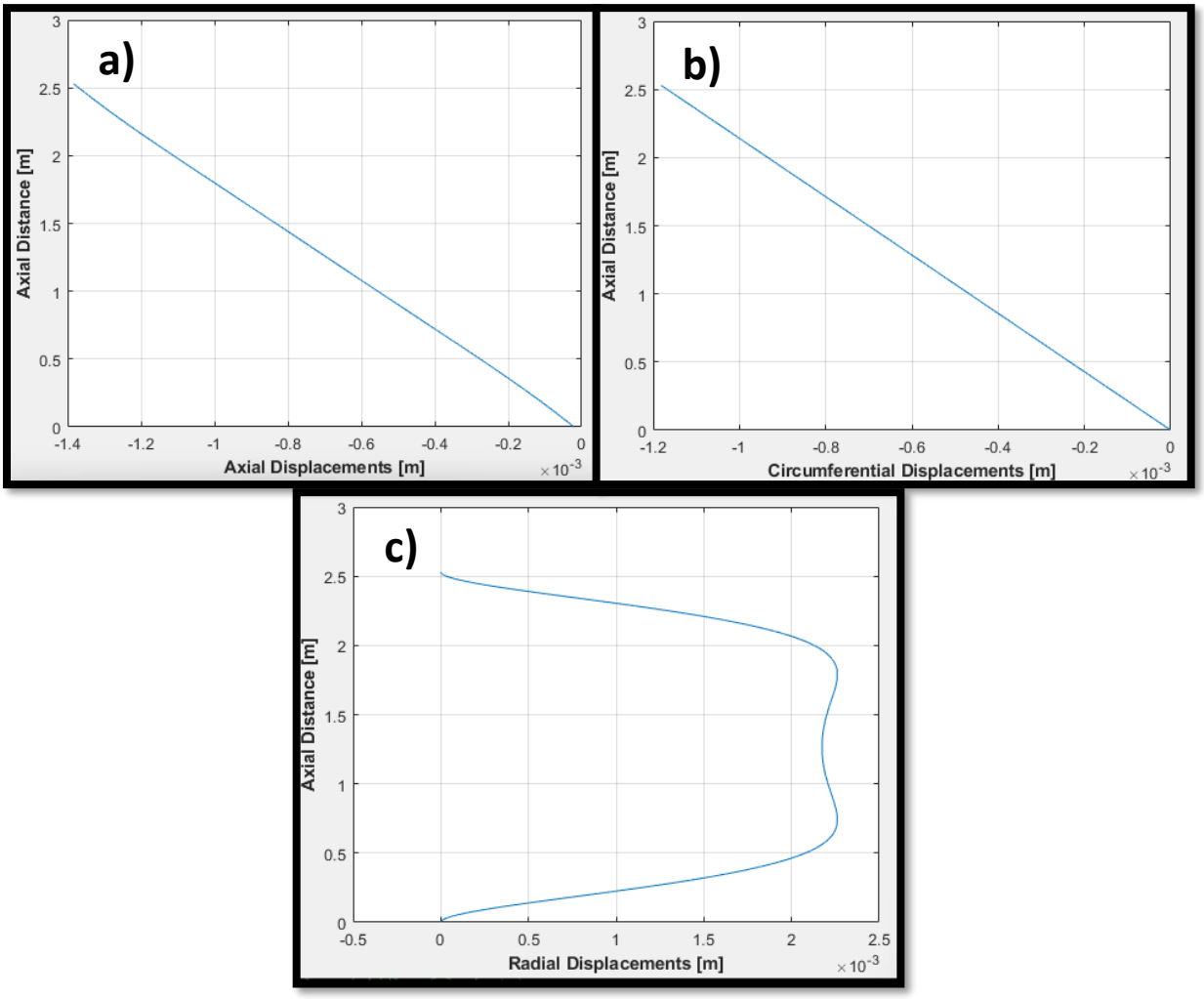

Figure 4.11 – a) Axial, b) Circumferential, and c) Radial displacements.

5. Execution of FEA in Ansys

5.1 General Overview

After the rapid analysis of the cylindrical CFRE section was conducted, as explained in chapter 4, Ansys Static Structural was then used to develop a numerical solution through the FEM. The implemented modeling strategy consisted of gathering the corresponding material properties, discretizing the geometry model, applying boundary conditions and loads, evaluating results, and making corrections as required. This process is shown in figure 5.1. Work presented in this section includes the upper-half of the diagram, as results will be discussed in section 6.

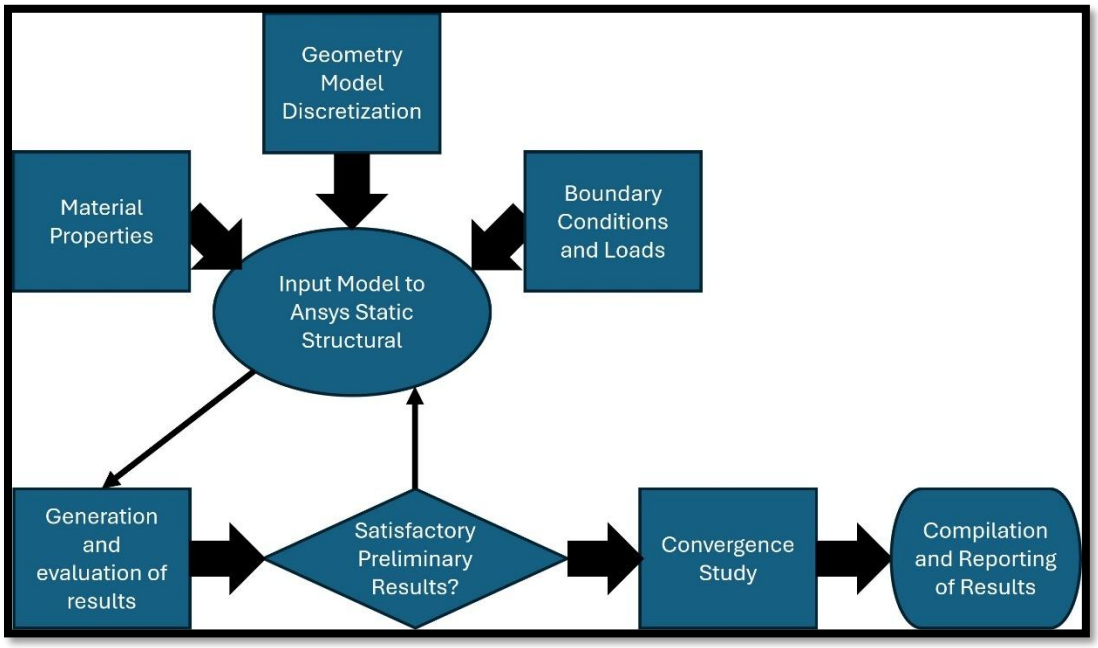

Figure 5.1 – Problem modeling approach in Ansys Static Structural.

5.2 Geometry Model

5.2.1 Material Assignment and Properties

Three materials were identified during the early research stages of this project and outlined in section 1.2. These were: Titanium Grade 3, Polymethyl Methacrylate (PMMA) and Carbon Fiber Reinforced Epoxy (CFRE). The material assignment is summarized in table 5.1. For convenience to the reader, the Titan Submersible drawing, labeled previously as Figure 3.26, is juxtaposed, as shown in the third column of the table.

Table 5.1 - Material assignment of the submersible's components.

Component	Material Assignment
Observation Window	PMMA
Bow and Stern	Titanium Grade 3
Interface O-Rings	
Cylindrical Section	CFRE

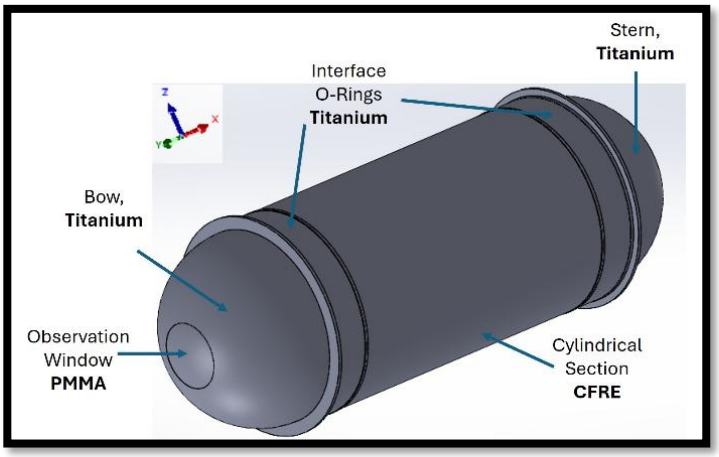

Material properties are highly dependent on the manufacturing process, which may vary by company. Manufacturing company A, for example, may have treatment processes that yield a higher level of purity while minimizing voids and porosity, as compared to company B. These factors will ultimately influence the mechanical properties of the processed material. As a result, without knowledge of the actual material properties used in the design of the submersible, the best reasonable approximation can be made by employing "average" properties from available sources. Three resources were consulted to obtain the mechanical properties of the Titan Submersible. For Titanium Grade 3, ASM Aerospace Specification Metals Inc. website [46] was consulted. In the case of PMMA, a similar study found in the literature review [27] contained all the properties of interest. Lastly, to obtain the properties of CFRE, the rules of mixture were used, employing the typical material properties for Carbon Fiber and Epoxy, as included in [43]. All the properties of interest are summarized in tables 5.2 through 5.4. To assess the soundness of these values, similar values obtained from the Ansys' material library were compared and are reflected in the third column of each corresponding table. The used values, reflected in column 4, were subsequently updated in the Ansys's material library.

Table 5.2 - Material properties of titanium.

Property	Unit	Value		Note and Source
		Ansys Titanium Alloy	Used	
Density	kg/m^3	4620	4500	[46]
Youngs Modulus	Pa	9.60E+10	1.05E+11	
Poisson's Ratio	-	0.36	0.37	
Tensile Yield Strength	Pa	9.30E+08	4.49E+08	
Compressive Yield Strength	Pa	9.30E+08	4.50E+08	
Tensile Ultimate Strength	Pa	1.07E+09	1.00E+09	

Table 5.3 - Material properties of PMMA.

Property	Unit	Value		Note and Source
		Ansys Granite Library	Used	
Density	kg/m^3	1200	1190	[27]
Youngs Modulus	Pa	3.00E+09	2.74E+09	
Poisson's Ratio	-	-	0.38	
Tensile Yield Strength	Pa	6.40E+07	1.15E+08	
Compressive Yield Strength	Pa	6.40E+07	1.15E+08	
Tensile Ultimate Strength	Pa	6.30E+10	-	

Table 5.4 - Material properties of CFRE laminate.

Property		Unit	Value		Note and Source
			Ansys Epoxy Carbon UD 365GP Prepreg	Used	
Density		kg/m^3	1540	1600	Typical Ply Property Graphite T300/Epoxy [43], p. 486
Young's Modulus	x-direction	Pa	2.09E+11	1.63E+11	Rules of Mixture Calculation
	y-direction		9.45E+09	9.08E+09	
	z-direction		9.45E+09	9.08E+09	
Poisson's Ratio	xy plane	-	0.27	0.294	
	yz plane		0.4	0.59	
	xz plane		0.27	0.294	
Shear Modulus	xy plane	Pa	5.50E+09	3.25E+09	
	yz plane		3.90E+09	2.85E+09	
	xz plane		5.50E+09	3.25E+09	
Orthotropic Stress Limit - Tensile	x-direction	Pa	1.98E+09	1.50E+09	Typical Ply Property Graphite T300/Epoxy [43], p. 486
	y-direction		2.60E+07	4.00E+07	
	z-direction		2.60E+07	4.00E+07	
	x-direction	Pa	-8.93E+08	-1.50E+09	

Orthotropic Stress Limit - Compressive	y-direction		-1.39E+08	-2.46E+08	
	z-direction		-1.39E+08	-2.46E+08	
Orthotropic Stress Limit - Shear	xy plane	Pa	1.00E+08	6.80E+07	[43], p. 486
	yz plane		5.00E+07	3.40E+07	Assumed 50% of orthotropic Stress Limit xy plane
	xz plane		1.00E+08	6.80E+07	Typical Ply Property Graphite T300/Epoxy [43], p. 486
Orthotropic Strain Limit - Tensile	x-direction	-	0.0095	0.00947	Calculated
	y-direction		0.0028	0.00275	
	z-direction		0.0028	0.00275	
Orthotropic Strain Limit - Compressive	x-direction		-0.0043	-0.00427	
	y-direction		-0.0147	-0.01471	
	z-direction		-0.0147	-0.01471	
Orthotropic Strain Limit - Shear	xy plane		0.0182	0.01818	
	yz plane		0.0128	0.01282	
	xz plane		0.0182	0.01818	

5.2.2 Laminate Modeling Technique

As previously signaled, Ansys Composites PrePost (ACP) is the simulation tool to develop composite structures. In the analytical approach outlined in chapter 4.2, the laminate was identified to be composed of 667 alternatingly aligned in the longitudinal and circumferential directions: $[\,[0, 90]_{333s}, 0]$. To represent this topology in ACP, the thickness per ply was first determined by dividing the thickness of the cylindrical section, $h_{cylinder}$, by the number of plies, n_{plies}, as reflected in equation 5.1. The corresponding thickness per ply was determined to be 0.1904mm. Consequently, the 667 plies and their corresponding orientation were created. This implementation can be visualized in figure 5.2. As intended, ACP calculated the total laminate thickness to be 0.127m; this can be observed at the bottom of figure 5.2 b). This process enabled the cylindrical section to be represented and a shell, for a subsequent import to Ansys Static Structural, where the meshing, boundary, and loading conditions are defined, as will be explained in the two proceeding subsections.

$$t_{ply} = \frac{h_{cylinder}}{n_{plies}} \tag{5.1}$$

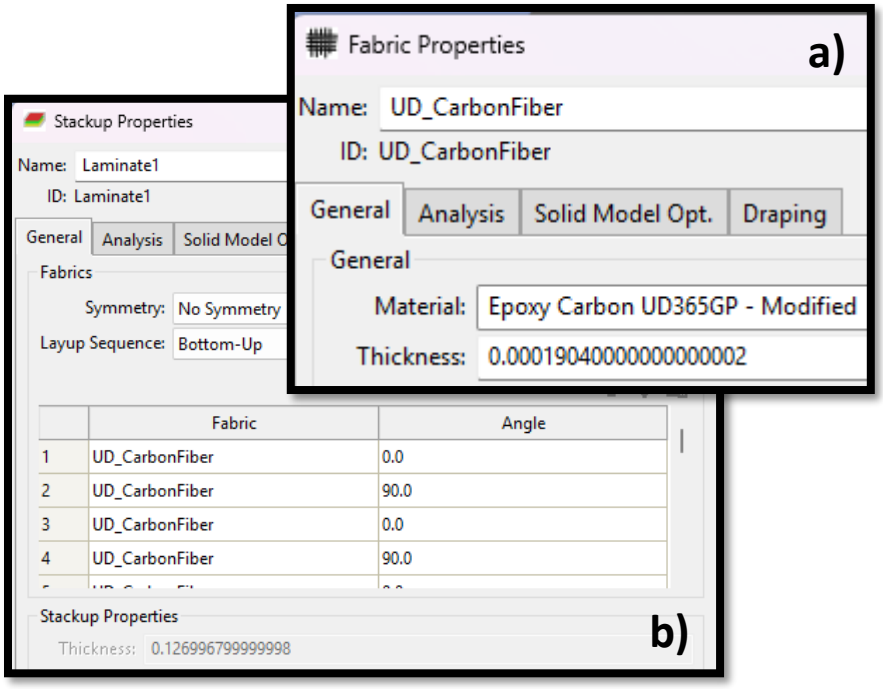

Figure 5.2 – a) Assignment of ply thickness and b) Creation of laminate with 667 plies.

Using this same module within ACP, once the laminate has been created, the ABD matrix can be generated. A comparison between the ABD matrix generated by Ansys and the analytical approach implemented with MATLAB is shown in figure 5.3. An acceptable agreement is observed across the A and D matrices. Non-zero elements appear to differ by less than 1%. Elements reflected as 0 in the analytical calculations, such as the first two elements in the last row of the A matrix, appear to approach zero; these values, for example, are 2.2713e-10 and 6.0023e-7. According to the Classical Laminate Theory, the values of the B matrix in a symmetric laminate are 0. The small-valued elements reflected in the last 3 rows and last 3 columns, pertaining to the B matrix calculated by Ansys, are observed to also approach zero. In the analytical approach, these values are automatically assigned as 0 if the laminate is symmetric. Lastly, the corresponding ply orientation was visually checked to ensure that the intended orientation was correctly assigned. The odd-numbered plies were oriented in the longitudinal direction while the even-numbered counterparts were positioned in the circumferential direction, as shown in figure 5.4.

a)

i	0	1	2	3	4	5
0	1.0994e+10	3.4066e+08	2.2713e-10	1.1561e-05	3.5415e-07	2.4448e-25
1	3.4066e+08	1.0965e+10	6.0023e-07	3.5415e-07	1.1644e-05	6.443e-22
2	2.2713e-10	6.0023e-07	4.1274e+08	2.4259e-25	6.443e-22	4.3737e-07
3	1.1561e-05	3.5415e-07	2.4448e-25	1.4816e+07	4.5785e+05	3.0435e-13
4	3.5415e-07	1.1644e-05	6.443e-22	4.5785e+05	1.4697e+07	8.043e-10
5	2.4259e-25	6.443e-22	4.3737e-07	3.0435e-13	8.043e-10	5.5473e+05

Stiffness Matrix:

ABD

6x6 double

b)

	1	2	3	4	5	6
1	1.0965e+10	3.4055e+08	0	0	0	0
2	3.4055e+08	1.0936e+10	0	0	0	0
3	0	0	4.1275e+08	0	0	0
4	0	0	0	1.4778e+07	4.5773e+05	0
5	0	0	0	4.5773e+05	1.4659e+07	0
6	0	0	0	0	0	5.5477e+05

Figure 5.3 – ABD matrix determined by a) Ansys and b) Analytical Approach in MATLAB ®.

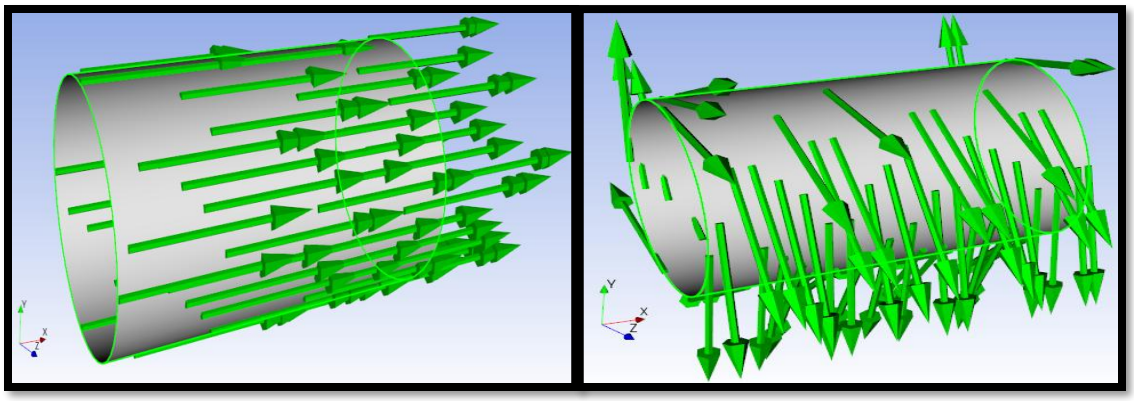

Figure 5.4 – Longitudinal and circumferential ply assignment in ACP.

5.3 Geometry Model Discretization

While geometry discretization precedes laminate model creation in the Ansys workflow, the author opted to discuss laminate development alongside material characteristics, as seen in Section 5.2. The intent of this approach was to ensure that readers can first assess the mechanical properties of both isotropic and orthotropic materials (composite structure) before addressing FEA domain discretization.

The geometry model was discretized in terms of a three gradual augmentation of elements. In other words, three meshes with incremental number of elements were developed: coarse, medium, and fine. Increasing the number of nodes in a domain is a technique referred by Cook et al [32] as a "weak patch test" to identify numerical convergence in a FEM solution. Creating a mesh using a computational tool is an iterative process, during which a combination of various methods, element sizes, and controls must be tested to generate a successful mesh. Once this is achieved, additional refinements and modifications are then tested to produce the greatest number of good-quality elements. Given the "regular" geometry of the submersible, three main types of meshing methods were used: tetrahedrons, sweep, quadrilateral dominant, and automatic. As the name implies, the tetrahedron method employs tetrahedron elements in areas with curved and irregular topologies. This was implemented for the observation window. In contrast, the sweep method is used for more regular shapes, such as the base of the bow and stern, the "body" of the connecting O-Rings, which are cylindrical. The quadrilateral dominant method is similar to sweep but it is recommended for shell models; as a result, it was implemented in the cylindrical section. Lastly, in automatic meshing method, Ansys selects the best meshing method based on the topology at hand. Primary elements can include a combination of tetrahedral and hexahedral elements, for example. This method was used in the spherical sections: the bow and the stern. The specific method and sizing by mesh resolution is summarized in table 5.5. The discussion of the last column, whose element size is "ideal" is deferred to the next paragraph.

Table 5.5 - Meshing methods and element types per mesh resolution.

Component	Method	Primary Element	Element Size [cm]			
			Coarse	Medium	Fine	Ideal
Observation Window	Tetrahedrons		7.5	7.0	6	1.5
Bow	Automatic	Ansys Selected	21	19.5	18	3
Bow Base	Sweep	Quadrilaterals	7.125	6.0	5.25	1.5
O-Ring Stern to Cyl.	Sweep	Quadrilaterals	7.125	6.0	5.25	1.5
Cylindrical Section	Quadrilateral Dominant	Quadrilaterals	10.5	9.5	9.188	4
O-Ring Bow to Cyl.	Sweep	Quadrilaterals	7.125	6.0	5.25	1.5

Stern Base	Sweep	Quadrilaterals	7.125	6.0	5.25	1.5
Stern	Automatic	Ansys Selected	9.0	8.5	7.875	2

To achieve a uniform mesh in a large structure, like the Titan Submersible, several refinements and smaller element sizes would be expected. Nevertheless, since Ansys' student license limits the Static Structural solution to no more than 32,000 elements, the main constraint was to select element sizes relatively close to each other without exceeding this node limit. Unsurprisingly, the element quality would be compromised without being able to implement smaller element sizes. An "ideal" element size was developed, but not executed due to Ansys license limitations, to contrast the impact of implementing a smaller element size on the mesh quality. The initial global target, minimum, and maximum element sizes are summarized in table 5.6, located below. These sizes were initially used to define the mesh resolution, but more specific adjustments and refinements were developed, as can be seen in columns four through six of table 5.5. In the case of the coarse mesh, for example, a global target size of 7.125 cm was intended; however, this element size appeared to be inadequate for mesh quality in the bow and was relaxed to 21cm. In the case of the medium-resolution mesh, the target element size of 6cm was also relaxed to 9.5cm in the cylindrical section because good-quality elements could be obtained at this size. Relaxing the number of elements without reducing the mesh quality is perceived as an acceptable practice, as it will reduce the computational time required to obtain the FEM solution. Isometric, front, and lateral views of the coarse, medium, fine, and ideal meshes can be observed in figures 5.5a through 5.8c.

Table 5.6 - Global mesh settings per mesh type.

Global Attribute	Coarse	Medium	Fine	Ideal
Target Element Size [cm]	7.125	6.0	5.25	1.5
Minimum Element Size [cm]	0.007125	0.006	0.00525	0.0105
Maximum Element Size [cm]	7.125	6.0	5.25	1.5
Order	Quadratic	Quadratic	Quadratic	Quadratic
Growth Rate	1.2	1.2	1.2	1.1
Total Nodes	43,989	59,667	86,071	2,102,175
Total Elements	15,484	21,928	31,024	1,061,591

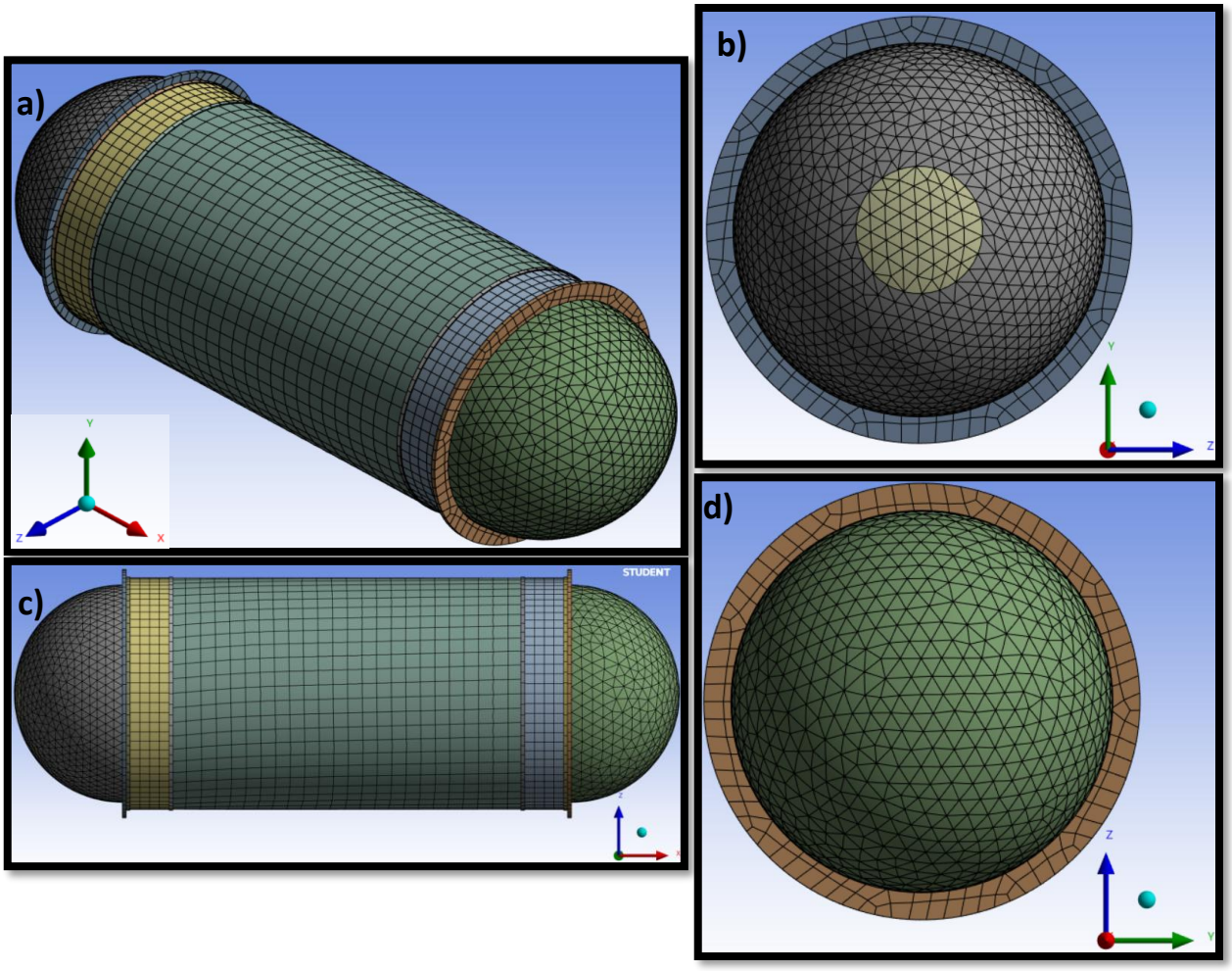

Figure 5.5 – Coarse mesh: a) Isometric, b) Front, c) Side, and d) Back views.

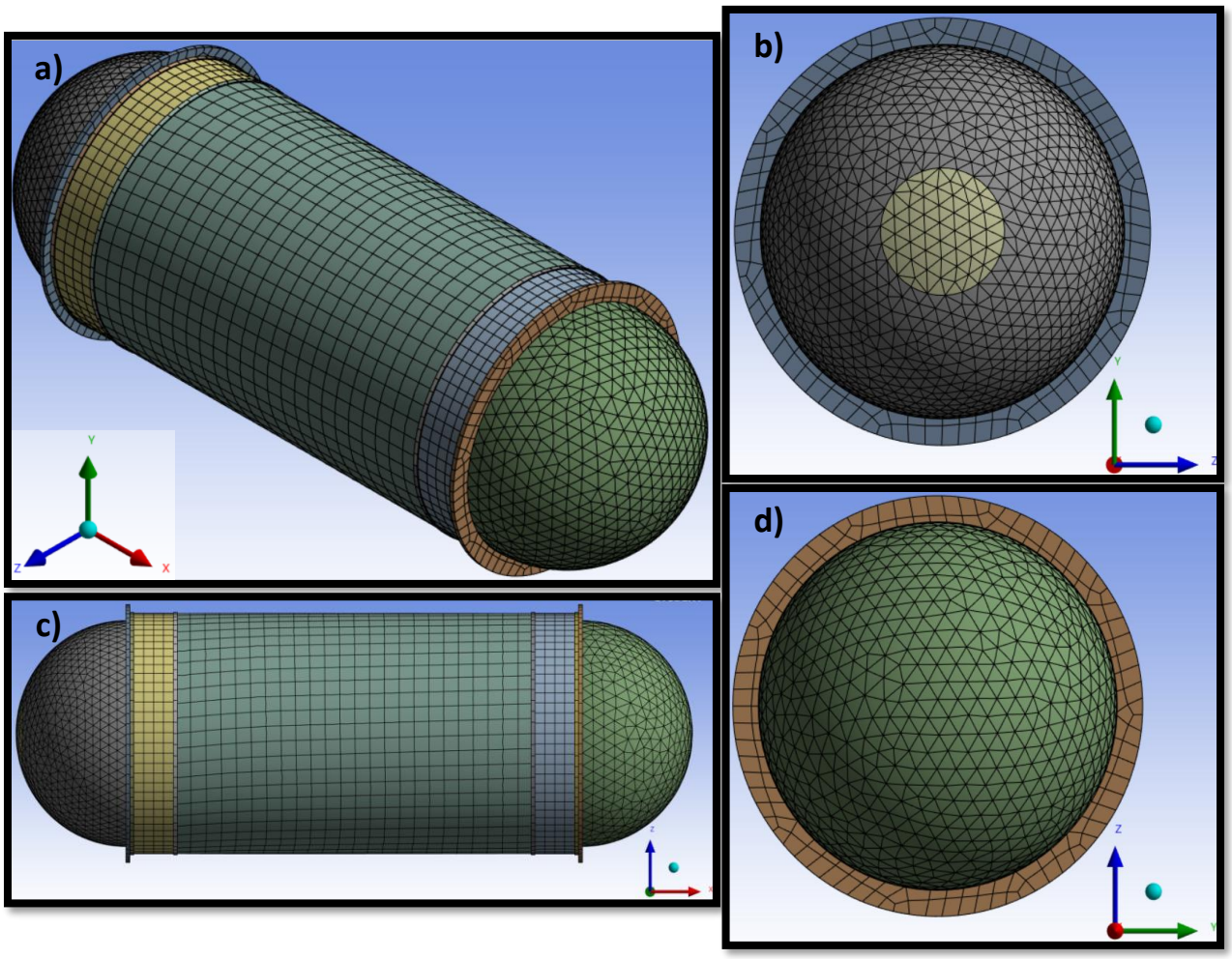

Figure 5.6 – Medium mesh: a) Isometric, b) Front, c) Side, and d) Back views.

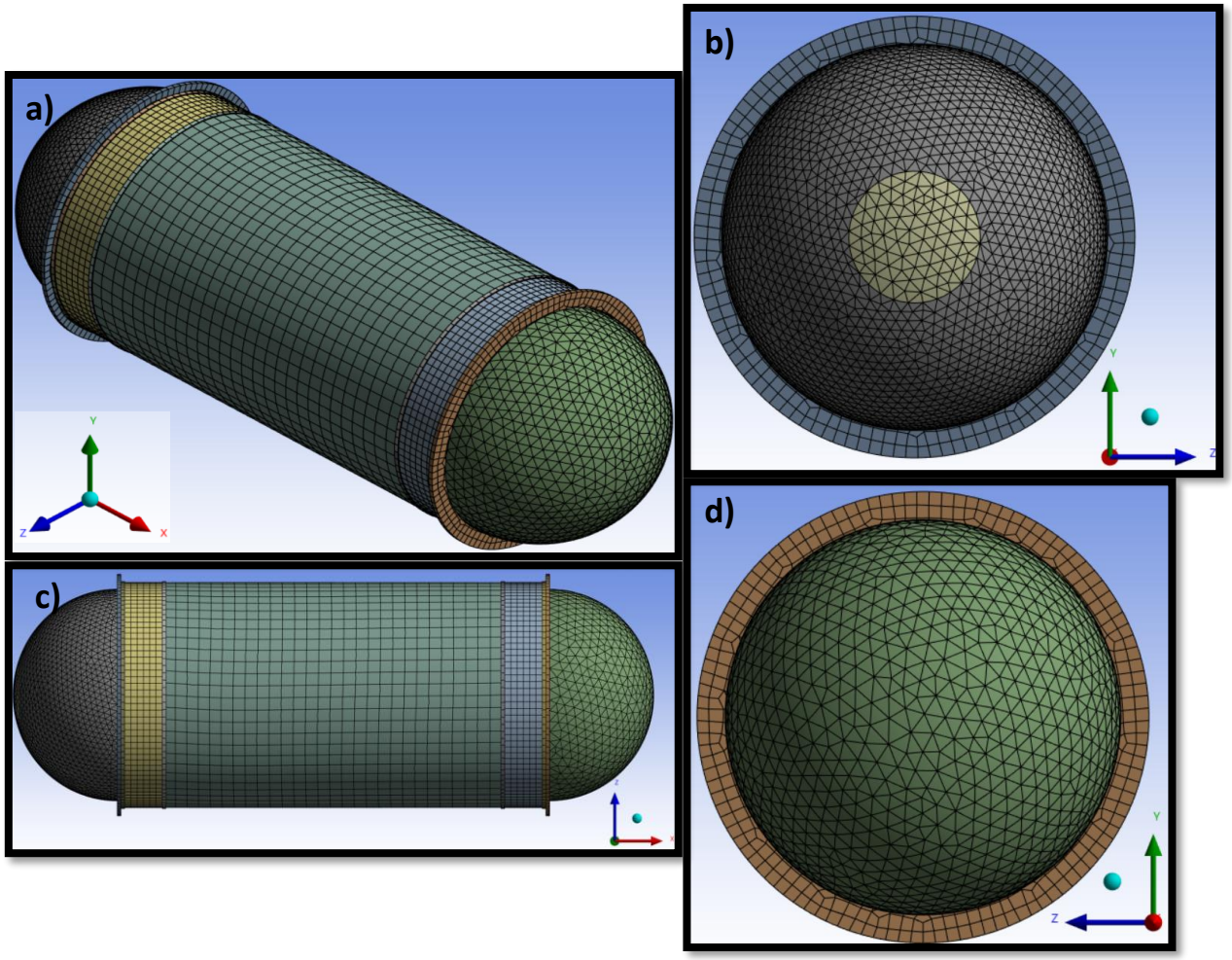

Figure 5.7 - Fine mesh: a) Isometric, b) Front, c) Side, and d) Back views.

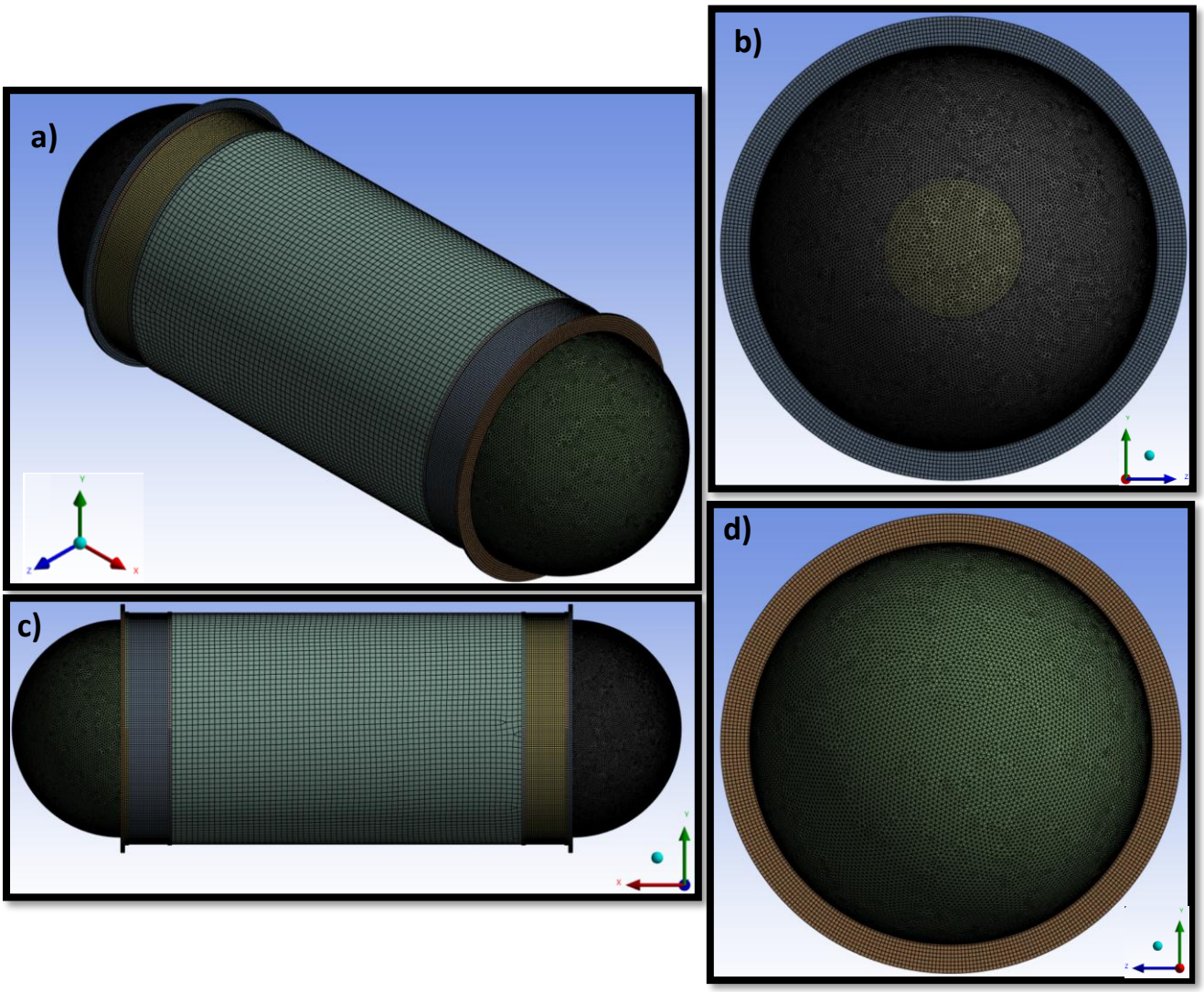

Figure 5.8 – Ideal mesh: a) Isometric, b) Front, c) Side, and d) Back views (not used due to Ansys's license limitations.

5.4 Boundary and Loading Conditions

A. Boundary Conditions.

Lastly, in preparation for generating the FEM solution, the boundary and loading conditions were implemented. This step occurs in the Static Structural environment of Ansys. To capture correctly the physical interactions between the structure and the simplified loading conditions, its environment was first observed. The submersible used vertical and lateral thrusters to guide its motion in the ocean, as can be seen in figure 5.9. In static conditions, the locations of these thrusters can be simplified as simple points. Implementing fixed supports at four locations would constraint the displacements of these four nodal locations to be zero, which might cause undesirable stress concentrations near vicinities of these supports. As a result, only two nodal locations were constrained with fixed supports. One of them was the node located at the intersection of the xy and yz planes, as illustrated by the top figure 5.10. The second nodal location corresponded to the node on the yz plane, at the edge of the axial location (x-axis), as in the bottom figure 5.10.

Figure 5.9 – Location of vertical thrusters of Titan Submersible [6].

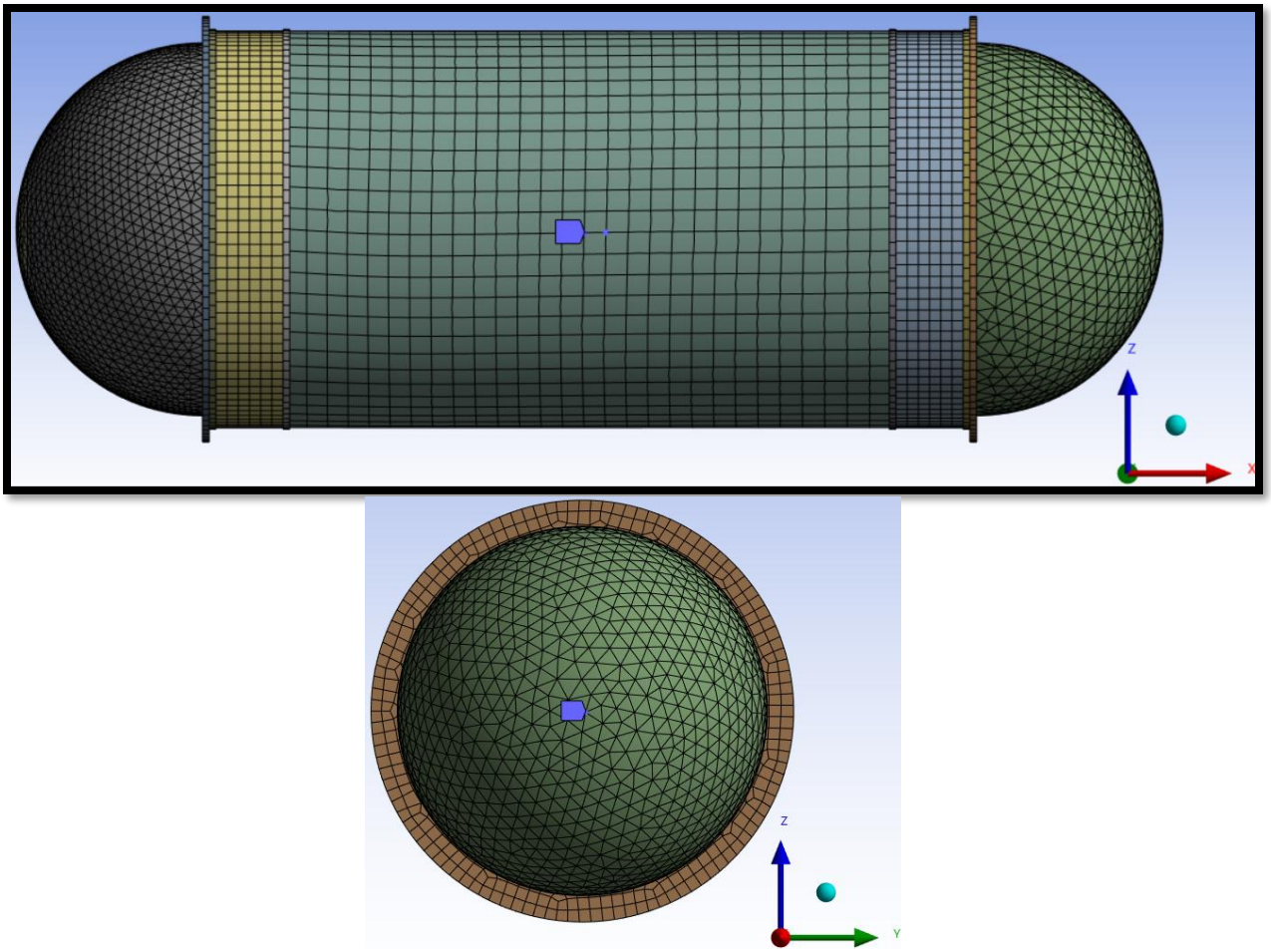

Figure 5.10 – Implementation of Boundary Conditions: Fixed Supports.

B. Loading Conditions

As explained in section 1.1, at the lowest operating depth, corresponding to 4km, the submersible was exposed to a pressure of 40.33 MPa. In Ansys, this loading condition was represented with a hydrostatic pressure, which is determined according to equation 5.2. The fluid density, gravitational acceleration, and depth of the geometry are represented by $\rho, g,$ and h, respectively. Consequently, implementing the density of sea water, acceleration due to gravity on earth, and operational depth of the submersible, as summarized in table 5.7, led to the corresponding hydrostatic pressure contours reflected in figure 5.11. Because the origin of the global coordinate system was placed at the geometric center of the pressure hull, lower pressure distribution is observed at the top of the hull than the bottom. At the top, the highest pressure is calculated as 40.41MPa, while the lowest pressure is 40.39MPa at the bottom.

$$P_{hydrostatic} = \rho g h \quad (5.2)$$

Table 5.7 - Hydrostatic pressure values applied in Ansys.

Variable	Units	Value
ρ	kg/m^3	1030
g	m/s^2	9.8066
h	m	4000

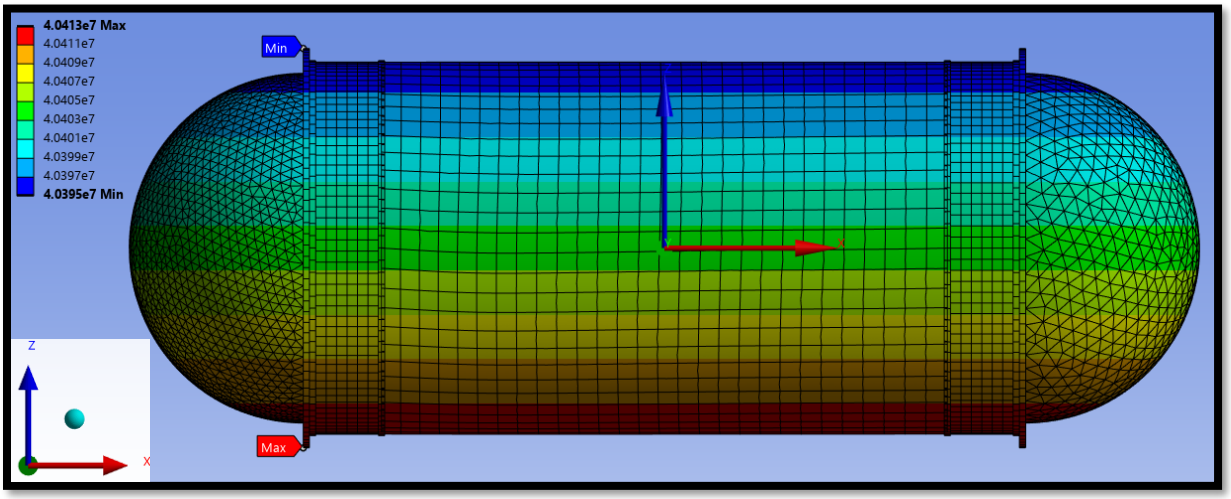

Figure 5.11 – Loading Condition: Hydrostatic pressure contour generated by Ansys.

6.0 Results and Future Work

6.1 Results

After implementing the previous boundary and loading conditions, results were generated in Ansys. For convenience to the reader, these results are grouped by their mesh size, in the subsections below, A through C. For each mesh size, three figures are presented in the following order. First are the lateral and front views, capturing the xz and yz planes from both sides. Next is the composite failure tool, showing whether failure occurred in any of the plies.

Three main observations can be made across all types of mesh resolution. First, qualitatively, all results show that the largest displacement occurs at the edge of the joining O-Ring, on the bow side. This can be observed in figures 6.1, 6.4, and 6.7. Similarly, is noticed that the slightly bigger pressure gradient is "bending" the submersible upward, since there is a larger stress concentration at the bottom of the submersible (negative z-axis) than the upper section, as previously visualized in figure 5.11. Secondly, with this modelled layup, failure is predicted in every mesh resolution. This is illustrated by figures 6.3, 6.6, and 6.9, where the safety margin of one is exceeding, signaling material failure. In most cases, this occurs in the "red" areas, which are observed to be the edges of the cylindrical section and the middle section. As a result, additional reinforcement will be required in these sections by either increasing the shell thickness or numerically testing different layups, possibly alternating ± 30, ± 45, ± 53, or ± 60 degrees. Lastly, the acrylic window is observed to undergo significant deformation, as its original spherical shape is observed to compress inward, consistent with its expected physical behavior. This can be observed in the upper images of figures 6.1, 6.4, and 6.7.

A. Coarse Mesh

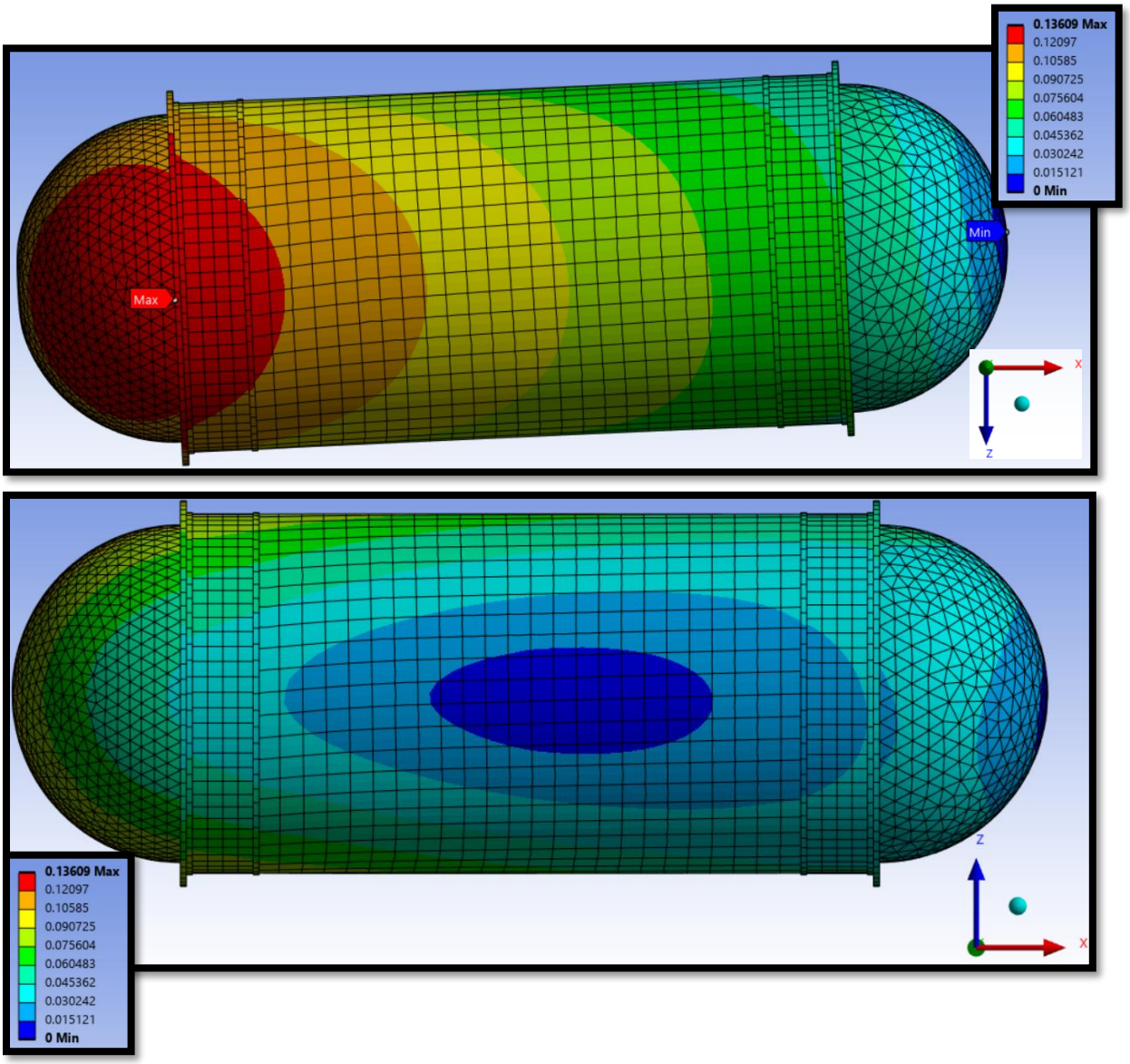

Figure 6.1 – Displacement from lateral views of the xz plane.

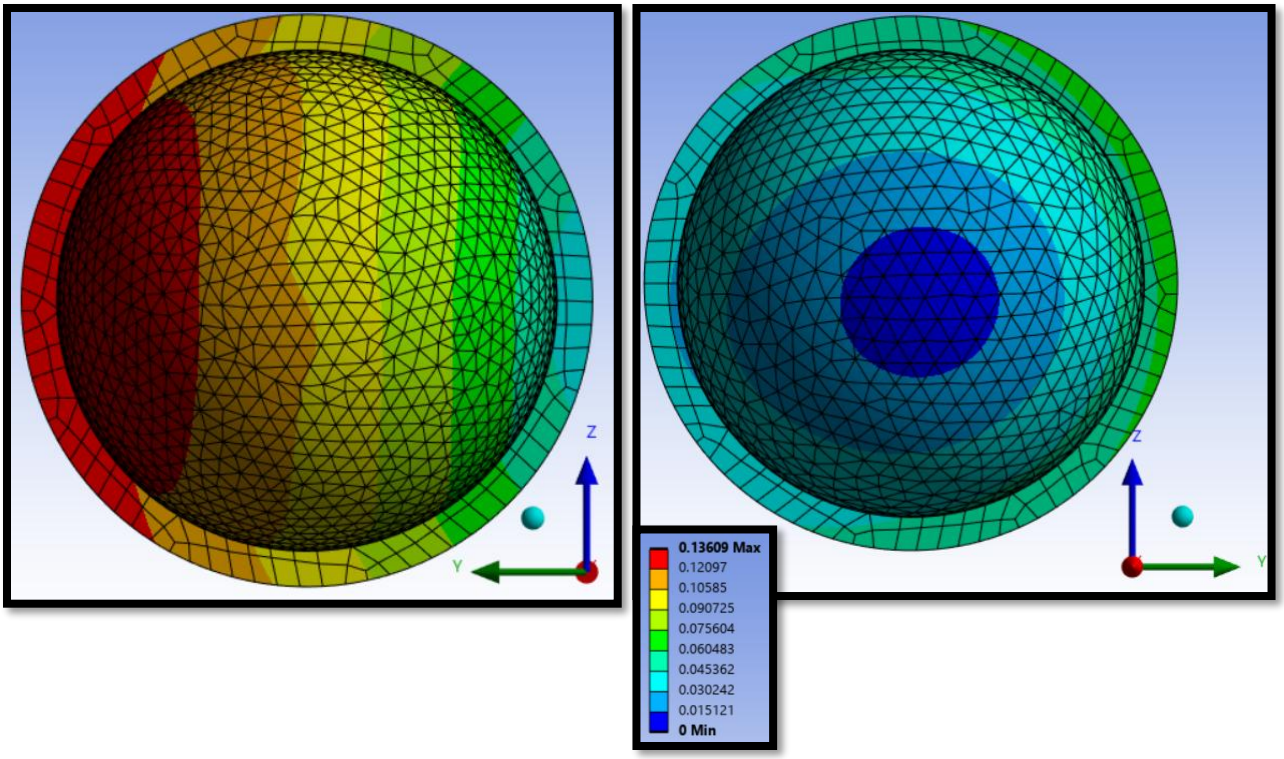

Figure 6.2 – Displacements from the front and back views of the yz plane.

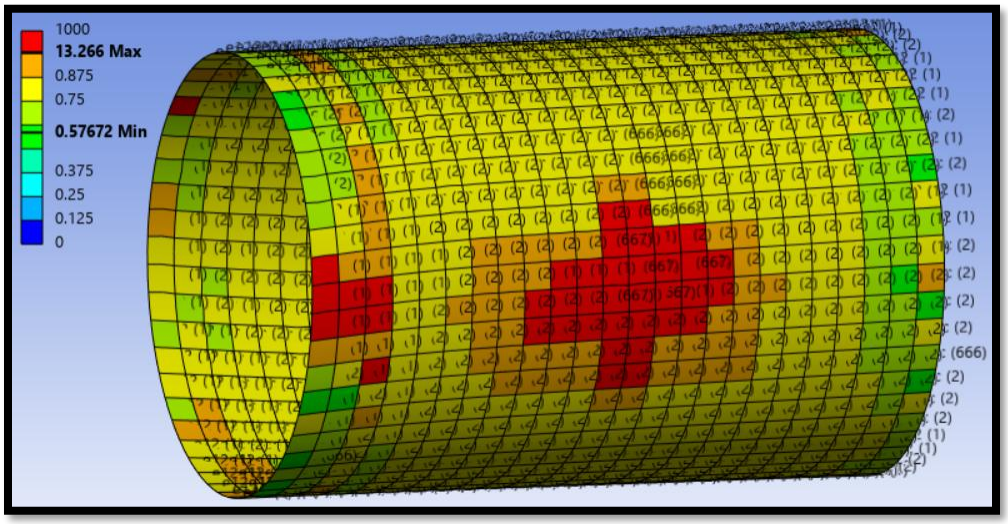

Figure 6.3 – Ansys's failure composite tool.

B. Medium Mesh

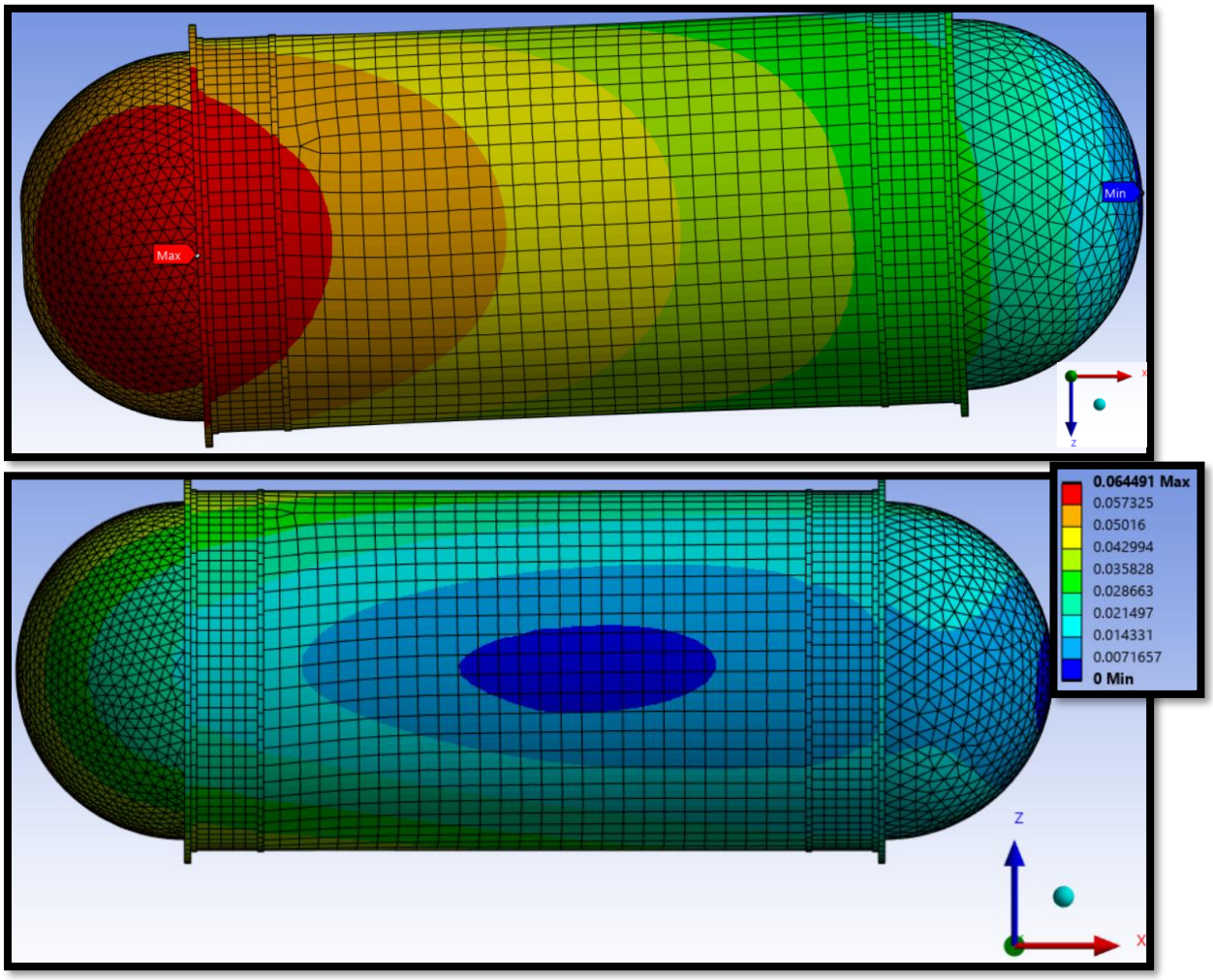

Figure 6.4 – Displacement from lateral views of the xz plane.

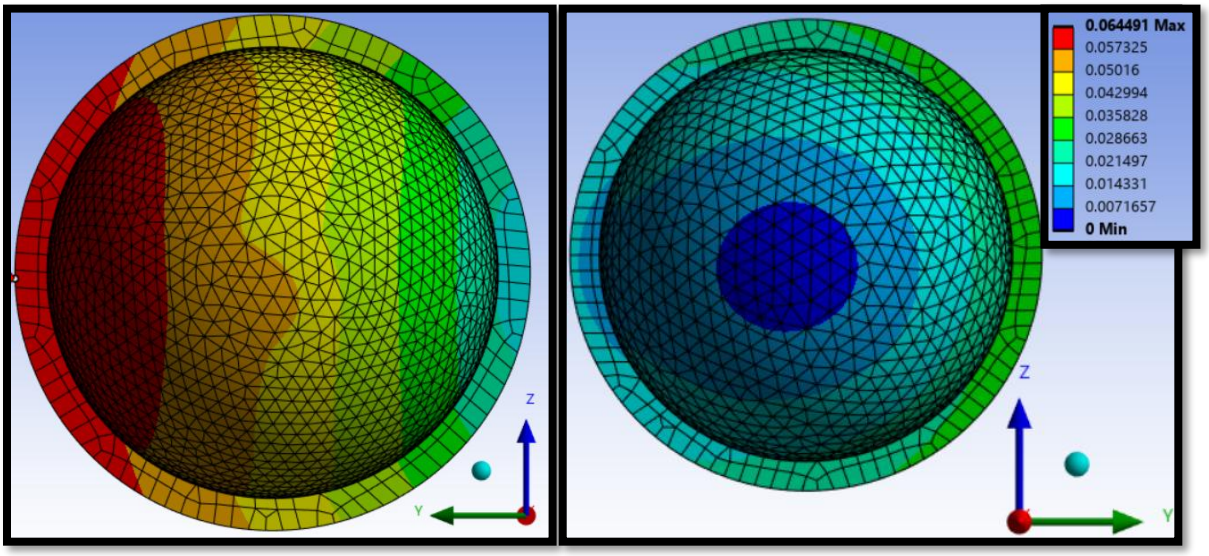

Figure 6.5 – Displacements from the front and back views of the yz plane.

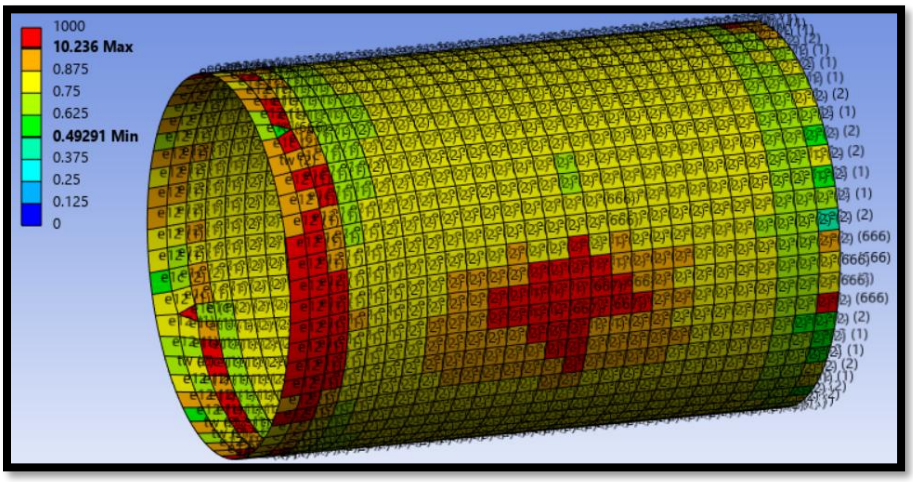

Figure 6.6 – Ansys's failure composite tool.

C. Fine Mesh

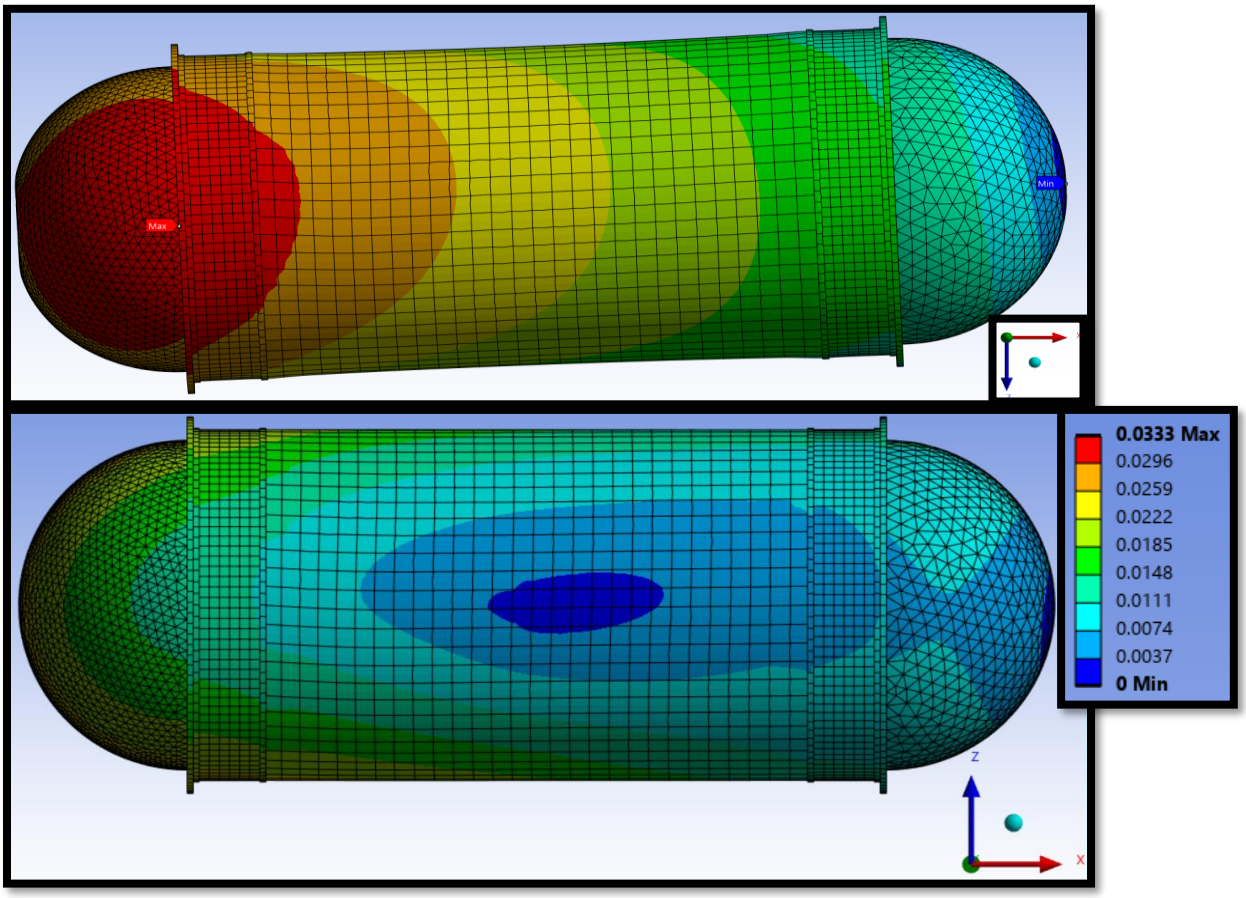

Figure 6.7 – Displacement from lateral views of the xz plane.

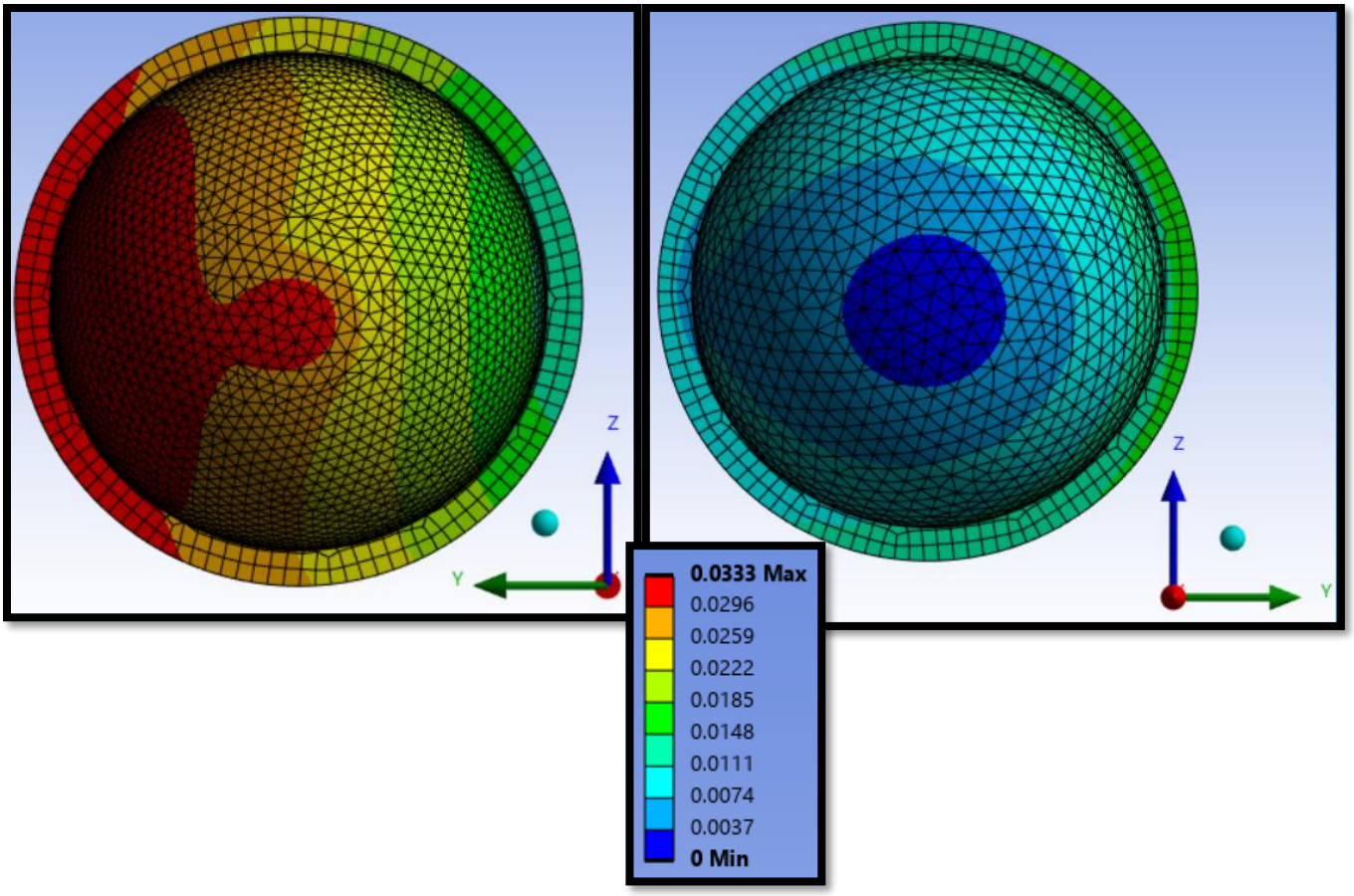

Figure 6.8 – Displacements from the front and back views of the yz plane.

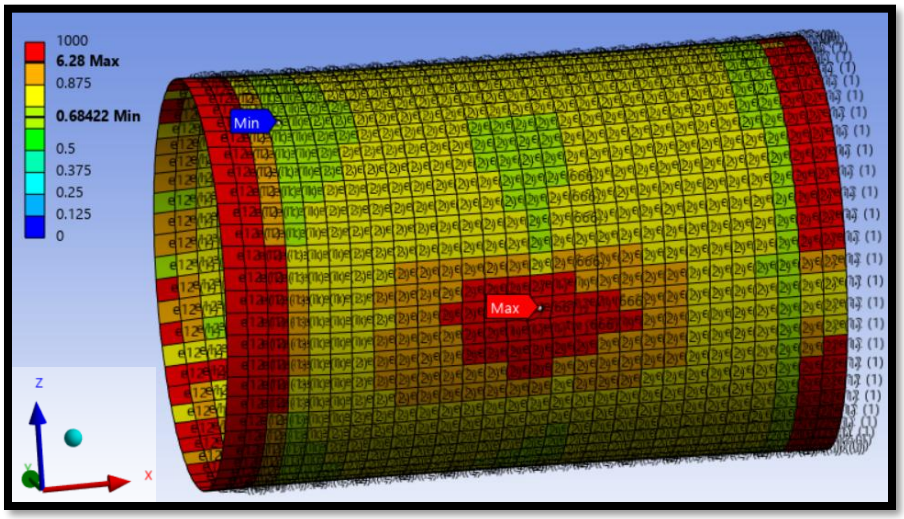

Figure 6.9 – Ansys's failure composite tool.

6.2 Convergence Study

As previously signaled, at the time this work was conducted, Ansys's solver limited the solution to 32,000 elements. Consequently, the number of nodes and subsequent reductions had to be closely tailored around this limit. Five different nodal locations were selected to investigate numerical convergence within the nodal limits of Ansys's student license. In more detail, these nodal locations were extracted from the xy plane. One selection was made for the stern, one for the stern-side O-Ring, two for the cylindrical section, flaking the origin, and one for the window. They can be visualized in figure 6.10. The predicted displacements for each selected nodal location, and its mesh resolution, are compiled in table 6.1. It can be observed that the displacements are significantly larger for the coarse mesh. In the case of the maximum displacement, for example, the computed magnitude was 13.61cm, while for the fine this value reduced to 3.33cm. This is expected, as the assigned target element size of the coarse mesh was 7.125cm, while the fine mesh used 5.250cm to remain within Ansys's element number limits. Given the difference is displacement magnitude, the author wished he could execute additional mesh refinements to observe further numerical convergence. For visualization, these values are plotted in figure 6.11.

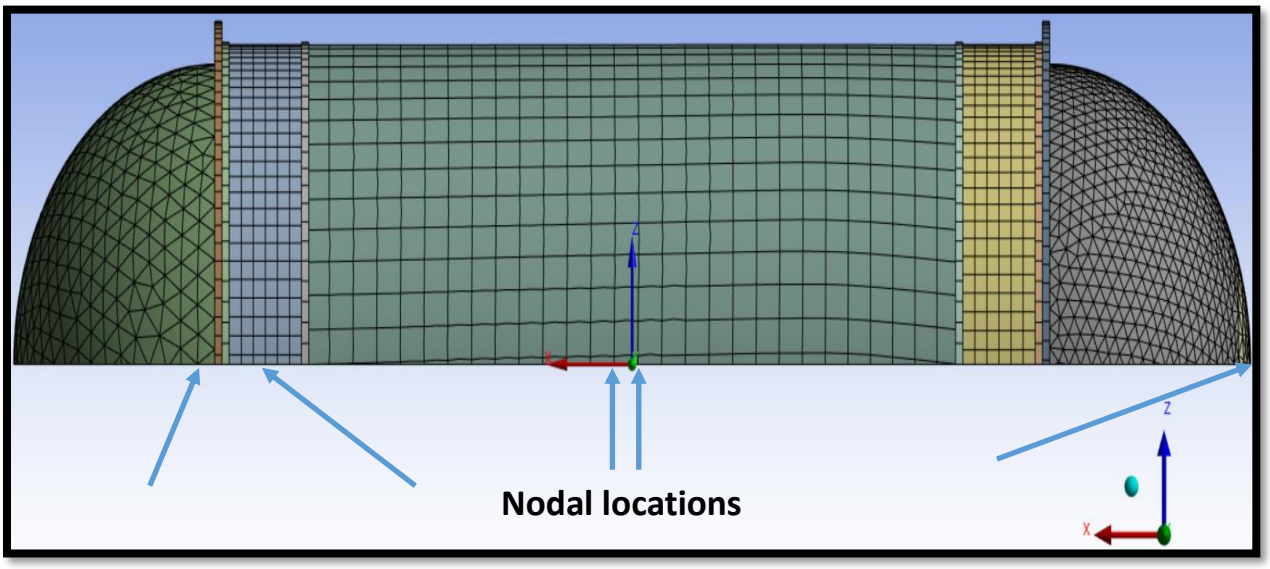

Figure 6.10 - Selected nodal locations for numerical convergence.

Table 6.1 - Displacements at five nodal locations to observe convergence.

Mesh	Target Element Size [cm]	Total Nodes	Total Elements	Displacement max [cm]	Nodal Displacement [cm]				
					Stern	O-Ring, Stern Side	Cabin, Left	Cabin, Right	Window
Coarse	7.125	43,989	15,484	13.61	5.66	6.52	9.46	9.69	10.63
Medium	6.000	59,667	21,928	6.45	2.92	3.23	4.70	4.79	5.19
Fine	5.250	86,071	31,024	3.33	1.40	1.61	2.34	2.39	3.08

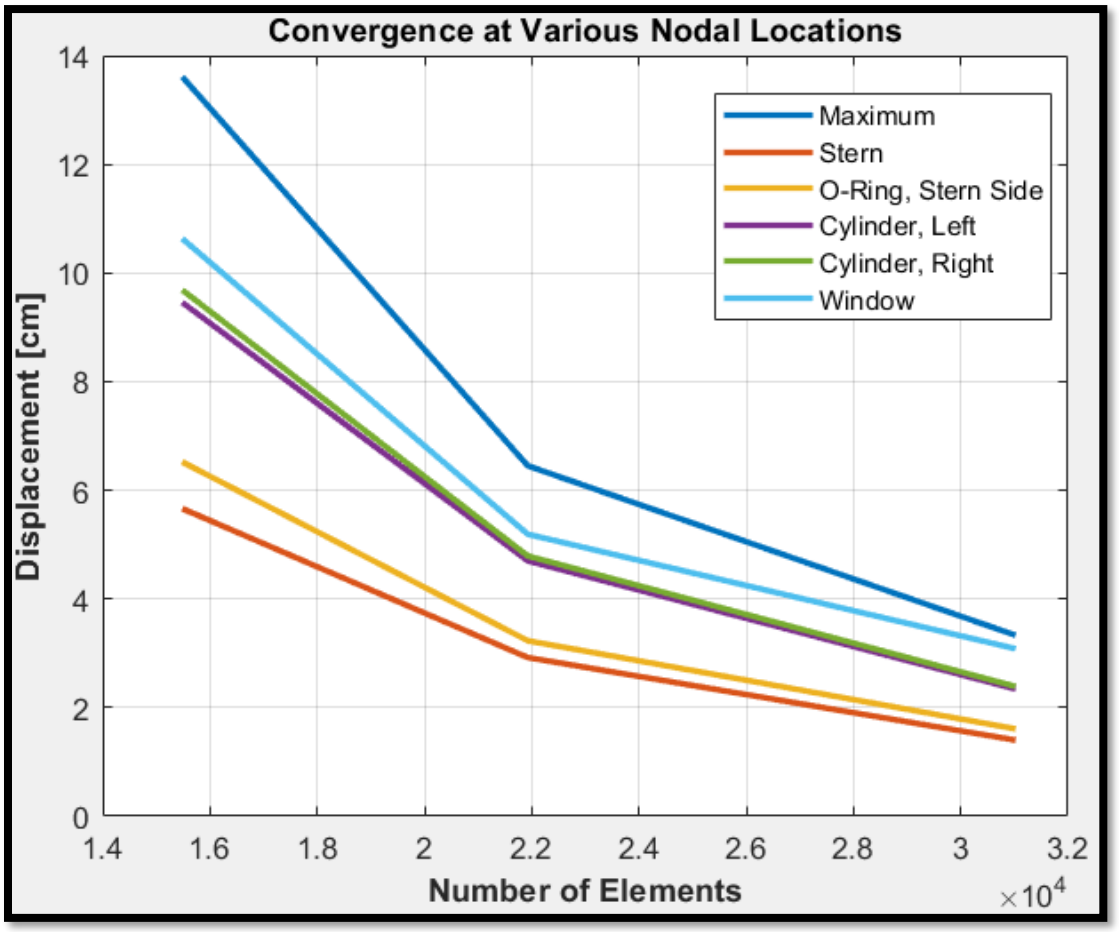

Figure 6.11 – Convergence at selected nodal locations.

6.3 Failure of Isotropic Materials

Although a finer mesh is likely required to truly identify certain mesh resolution as the converged solution, given Ansys's student license limitations, the fine mesh was treated as the solution. Consequently, the von-Mises and Tresca criteria were used to evaluate potential areas of failure of isotropic materials, namely the Titanium components and PMMA observation window. It can be observed that the rims of the Titanium O-Ring interfaces experience the lowest safety factor by both von-Mises and Tresca theories. These numbers correspond to 0.10509 and 0.091568, respectively, suggesting that additional reinforcement, such as a bigger thickness, is required to ensure structural integrity is maintained in these at-risk areas. Figures 6.12 and 6.13 illustrate the results obtain implementing both failure criteria.

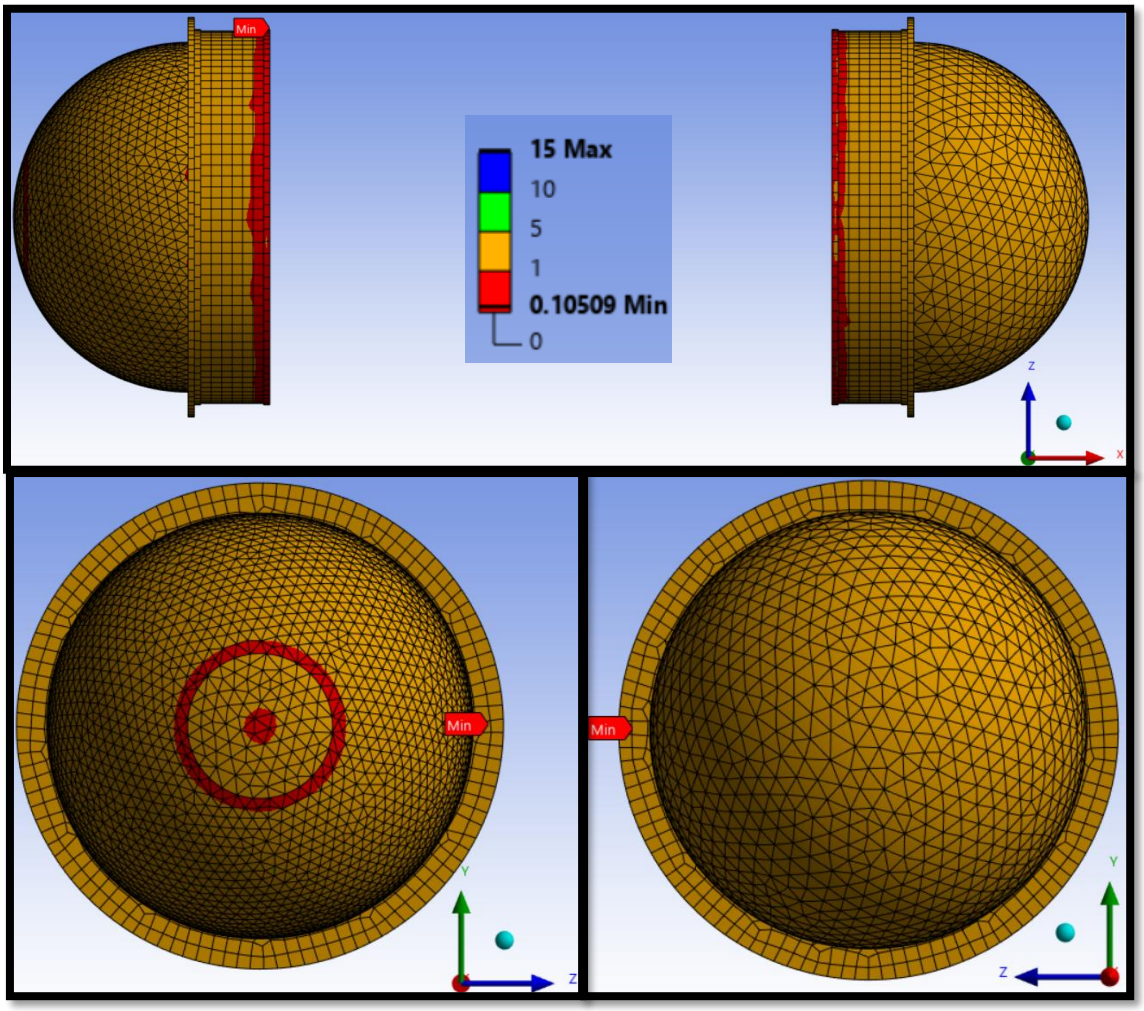

Figure 6.12 – Failure of Isotropic Materials in Ansys by von-Mises criteria.

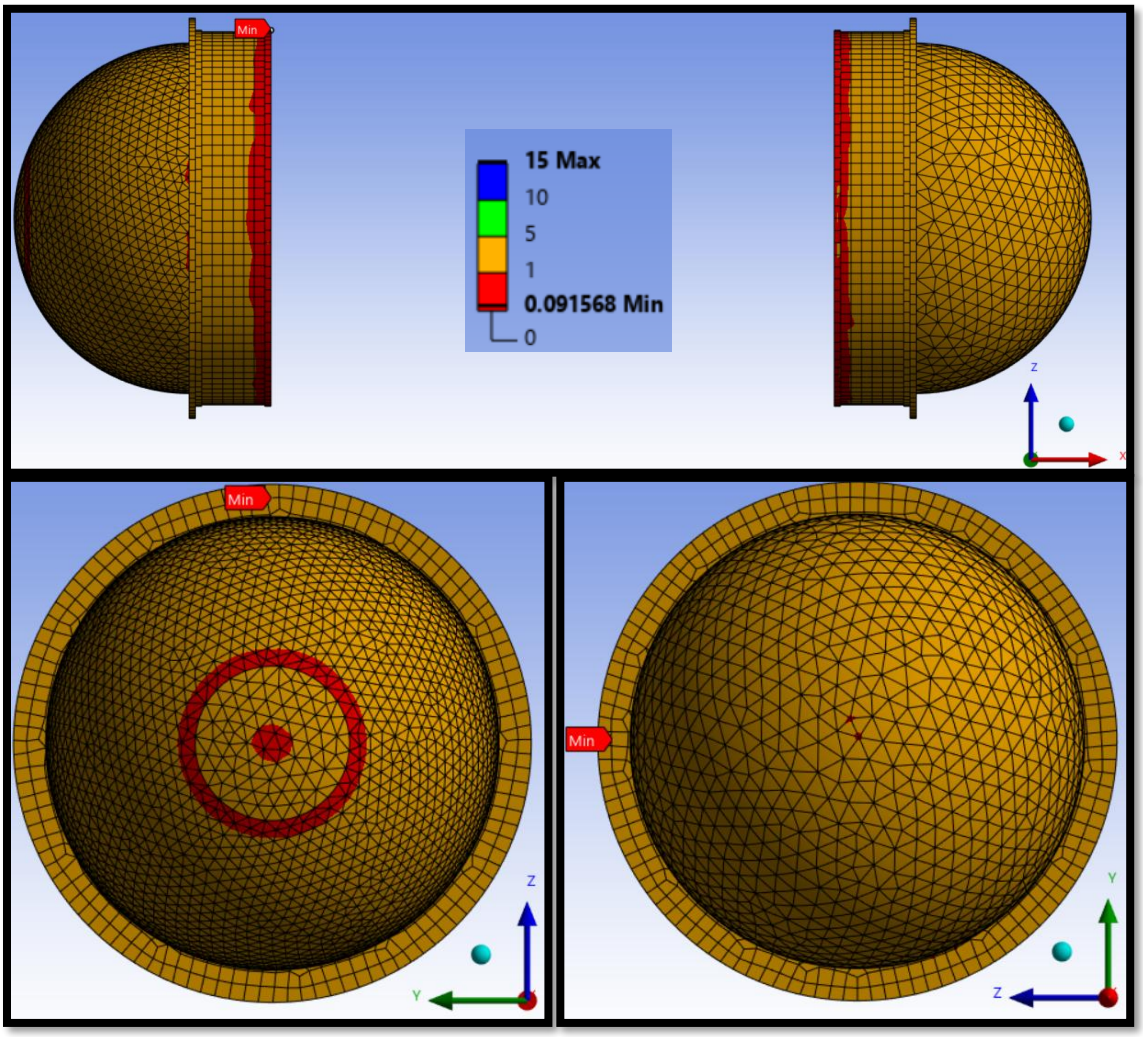

Figure 6.13 – Failure of Isotropic Materials in Ansys by Tresca criteria.

6.4 Comparison to Analytical Model

As indicated in the previous paragraph, additional mesh refinements are needed to further investigate convergence. Given the trends observed in figure 6.11, the author suspects it is highly likely to observe further decreases in predicted displacements for more refined mesh sizes. The analytical model discussed in chapter 5.1 predicted a maximum radial displacement of 0.226cm while the fine mesh reported 3.05cm. The analytical theory predicts the location to be at about 1/3 and 2/3 of the cylinder length, whereas the FEM solution identified two main failure areas: near the edges of the cylindrical pressure hull and the middle-section, 1/2 location of the cylinder length. As previously identified in subsection 5.2, the presented analytical approach was not valid near the edges, where Kollár and Springer [43] asserted that different methods should be used. The magnitude of the total displacements generated by the FEM solution is observed to be smaller in

areas away from the edges. The analytical and numerical results are included in figure 6.14, located below.

Table 6.2 - Comparison of maximum displacements in cylindrical pressure hull.

Model		Maximum Displacement [cm]	Region	Consideration
Analytical		0.226	1/3 and 2/3 of cylinder radial direction	Theory is not valid for areas near the edges.
Ansys	Coarse	12.849	Near edge	Better agreement observed for areas away from the edges.
	Medium	5.94		
	Fine	3.05		

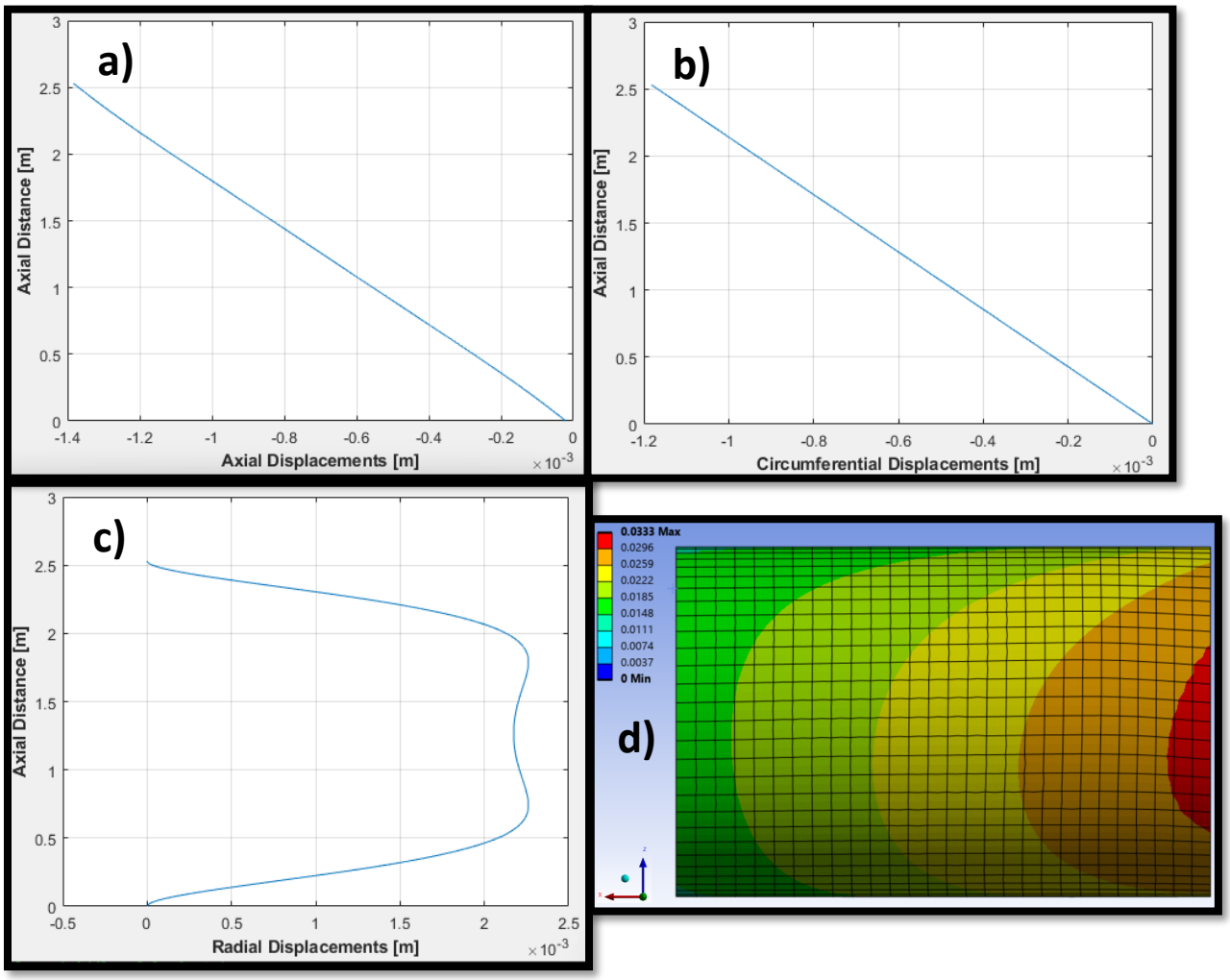

Figure 6.14 – Analytical versus FEM solution predicted displacements.

6.5 Concluding Remarks

Before formulating conclusions, the limitations and assumptions of this study must be reconsidered. First, the geometry model used in this prototype was created from available online resources and best-engineering judgement. Despite carefully investigating the dimensions and material properties, without knowing the specific values used by the manufacturers, these efforts remain, at best, and approximation to the "actual" predicted values conducted by the then active OceanGate company. The connections between components, such as the window and bow, and O-Rings to cylindrical and spherical sections were assumed to be perfectly bonded and unaffected by water intrusion. This idealization might not be the case, as manufacturing practices can dramatically affect porosity and imperfections between contact surfaces; consistent duty cycles are also expected to further degrade these bonding interfaces. In other words, bonding degradation is likely to exist and was not included in this study. Third, given the student license limitations of Ansys, additional mesh refinements are required to visualize the true extent of convergence before certain mesh resolution is assessed as "true". The author urges the reading audience to maintain these considerations in mind and is happy to provide drawings and higher-resolution (ideal) meshing for additional studies with a full commercial Ansys license.

Nonetheless, using the highest resolution created mesh, under the 32,000 elements limit, provides valuable qualitative information for future submarine vehicle prototyping and testing. The middle and edge sections of the cylinder experience the greatest deformations, where additional reinforcement should occur. Alternating layup orientations identified previously, such as ± 30, ± 45, ± 53, or $\pm 60°$ could be implemented to better distribute the pressure loads across the structure. Similarly, for the isotropic materials, the Titanium O-Ring interfaces were identified as the areas experiencing the lowest safety factors, for which additional thickness can be added to better withstand the working environment.

6.6 Future Work

Without a doubt, using additional resources, specifically a full-Ansys license, the author would opt to further refine the mesh until numerical convergence is further explored. This will enable the analyst to better understand the "converged" stress values experienced by the structure. Additionally, since the submersible reportedly used an alternating layup of $[(0, 90)_{333s}, 0]$, the author proposes to explore the cases in table 6.3 and determine whether these configurations lead to greater safety factors.

Table 6.3 - Potential continuation study cases for this investigation.

Case	Modification
1	1.5x thickness increase in thickness in pressure hull and titanium hemispheres
2	3.0x thickness increase in thickness in pressure hull and titanium hemispheres
3	Nominal Thicknesses, ply layout [0, 30, 60, 90]s, ceteris paribus
4	Ply layout [0, 30, 60, 90]s; 1.5x global thickness increase
5	Ply layout [0, 30, 60, 90]s; 3.0x global thickness increase

References

[1] *"Global Positioning System (GPS),"* Time and Navigation, National Air and Space Museum, Smithsonian Institution, https://timeandnavigation.si.edu/satellite-navigation/gps [accessed 24 May 2024].

[2] Newman, P. G., and Rozycki, G. S., "The History of Ultrasound," Surgical Clinics of North America, Vol. 78, No. 2, 1998, pp. 179-195. doi:10.1016/S0039-6109(05)70308-X

[3] "*Ultrasound,"* Mayo Clinic, 11 Feb. 2023. https://www.mayoclinic.org/tests-procedures/ultrasound/about/pac-20395177 [accessed 24 May 2024].

[4] "*OceanGate Home,"* OceanGate Inc., archived by Wayback Machine, 21 June 2023. https://web.archive.org/web/20230621213636/https://oceangate.com/ [accessed 24 May 2024].

[5] Rondeau, R., *"History Repeats Itself: The Titan Submersible Implosion Mirrors Past Disasters,"* The Canadian Press, 27 June 2023. http://search.proquest.com.libaccess.sjlibrary.org/wire-feeds/history-repeats-itself-titan-submersible/docview/2830950850/se-2

[6] Brunn, E. C., *"Technical Note: Comparison of the Titan Deep Submersible to Older Designs," Rakenteiden Mekaniikka (Journal of Structural Mechanics)*, Vol. 56, No. 3, 2023, pp. 121–126. https://doi.org/10.23998/rm.138288

[7] *"Titan (Submersible),"* Wikipedia, https://en.wikipedia.org/wiki/Titan_(submersible) [accessed 24 May 2024].

[8] "*What's the Difference Between a Submersible and a Submarine?"* The Seattle Times, https://www.seattletimes.com/nation-world/whats-the-difference-between-a-submersible-and-a-submarine/ [accessed 24 May 2024].

[9] Quinn, B., et al., *"Missing Titanic Sub: What is the Titan Submersible and What Might Have Happened?"* The Guardian, 20 June 2023. https://www.theguardian.com/uk-news/2023/jun/20/missing-titanic-sub-titan-submersible-tourist-oceangate-what-is-it-and-what-might-have-happened

[10] Nahas, A., *"OceanGate's Titan Submersible: Everything to Know,"* People, https://people.com/oceangate-titan-submersible-everything-to-know-7551180 [accessed 24 May 2024].

[11] *"How Does Pressure Change with Ocean Depth?"* NOAA National Ocean Service, https://oceanservice.noaa.gov/facts/pressure.html [accessed 24 May 2024].

[12] Hasan, M. H., Sidhu, R. S., Samad, Z., and Mehmood, F., "A Review on Structural Failure of Composite Pressure Hulls in Deep Sea," *Composite Structures*, Vol. 276, 2021, Paper No. 113128. https://doi.org/10.1016/j.compstruct.2021.113128

[13] Hill, R., “A Theory of the Yielding and Plastic Flow of Anisotropic Metals,” *Proceedings of the Royal Society of London. Series A. Mathematical and Physical Sciences*, Vol. 193, No. 1033, 1948, pp. 281–297. https://doi.org/10.1098/rspa.1948.0045

[14] Azzi, V. D., and Tsai, S. W., “Anisotropic Strength of Composites,” *Experimental Mechanics*, Vol. 5, 1965, pp. 283–288. https://doi.org/10.1007/BF02326292

[15] Tsai, S. W., and Wu, E. M., “A General Theory of Strength for Anisotropic Materials,” *Journal of Composite Materials*, Vol. 5, No. 1, 1971, pp. 58–80. https://doi.org/10.1177/002199837100500106

[16] Hashin, Z., “Failure Criteria for Unidirectional Fiber Composites,” *Journal of Applied Mechanics*, Vol. 47, 1980, pp. 329–334. https://doi.org/10.1115/1.3153664

[17] Puck, A., and Schürmann, H., “Failure Analysis of FRP Laminates by Means of Physically Based Phenomenological Models,” *Composites Science and Technology*, Vol. 58, 1998, pp. 1045–1067. https://doi.org/10.1016/S0266-3538(96)00140-6

[18] Talreja, R., “Physical Modelling of Failure in Composites,” *Philosophical Transactions of the Royal Society A: Mathematical, Physical and Engineering Sciences*, Vol. 374, No. 2071, 2016, Paper No. 20150280. https://doi.org/10.1098/rsta.2015.0280

[19] Wenxuan, Q., Weixing, Y., and Haojie, S., “A Micro–Macro Damage Mechanics-Based Model for Fatigue Damage and Life Prediction of Fiber-Reinforced Composite Laminates,” *Applied Composite Materials*, Vol. 29, 2022, pp. 1795–1816. https://doi.org/10.1007/s10443-022-10039-y

[20] Li, Y., Yu, C., Wang, W., Li, H., and Jiang, X., “A Review on Structural Failure of Composite Pressure Hulls in Deep Sea,” *Journal of Marine Science and Engineering*, Vol. 10, No. 1456, 2022. https://doi.org/10.3390/jmse10101456

[21] Ross, C. T. F., Little, A. P. F., and Haidar, Y., “Buckling of Carbon/Glass Composite Tubes under Uniform External Hydrostatic Pressure,” *Strain*, Vol. 47, 2011, pp. 156–174. https://doi.org/10.1111/j.1475-1305.2009.00664.x

[22] Pavlopoulou, S., Roy, S. S., and Gautam, M., “Numerical and Experimental Investigation of the Hydrostatic Performance of Fibre Reinforced Tubes,” *Applied Composite Materials*, Vol. 24, 2017, pp. 417–448. https://doi.org/10.1007/s10443-016-9530-7

[23] Zhang, X., Li, Z., Wang, P., and Pan, G., “Experimental and Numerical Analyses on Buckling and Strength Failure of Composite Cylindrical Shells under Hydrostatic Pressure,” *Ocean Engineering*, Vol. 249, 2022, Article No. 110871. https://doi.org/10.1016/j.oceaneng.2022.110871

[24] Kachnov, L. M., *Delamination Buckling of Composite Materials*, Mechanics of Elastic Stability, Springer, Dordrecht, The Netherlands, 1988. https://doi.org/10.1007/978-94-009-2807-0

[25] Luo, S., and Wang, W. B., "Research on the Delamination Snap Buckling of Composite Spherical Shells under Uniform External Pressure," *Journal of Ship Mechanics*, Vol. 26, 2022, pp. 91–102.

[26] Zheng, J., and Zhao, M., "Fluid-Structure Interaction of Spherical Pressure Hull Implosion in Deep-Sea Pressure: Experimental and Numerical Investigation," *Ocean Engineering*, Vol. 291, 2024, Article No. 116378. https://doi.org/10.1016/j.oceaneng.2023.116378

[27] He, Z., Wang, F., Wang, H., and Zhao, B., "Parametric Analysis on Creep Deformation of Deep-Sea PMMA Observation Window," *Applied Sciences*, Vol. 14, No. 1040, 2024. https://doi.org/10.3390/app14031040

[28] Oden, J. T., "Historical Comments on Finite Elements," *Computing in Science and Engineering*, Vol. 10, No. 1, 1987, pp. 125–126. https://doi.org/10.1145/41579.41592

[29] Liu, W. K., Li, S., and Park, H. S., "Eighty Years of the Finite Element Method: Birth, Evolution, and Future," *Archives of Computational Methods in Engineering*, Vol. 29, No. 3, 2022, pp. 4431–4453. https://doi.org/10.1007/s11831-022-09740-9

[30] Best, G., and Oden, J. T., *Stiffness Matrices for Shell-Type Structures*, Research Report No. 233, Research & Engineering Department, General Dynamics, Fort Worth, TX, 1963.

[31] Swanson, J. A., "John Swanson and ANSYS—An Engineering Success Story," *Proceedings of the Winter Simulation Conference 2014*, Savannah, GA, 2014, pp. 3–4. https://doi.org/10.1109/WSC.2014.7019872

[32] Cook, R. D., Malkus, D. S., Plesha, M. E., and Witt, R. J., *Concepts and Applications of Finite Element Analysis*, 4th ed., Wiley, New York, 2001.

[33] Szabo, L., "What are the Types of Elements Used in FEA?" *Enterfea*, URL: https://enterfea.com/what-are-the-types-of-elements-used-in-fea/ [cited 11 July 2024].

[34] Reddy, J. N., *Introduction to the Finite Element Method*, 4th ed., McGraw Hill LLC, New York, 2018.

[35] ANSYS, Inc., *ANSYS Composite PrepPost User's Guide*, Release 2025 R1, Canonsburg, PA, 2025. Available: https://ansyshelp.ansys.com/public/Views/Secured/corp/v242/en/acp_ug/acp_comp_project.html

[36] Washington University in St. Louis, *Abaqus User's Manual*, URL: https://classes.engineering.wustl.edu/2009/spring/mase5513/abaqus/docs/v6.6/books/usb/default.htm?startat=pt03ch06s02at01.html [accessed 9 Nov. 2024].

[37] GeekWire, "GW Summit Power Talk: Journey to the Titanic with Stockton Rush, Chief Submersible Pilot, OceanGate," *YouTube*, uploaded 16 April 2021. Available: https://www.youtube.com/watch?v=9PGpjEDc96I

[38] ThinkReliability, "Titan Submersible: Initial Insights from an Ongoing Investigation," *ThinkReliability Blog*, URL: https://blog.thinkreliability.com/titan-submersible-initial-insights-from-an-ongoing-investigation [retrieved 3 Dec. 2024].

[39] Bell, M., "Titan Sub | Carbon Fiber – Detailed Tour," *YouTube*, uploaded 16 March 2022. Available: https://www.youtube.com/watch?v=UO4IKYXacvM [accessed 28 Nov. 2024].

[40] Kunka, J., "Why OceanGate Titan Imploded – A Carbon Fiber Composites Perspective," *YouTube*, uploaded 10 July 2021. Available: https://www.youtube.com/watch?v=rie76UsjPZs [accessed 28 Nov. 2024].

[41] Custom Thumb Rings, "Thumb Ring Sizing Info," URL: https://www.customthumbrings.com/sizing-info [accessed 5 Dec. 2024].

[42] Fox News, "Haunting Photos Show Late OceanGate CEO Stockton Rush Test Diving His Titan Sub," URL: https://www.foxnews.com/us/haunting-photos-show-late-oceangate-ceo-stockton-rush-test-diving-his-titan-sub [accessed 12 Dec. 2024].

[43] Kollár, L. P., and Springer, G. S., *Mechanics of Composite Structures*, Cambridge University Press, Cambridge, England, 2003.

[44] Wagner, R., "The World's First Multi-Physics Simulation of the OceanGate TITAN," *YouTube*, uploaded 26 June 2024. Available: https://m.youtube.com/live/ciZHwe-9ago?t=274s

[45] U.S. Mint, "Coin Specifications," URL: https://www.usmint.gov/learn/coins-and-medals/circulating-coins/coin-specifications [retrieved 5 Mar. 2025].

[46] MatWeb, LLC, "Titanium Grade 3 (UNS R50550) Titanium CP3," *MatWeb Material Property Data*, URL: https://asm.matweb.com/search/SpecificMaterial.asp?bassnum=MTU030 [accessed 1 Apr. 2025].

Appendix A: Calculations of Nodal Displacements using FEM with MATLAB

```
%%   FEA of Bar with 5 elements
clear; close; clc;

%    Known Values
d = 0.3;           % Bar Base Diameter [m]
lf = 1;            % Total Bar Length [m]
E = 180e9;         % Young's Modulus - Steel, stainless AISI 302 [Pa]
A0 = (pi/4)*d^2;   % Base Area [m^2]
P = -100*9.81;     % Applied Load [N]

%    Nodal Properties
li = linspace(0, lf, 6);          % Nodal Location of Each Element
l = lf/5;                         % Length of Each Element
A = A0 - (1/(3*lf))*(2*A0*li);    % Nodal Elements Area [m^2]
k = (E/l).*A;                     % Stiffness of Each Element

%    Global Stiffness Matrix
k = [k(1)+k(2)    -k(2)             0             0             0             0;...
     -k(2)        k(1)+k(2)         -k(2)         0             0             0;...
     0            -k(2)             k(2)+k(3)     -k(3)         0             0;...
     0            0                 -k(3)         k(3)+k(4)     -k(4)         0;...
     0            0                 0             -k(4)         k(4)+k(5)     -k(5);...
     0            0                 0             0             -k(5)         k(5)];

%    Stiffness Matrix Before Reaction
kbr = k(2:end, 2:end);            % Extracts 2nd to last row and 2nd to last column

%    Force Vector Before Reaction
fbr = [0; 0; 0; 0; P];
f = [0; fbr];           % Force vector to solve for reaction

%    Displacements Before Reaction
ubr = kbr\fbr;          % Displacements before solving for reaction force
u = [0; ubr];           % Displacements to solve for reaction

%    Solving for Reaction Force
R = k*u - f;

%   Analytical Solution
x = linspace(0, lf, 1001);        % Length of Rod for Analytical Solution
uAn = ((3*lf*P)/(2*E*A0))*log((3*lf)./(3*lf - 2*x));

figure,
plot(x, uAn)
grid on
```

```
hold on
scatter(li, u, 25, 'filled')
legend('Analytical', 'FEM, 5-Elements')
xlabel('Bar Length [m]', FontWeight='bold')
ylabel('Displacement [m]', FontWeight='bold')
```

Appendix B: Calculations of Displacements for Cylindrical Section of the Pressure Hull

```
%%   Analytical Calculation of Displacements for Cylindrical Pressure Hull
%    Based on Equations from Ch 8.1 (Mechanics of Composite Structures (p. 397)
%    Developed by Ignacio Ramirez Romero
%    General Commands
clear all; close all; clc;

%    Cylinder Geometry
h = 12.7e-2;                    % Thickness [m]
L = 2.5298;                     % Length [m]
ri = 70.11e-2;                  % Inner Radius [m]
x = linspace(0, L, 25299);          % Displacement Array for Length

%    Loading Conditions
Pz0 = 40.33e6;                    % Constant Pressure [Pa]
Pz1 = 0;                        % Constant Pressure 2, if Pressure Distribution is used [Pa/m]
N = -Pz0*(pi*((ri+h)^2 - ri^2));       % Axial Load [N]
T = 0;                          % Torque [N*m]

%    Ply Geometry and Computation of ABD Matrix   ----------------------------
hLa = h;                        % Lamina Thickness [m]
or = repmat([0, 90], 1, 333);          % Array with Ply Orientation [[0, 90]_333s 0]
or = [or, 0];                   % Adds 0 Ply to match Titan's Laminate
plyNu = 1:length(or);                % Ply Number Assignment, Bottom to Top
hPly = hLa/(length(or));             % Thickness of Each Ply
zref = round(length(or)/2);           % Reference plane (middle of laminate)

%    Computation of Ply Properties using Rules of Mixture
%    Properties of Fiber
Ef1 = 231e9;                     % Longitudinal Youngs Modulus of Fiber [Pa]
Gf12 = 91e9;                     % Longitudunal Shear Modulus of Fiber [Pa]
nuf12 = 0.27;                    % Longitudinal Poisson's Ratio of Fiber
Vf = 0.7;                       % Volume Fiber Fraction

%    Properties of Matrix
Em = 2.8e9;                      % Matrix Young Modulus [Pa]
Gm = 1e9;                       % Matrix Shear Modulus [Pa]
num = 0.35;                      % Matrix Poisson's Ratio

%    Rules of Mixture Ply Properties
E1 = Ef1*Vf + Em*(1-Vf);
E2 = (Vf/Ef1 + ((1-Vf)/Em))^-1;
G12 = (Vf/Gf12 + ((1-Vf)/Gm))^-1;
nu12 = nuf12*Vf + num*(1-Vf);

%    Reduced Stiffness Matrix for reference ply at 0 deg
```

```
D = 1 - (E2/E1)*nu12^2;  % Engineering Constant [unitless]
Q0 = [E1/D,         (nu12*E2)/D,        0;...
    (nu12*E2)/D,   E2/D,               0;...
    0,             0,                  G12];

%    Calculation of Reduced Stiffness Matrix of All Other Plies
for i = 1:length(or)
   %     Defining the current angle th
   th = or(i);

   %     Checking if th = 0
   if th == 0
      % If th1 is 0, create Qth variable with name Qth1, Qth2, ..., Qth5
      eval(['Qth' num2str(i) ' = Q0;']);
   else
      %      Otherwise, compute Tsig and Teps based on the current angle (i)
      Tsig = [cosd(th)^2,      sind(th)^2,         2*cosd(th)*sind(th);...
            sind(th)^2,        cosd(th)^2,         -2*cosd(th)*sind(th);...
            -cosd(th)*sind(th), cosd(th)*sind(th),  cosd(th)^2 - sind(th)^2];

      Teps = [cosd(th)^2,      sind(th)^2,         cosd(th)*sind(th);...
            sind(th)^2,        cosd(th)^2,         -cosd(th)*sind(th);...
            -2*cosd(th)*sind(th), 2*cosd(th)*sind(th),  cosd(th)^2 - sind(th)^2];

      %      Computing Qth using the formula Qth = Tsig \ Q0 * Teps
      eval(['Qth' num2str(i) ' = Tsig\Q0*Teps;']);
   end
end

A = 0; % Initial value for loop summation
B = 0; % Initial value for loop summation
D = 0; % Initial value for loop summation

for i = 1:length(or)
   %     Calculating z values (z0, z1, z2, ..., zn)
   z_i = -(zref - i) * hPly; % This automatically calculates z1, z2, ..., zn
   z_prev = -(zref - (i-1)) * hPly;  % Previous z value

   %     Using previously computed Qth values
   eval(['Qth_current = Qth' num2str(i) ';']);

   %     Calculating A and B components
   A = A + Qth_current * (z_i - z_prev);
   B = B + (1/2)*(Qth_current * (z_i^2 - z_prev^2));  % For B calculation
   D = D + (1/3)*(Qth_current * (z_i^3 - z_prev^3));  % For B calculation
end
```

```
%    Finding if B is symetrical based on the ply orientation
%    Check if A is mirrored (symmetric)
if isequal(or, fliplr(or))
   B = zeros(size(B));
   ABD = [A, B; B D];
   disp('Layup is Symmetric; B=0.');
else
   B = -B;
   ABD = [A, B; B D];
   disp('Layup is Symmetric; B is not 0.');
end

%    End of Section where ABD Matrix is determined ----------------------------

%    Re-assigning indices in A, B, and D matrices for consistency with book
A(1,6) = A(1,3);
A(2,6) = A(2,3);
A(6,6) = A(3,3);

B(1,6) = B(1,3);
B(2,6) = B(2,3);
B(6,6) = B(3,3);

D(1,6) = D(1,3);
D(2,6) = D(2,3);
D(6,6) = D(3,3);


%    Computing the various values to find the constants f_i
R = ri + 0.5*h;     % Radius of Reference [m]
D1 = N/(2*pi*R);   % Constant Required for Analysis, from loading
D2 = T/(2*pi*R^2);  % Constant Required for Analysis, from loading

a1 = [A(2,2) - B(2,2)/R,   B(1,2);...
   B(1,2) - D(1,2)/R,     D(1,1)];

a3 = [A(1,1),               A(1,6) - (2/R)*B(1,6);...
   A(1,6) + B(1,6)/R,       A(6,6) - B(6,6)/R - (2/R^2)*D(6,6)];

a2 = [A(1,2) - B(1,2)/R,      B(1,1);...
   A(2,6) - D(2,6)/R^2,      B(1,6) + D(1,6)/R];

a4 = [A(1,2),               A(2,6) - (2/R)*B(2,6);...
   B(1,1),                 B(1,6) - (2/R)*D(1,6)];
```

```
H = a1 - (a4/a3)*a2;

g = (a4/a3)*[D1 D2]';

f1 = H(2,2);
f2 = (-1/R)*(H(2,1) + H(1,2));
f3 = H(1,1)/R^2;
f4 = Pz0 - g(1)/R;
f5 = Pz1;

%    Roots of Characteristic Polynomial
ga = sqrt((-f2 + sqrt(f2^2 - 4*f1*f3))/(2*f1));
la = real(ga);          % Real Component
be = imag(ga);          % Imaginary Component

%    Y-parameters from table 8.3 (p. 375)
Y13 = exp(-la*L)*cos(be*L);
Y23 = exp(-la*L)*(la*cos(be*L) + be*sin(be*L));
Y31 = Y13;
Y41 = -Y23;
Y14 = exp(-la*L)*sin(be*L);
Y24 = exp(-la*L)*(-be*cos(be*L) + la*sin(be*L));
Y32 = Y14;
Y42 = exp(-la*L)*(be*cos(be*L) - la*sin(be*L));

%    Creating System of Matrices to Solve for the Constants, C1 - C4
Ymat = [1,     0,       Y13,      Y14;...
   -la,       be,       Y23,      Y24;...
   Y31,       Y32,      1,        0;...
   Y41,       Y42,      -la,      be];
fmat = -[f4/f3; f5/f3;    (1/f3)*(f4 + L*f5); f5/f3];
C = Ymat\fmat;
C1 = C(1);
C2 = C(2);
C3 = C(3);
C4 = C(4);

%    Generating radial w0, axial u0, and circumferential v0 displacements
w0 = exp(-la.*x).*(C1*cos(be.*x) + C2*sin(be.*x)) + ...
    exp(-la.*(L - x)).*((C3*cos(be.*(L - x))) + C4*sin(be*(L - x))) + ...
    (1/f3)*(f4 + x.*f5);          % Radial Displacements [m]

intw0dx = (1/f3).*(f4.*x + 0.5.*(x.^2).*f5) + ...
    exp(-la.*x).*cos(be.*x).*((-la*C1 - be*C2)./(la^2 + be^2)) + ...
    exp(-la.*x).*sin(be.*x).*((be*C1 - la*C2)./(la^2 + be^2)) + ...
    exp(-la.*(L - x)).*cos(be.*(L - x)).*((la*C3 + be*C4)./(la^2 + be^2)) + ...
```

```
    exp(-la.*(L - x)).*sin(be.*(L - x)).*((-be*C3 + la*C4)./(la^2 + be^2));

dw0dw = f5/f3 + exp(-la.*x).*cos(be.*x).*(-la*C1 + be*C2) + ...
    exp(-la.*x).*sin(be.*x).*(-be*C1 - la*C2) + ...
    exp(-la.*(L - x)).*cos(be.*(L - x)).*(la*C3 - be*C4) + ...
    exp(-la.*(L - x)).*sin(be.*(L - x)).*(be*C3 + la*C4);

%    The elements of equation 8.37 are separated as follows for convenience:
el3 = [intw0dx./R; -dw0dw];
el6 = [D1; D2];
xArray = [x; x]';       % To make matrices agree with x values

u0v0 =  -(a3\a2)*el3 + transpose(xArray*inv(a3)*el6);

%    Extracting individual results
u0 = u0v0(1,:);         % Axial Displacements [m]
v0 = u0v0(2,:);         % Circumferential Displacements [m]


%    Plotting Results
figure,
plot(w0, x)
grid on
ylabel('Axial Distance [m]', 'FontWeight',' bold')
xlabel('Radial Displacements [m]', 'FontWeight',' bold')

figure(2),
plot(u0, x)
grid on
ylabel('Axial Distance [m]', 'FontWeight',' bold')
xlabel('Axial Displacements [m]', 'FontWeight',' bold')

figure(3),
plot(v0, x)
grid on
ylabel('Axial Distance [m]', 'FontWeight',' bold')
xlabel('Circumferential Displacements [m]', 'FontWeight',' bold')
```

Appendix C: Calculations of Critical Buckling Load for the Cylindrical Pressure Hull

```
%%   Buckling Analysis of Composite Cylinder, p. 407
%    Based on Equations from Ch 8.4 (Mechanics of Composite Structures (p. 404)
%    Developed by Ignacio Ramirez Romero
%    General Commands
clear all; close all; clc;

%    Cylinder Geometry and Other Constants
h = 12.7e-2;                    % Thickness [m]
L = 2.5298;                     % Length [m]
ri = 70.11e-2;                  % Inner Radius [m]
Ry = ri + 0.5*h;                % Shell Radius
Rx = inf;                       % Analysis Constant
Rxy = Rx;                       % Analysis Constant

%    Loading Conditions
Nx0 = 1;                        % Assumed Axial Load [N]
Ny0 = 0;                        % Transverse Load [N]
Nxy0 = 0;                       % Membrane Load [N]

%    Ply Geometry and Computation of ABD Matrix   ----------------------------
hLa = h;                        % Lamina Thickness [m]
or = repmat([0, 90], 1, 333);          % Array with Ply Orientation [0, 90]_333
or = [or, 0];                   % Adds 0 Ply to match Titan's Laminate
plyNu = 1:length(or);                % Ply Number Assignment, Bottom to Top
hPly = hLa/(length(or));             % Thickness of Each Ply
zref = round(length(or)/2);          % Reference plane (middle of laminate)

%    Computation of Ply Properties using Rules of Mixture
%    Properties of Fiber
Ef1 = 231e9;                    % Longitudinal Youngs Modulus of Fiber [Pa]
Gf12 = 91e9;                    % Longitudunal Shear Modulus of Fiber [Pa]
nuf12 = 0.27;                   % Longitudinal Poisson's Ratio of Fiber
Vf = 0.7;                       % Volume Fiber Fraction

%    Properties of Matrix
Em = 2.8e9;                     % Matrix Young Modulus [Pa]
Gm = 1e9;                       % Matrix Youngs Modulus [Pa]
num = 0.35;                     % Matrix Poisson's Ratio

%    Rules of Mixture Ply Properties
E1 = Ef1*Vf + Em*(1-Vf);
E2 = (Vf/Ef1 + ((1-Vf)/Em))^-1;
G12 = (Vf/Gf12 + ((1-Vf)/Gm))^-1;
nu12 = nuf12*Vf + num*(1-Vf);
```

```
%    Reduced Stiffness Matrix for reference ply at 0 deg
D = 1 - (E2/E1)*nu12^2;                % Engineering Constant [unitless]
Q0 = [E1/D,         (nu12*E2)/D,       0;...
    (nu12*E2)/D,   E2/D,              0;...
    0,             0,                 G12];

%    Calculation of Reduced Stiffness Matrix of All Other Plies
for i = 1:length(or)
   % Defining the current angle th
   th = or(i);

   % Checking if th = 0
   if th == 0
      % If th1 is 0, create Qth variable with name Qth1, Qth2, ..., Qth5
      eval(['Qth' num2str(i) ' = Q0;']);
   else
      %      Otherwise, compute Tsig and Teps based on the current angle (i)
      Tsig = [cosd(th)^2,      sind(th)^2,         2*cosd(th)*sind(th);...
            sind(th)^2,         cosd(th)^2,         -2*cosd(th)*sind(th);...
            -cosd(th)*sind(th), cosd(th)*sind(th),  cosd(th)^2 - sind(th)^2];

      Teps = [cosd(th)^2,      sind(th)^2,         cosd(th)*sind(th);...
            sind(th)^2,         cosd(th)^2,         -cosd(th)*sind(th);...
            -2*cosd(th)*sind(th), 2*cosd(th)*sind(th),  cosd(th)^2 - sind(th)^2];

      %     Computing Qth using the formula Qth = Tsig \ Q0 * Teps
      eval(['Qth' num2str(i) ' = Tsig\Q0*Teps;']);
   end
end

A = 0; % Initial value for loop summation [N/m]
B = 0; % Initial value for loop summation [N]
D = 0; % Initial value for loop summation [N*m]

for i = 1:length(or)
   %     Calculating z values (z0, z1, z2, ..., zn)
   z_i = -(zref - i) * hPly; % This automatically calculates z1, z2, ..., zn
   z_prev = -(zref - (i-1)) * hPly;  % Previous z value

   %     Using previously computed Qth values
   eval(['Qth_current = Qth' num2str(i) ';']);

   %     Calculating A and B components
   A = A + Qth_current * (z_i - z_prev);
   B = B + (1/2)*(Qth_current * (z_i^2 - z_prev^2));  % For B calculation
   D = D + (1/3)*(Qth_current * (z_i^3 - z_prev^3));  % For B calculation
```

```
end

%    Finding if B is symetrical based on the ply orientation
%    Check if A is mirrored (symmetric)
if isequal(or, fliplr(or))
   B = zeros(size(B));
   ABD = [A, B; B D];
   disp('Layup is Symmetric; B=0.');
else
   B = -B;
   ABD = [A, B; B D];
   disp('Layup is Symmetric; B is not 0.');
end

%    End of Section where ABD Matrix is determined ----------------------------

%    Re-assigning indices in A, B, and D matrices for consistency with book
A(1,6) = A(1,3);
A(2,6) = A(2,3);
A(6,6) = A(3,3);

B(1,6) = B(1,3);
B(2,6) = B(2,3);
B(6,6) = B(3,3);

D(1,6) = D(1,3);
D(2,6) = D(2,3);
D(6,6) = D(3,3);

%    Generating M0, Mn, and J matrices
M0 = [A(1,1),  A(1,2),   0,       B(1,1),   B(1,2),   0;...
    A(1,2),   A(2,2),   0,       B(1,2),   B(2,2),   0;...
    0,        0,        A(6,6),   0,        0,        B(6,6);...
    B(1,1),   B(1,2),   0,       D(1,1),   D(1,2),   0;...
    B(1,2),   B(2,2),   0,       D(1,2),   D(2,2),   0;...
    0,        0,        B(6,6),   0,        0,        D(6,6)];

Mn = ABD - M0;

J = [0, 0, 0;...
    0, 0, 0;...
    0, 0, 1];

%    Defining parameter ranges
al = linspace(1, 50, 100);
be = linspace(1, 50, 100);
```

```
c1 = linspace(0, 2, 21);
c2 = linspace(0, 2, 21);

%    Preallocating storage for results
la = struct();

%    Iterating over all possible combinations
for i = 1:length(al)
   for j = 1:length(be)
      for k = 1:length(c1)
         for m = 1:length(c2)

            %   Extracting current parameter values
            al1 = al(i);
            be1 = be(j);
            c11 = c1(k);
            c21 = c2(m);

            %   Generating O and L matrices
            O = [-al1,     0,        be1,      0,        0,        0;...
                0,        -be1,     al1,      0,        0,        0;...
                1/Rx,     1/Ry,     0,        al1^2+((be1^2)*c21^2), be1^2+((al1^2)*c11^2),  -
2*al1*be1*(1+c11*c21)];

            L = [be1*c21,   0,        -al1*c11,  0,        0,        0;...
                0,        al1*c11,  -be1*c21,  0,        0,        0;...
                0,        0,        1/Rxy,    -2*al1*be1*c21,     -2*al1*be1*c11,     2*(c11*al1^2 +
c21*be1^2)];

            %   Computing OL, G, Ph1, Ph2, PhJ
            OL = [O, L; L, O];
            G = OL * [M0, Mn; Mn, M0] * transpose(OL);

            %   Computing Phi matrices
            Ph1 = al1^2 + be1^2*c21^2;
            Ph2 = -2*al1*be1*c21;
            PhJ = [Ph1*J, Ph2*J; Ph2*J, Ph1*J];

            %   Solving eigenvalue problem
            eigenVals = eig(G, PhJ);
            la_min = min(eigenVals);

            %   Storing result with dynamic field naming
            field_name = sprintf('la_al%d_be%d_c1%d_c2%d', i, j, k, m);
            la.(field_name) = la_min;
         end
```

```
        end
    end
end

%    Extracting Results
%    Extracting field names and corresponding values
fields = fieldnames(la);
values = struct2array(la);

%    Filtering the infinite values
finite_indices = ~isinf(values) & (values > 0) & isreal(values);  % Ensure values are finite,
positive, and real
finite_values = values(finite_indices);
finite_fields = fields(finite_indices);

%    Ensuring there are valid finite values before proceeding
if isempty(finite_values)
    error('No finite values found in the dataset.');
end

%    Finding the minimum finite value
[la_result, min_idx] = min(finite_values);

%    Extracting the corresponding field name
min_field = finite_fields{min_idx};

%    Parsing the field name to extract indices
tokens = regexp(min_field, 'la_al(\d+)_be(\d+)_c1(\d+)_c2(\d+)', 'tokens');
tokens = str2double(tokens{1});  % Convert extracted strings to numbers

%    Extracting indices
i_res = tokens(1);
j_res = tokens(2);
k_res = tokens(3);
m_res = tokens(4);

%    Retrieving actual parameter values
al_res = al(i_res);
be_res = be(j_res);
c1_res = c1(k_res);
c2_res = c2(m_res);

%    Displaying results
fprintf('Minimum finite la: %.6f\n', la_result);
fprintf('Occurs at: al = %.2f, be = %.2f, c1 = %.2f, c2 = %.2f\n', al_res, be_res, c1_res, c2_res);
```